INTERACTION EFFECTS IN ELECTRONIC TRANSPORT THROUGH ONE-DIMENSIONAL QUANTUM DOTS

Dissertation
zur Erlangung des Doktorgrades
des Fachbereichs Physik
der Universität Hamburg

vorgelegt von
Tobias Kleimann
aus Duisburg

Hamburg
2003

.

Gutachter der Dissertation:	Prof. Dr. B. Kramer Prof. Dr. M. Sassetti
Gutachter der Disputation:	Prof. Dr. B. Kramer PD Dr. T. Brandes
Datum der Disputation:	6. Mai 2003
Vorsitzender des Prüfungsausschusses:	PD Dr. S. Kettemann
Vorsitzender des Promotionsausschusses:	Prof. Dr. R. Wiesendanger
Dekan des Fachbereichs Physik:	Prof. Dr. G. Huber

Abstract

We investigate the linear DC transport properties of one-dimensional quantum dots that are immersed in quantum wires. The electronic interaction is treated microscopically in terms of the Tomonaga-Luttinger liquid model for one-dimensional electrons.

The quantum dot is modeled as a double barrier structure in the quantum wire. We derive an effective theory to model sequential tunneling through the dot to describe the Coulomb blockade phenomenon. We obtain a microscopic charging energy, the level structure of the dot, and a description of the lineshape of the Coulomb blockade conductance peaks. The temperature behaviour of Coulomb blockade peaks is determined by electronic correlations.

First, we investigate the effect of a homogeneous long-range interaction on the charging energy, the excitations of the quantum dot and the external electric field. The temperature behaviour of the Coulomb blockade peaks is driven by a power-law with effective exponents that depend directly on -and take into account- the long-range nature of the interaction and the spin degree of freedom.

Second, we use a nonhomogeneous, slowly varying interaction strength along the system to model leads with a weaker interaction far away from the quantum dot position. We find that depending on the temperature range one detects from the Coulomb blockade the local interaction strength or a global strength dominated by the weak leads-interaction. This is reflected in a crossover in the power-law in temperature for the Coulomb blockade peaks.

Third, we study the effects of metallic leads which are coupled through tunnel junctions to a homogeneous quantum wire containing a one-dimensional dot. This shows again that, depending on the temperature range, measurements of the Coulomb blockade conductance probe the local (quantum dot) or global (metallic leads) properties of the interaction.

Zusammenfassung

Wir untersuchen die linearen DC Transporteigenschaften von eindimensionalen Quantenpunkten, die in Quantendrähten eingebettet sind. Die elektronische Wechselwirkung ist im Rahmen des Modells der Tomonaga–Luttinger Flüssigkeit für eindimensionale Systeme berücksichtigt.

Der Quantenpunkt ist durch eine Doppelbarrierenstruktur im Quantendraht beschrieben, und wir entwickeln ein Modell für sequentielles Tunneln durch den Quantenpunkt, um den Coulomb-Blockade-Effekt zu beschreiben. Das Modell liefert eine mikroskopische Ladungsenergie, die Zustände des Quantenpunktes und die Form der Resonanzkurve der Coulomb-Blockade-Leitfähigkeit. Die Temperaturabhängigkeit dieser Kurve wird durch die Form und Stärke Elektronwechselwirkung bestimmt.

Zunächst untersuchen wir den Effekt einer langreichweitigen Wechselwirkung auf die Ladungsenergie, das Anregungsspektrum des Quantenpunktes und ein

extern angelegtes elektrisches Feld. Die Temperaturabhängigkeit der Coulomb-Blockade-Resonanz ist durch ein Potenzgesetz mit effektiven Exponenten gegeben, die direkt von den Eigenschaften des Wechselwirkungspotentials und dem Spin-Freiheitsgrad abhängen.

Dann nehmen wir eine inhomogene, sich langsam entlang des Systems ändernde Wechselwirkungsstärke an. Dabei ist die Wechselwirkung in den Zuleitungen, weit entfernt von der Position des Quantenpunktes, schwächer. Es wird gezeigt, dass aus Analyse der Temperaturabhängigkeit der Coulomb-Blockade, abhängig vom gewählten Temperaturbereich, entweder die lokale Wechselwirkungsstärke bestimmt wird, oder aber die Schwächere in den Zuleitungen. Dies sieht man am Übergang zwischen zwei Potenzgesetzen für die Temperaturabhängigkeit der Coulomb-Blockade-Resonanzen.

Zuletzt untersuchen wir den Effekt von Metallzuleitungen, die durch Tunnelkontakte an den homogenen Quantendraht mit eingebettetem Quantendot gekoppelt sind. Wir finden erneut, dass durch Messungen der Coulomb-Blockade entweder die lokalen (am Quantenpunkt vorliegenden) oder globalen (an den Zuleitungen vorherschende) Eigenschaften der Wechselwirkung sondiert werden. Ob lokal oder global gemessen wird, hängt wiederum stark vom Temperaturbereich der Untersuchung ab.

Contents

1 Introduction

"There's plenty of room at the bottom" said Richard P. Feynman 1959 in a speech at the annual meeting of the American Physical Society [1]. He then raised the ideas of manipulating things on a nanometer scale and what today is called *nanotechnology*. A lot of what Feynman pictured over 40 years ago is reality now, like the possibility of putting the information contained in the of the Encyclopædia Britannica on the head of a pin, and imaging single DNA molecules. For the development of the scanning tunneling microscope [2] the Nobel Prize was awarded to Binnig and Rohrer in 1986, and also atoms can be rearranged one by one with the atomic force microscope [3]. Miniaturizing of the computer is today an industrial issue, and the size of a transistor, which was invented in 1949 by Shockley, Bardeen and Brattain [4] has shrunk from a bulky piece of semiconductor material on a workbench to microprocessors that contain 29 million transistors in just one chip the size of a thumbnail [5]. Moore's law [6] says that the number of transistors per integrated circuit grows exponentially, and because of technology advances every couple of years the number of transistors on a chip double. Ever tinier electronic circuits require ever smaller and narrower wires to connect the devices, and one may arrive at sizes where, as Feynman put it, "we can use, not just circuits, but some system involving the quantized energy levels, or the interactions of quantized spin, etc."

Such minute systems where the motion of microscopic degrees of freedom, such as electrons or phonons, is restricted to less than the usual three dimensions are called *low-dimensional systems*. During the past decades there has been a lot of interest in low-dimensional quantum systems driven by the discovery new phenomena and the potential of developing new electronic devices. The workhorse for investigating low dimensional phenomena are semiconductor nanostructures engineered at the atomic scale. But also the use of entire molecules as has become possible and fueled the boom of nanoscience and nanotechnology .

The study of low dimensional quantum phenomena has led to new fields of research like the physics of *mesoscopic systems*. Mesoscopic phenomena are found in the regime between microscopic and macroscopic physics [7]. A mesoscopic system is usually larger than a few atoms or molecules but it is small enough that the electrons must be regarded as quantum mechanical particles. The appealing feature of mesoscopic systems, that contain a macroscopic number of electrons, is that they can exhibit quantum mechanical phenomena which are apparently of microscopic origin.

The geometrical size $\sim L$ of a mesoscopic system should be smaller than or of the order of the phase coherence length L_φ. This is the characteristic length scale over which a particle stays in a particular eigenstate and maintains phase coherence. L_φ generally depends on the dimension and temperature of the system and microscopic details of the inelastic scattering. Remarkably, L_φ increases when the temperature is lowered and can become comparable to the the system size even if the elastic mean free path is shorter than the system. For instance, then the transport properties of a mesoscopic sample can be influenced by quantum interference. The *Aharonov–Bohm effect* is a prominent example how a magnetic field

alters quantum mechanic interference patterns [8]: the conductance of a tiny ring that is contacted at opposite points shows oscillations as a function of the magnetic flux enclosed by the ring. This is due to the difference in the picked up phases for electrons traveling clockwise or anti-clockwise from one contact to the ring to the the other. It was also found that *persistent currents* can flow in a small metallic ring when its circumference is smaller than the phase coherence length of the electrons [9, 10, 11]. If the ring is threaded by a magnetic flux current will flow around the ring without dissipation even in the presence of disorder. The persistent current can be detected as a magnetization without contacting the ring with leads.

We mention only in passing the perhaps most famous mesoscopic effect, the *quantum Hall effect*. It is a vast and active field of theoretical and experimental studies. The quantum Hall effect occurs when two-dimensional electron gas (2DEG) is placed in a strong perpendicular magnetic field [12]. Classically one expects a monotonic behaviour of the Hall resistance when the carrier density changed. However, it turned out that the transverse, or Hall resistance shows plateaus at $R_{\mathrm{H}} = h/\nu e^2$ where the filling factor ν can be adjusted to be an integer number. ν can be tuned by a change in the magnetic field or electron density . At the same time the Hall resistance is constant the longitudinal resistance vanishes. Because only the fundamental constants e and h are involved in R_{H} the quantum Hall effect today serves as a current standard.

In this thesis, we focus on the mesoscopic transport properties of wire-like, one-dimensional structures. In particular, we want to concentrate on the effects of the mutual Coulomb interaction between the electrons. Electronic transport can be examined in quantum point contacts defined by a constriction of a 2DEG. There, the *conductance* appears to be *quantized* [13, 14]. By applying a negative voltage to a metallic gate the 2DEG below is depleted, and a narrow channel can be formed by an opening in the gate. The width of the channel is adjusted by changing the the gate voltage. When widening the opening the current through this quantum point contact does not increase gradually but stepwise in units $2e^2/h$ because each transverse mode in the one-dimensional channel contributes one conductance quantum to the transport, and the two stems from the spin degeneration.

A long, stretched quantum point contact can lead to a *quantum wire* where the electronic motion is confined to just one dimension. In such one-dimensional (1D) conductors, or quasi 1D systems, where by appropriately applied confinement potentials the transverse modes are squeezed out, the mutual Coulomb interaction between the electrons is expected to alter the transport properties of the wires with respect to 2D. The *Tomonaga–Luttinger liquid* model (TLL) serves as a theory for interacting electrons in one dimension. It is for the most part analytically calculable, and we employ the model throughout this theses for calculating the transport properties of 1D quantum dots connected to quantum wires. The TLL predicts collective spin and charge density waves as elementary excitations in the 1D electron system. These two types of excitations are completely decoupled because they propagate at different velocities due to the interaction [15]. This phenomenon is called *spin charge separation* and is unique for 1D systems. In terms of the TLL a renormalization of the linear conductance of a clean quantum wire by the interaction parameter

g_0 [16] is expected: $\mathcal{G} = 2e^2 g_0/h$. In transport experiments however the DC conductance at relatively high temperatures showed only a quantization in terms of the universal conductance $2e^2/h$. This could be explained either as an effect of the noninteracting leads which are connected to the quantum wire [17, 18, 19], or in terms of a self-consistent treatment of the electric driving potential [20, 21]. In the presence of weak disorder and low temperatures deviations from the universal conductance steps are expected. The corrections have peculiar power-law dependencies in temperature $\delta\mathcal{G} \propto T^{f(g_0)}$ where the power-law exponent is a function of the interaction parameter g_0 [17]. Strong, localized impurity potentials are also expected to give rise to power-laws in temperature for their tunnel conductances [16, 22]. This is what is usually interpreted as a typical Luttinger liquid feature. Rather than the conductance of a clean quantum wire, power-laws in temperature for a tunnel conductance or conductance plateaus are signals for a 1D TLL system. Experimentalist search for such TLL features in quantum wires based on semiconductor heterostructures or carbon nanotubes.

The electronic interaction is evident in the peculiar transport properties of *quantum dots*. In a quantum dot the electrons are confined in all three dimensions to a tiny island and electrons can only tunnel on and off the dot to the attached leads. In transport through such a zero-dimensional system *Coulomb blockade* occurs when the chemical potentials of the weakly coupled leads are not aligned with the potential of the dot. On alignment the electrons can pass the dot one by one because of the charging energy which arises from the Coulomb interaction and one speaks of a *single electron transistor*.

We want to study the combined effects of the interaction in a one-dimensional quantum wire and the influence of impurities on the transport. Since today there are experimental realizations of quantum dots embedded in quantum wires, we concentrate on the linear transport through one-dimensional quantum dots. Here "one-dimensional" is used in the sense that the quantum dot is a tiny island in the quantum wire, which is defined by at two localized impurities. We regard the entire system (quantum wire plus two localized impurities) as the one-dimensional quantum dot immersed in a quantum wire.

This thesis is organized as follows: we give a brief overview of the experimentally available quantum wires, either on semiconductor basis or on a molecular basis as carbon nanotubes (chapter 2). 1D quantum dots with leads can be fabricated as quantum wires with two localized impurities which effectively cut the wire. In this situation the Coulomb blockade phenomena can be studied. In order to investigate CB in these systems microscopically we introduce the standard Tomonaga–Luttinger liquid model for 1D interacting electrons in chapter 3. It serves as the workhorse for our description of electronic transport through quantum wires and 1D dots. We develop a model appropriate for linear electronic transport through a 1D quantum dot with 1D leads in terms of the TLL in chapter 4. This is achieved by deriving an effective action for a TLL with a double barrier structure, and then mapping onto a model for quantum Brownian particle in a 2D washboard potential. And because we assume sequential tunneling, a Master equation for the tunneling rates can be set up and solved in the limit of the linear transport for the

Coulomb blockade peaks. This yields a closed form for the conductance peak lineshape which shows up as a certain power-law in temperature. Also the charging energy of quantum island is derived microscopically. We employ our microscopic model in chapter 5 for different electronic interaction types. First, the effects of a special long-range interaction on the spectrum of the 1D dot coupled to the quantum wire leads is discussed (chapter 5.1). We find that the levels of the quantum dot acquire a finite width, which is in contrast to the usual case where zero-range interaction is assumed. Additionally the level positions are shifted in energy with respect to the zero-range counterparts. Also the power-law exponent, e. g. for the CB peak maxima $\mathcal{G}_{\mathrm{d}}^{\max}(T) \propto T^{1/g_0-2}$, differs from the zero-range interaction and has to be replaced by an effective g_{eff} which depends on the geometry of the dot and the interaction range. Second, in chapter 5.2, a realistic long-range interaction is assumed to describe the effects of electrostatic gates used for confinement in the cleaved-edge-overgrowth quantum wires. We also take into account the spin degree of freedom here. The theoretical charge and spin addition energies are compared to data from experiments where successive CB peaks were detected. The additional spin degree and the long-range interaction potential lead to an altered power-law for the CB peak conductance $\mathcal{G}_{\mathrm{d}}^{\max}(T) \propto T^{1/g_{\mathrm{eff}}-2}$. However, the value of the interaction parameter obtained from the analysis of the experimental data of the CB peaks was found to be different from the one expected from the charging energy. We conclude that inhomogeneity effects in the interaction should be considered for a proper description of quantum transport through one-dimensional quantum dots immersed in a TLL. The two (sub)chapters 5.3 and 5.4 are devoted to the role of the contacts attached to the quantum wires containing the dot. We use a smoothly varying interaction strength along the quantum wire to describe the situation in the CEO quantum wires: the interaction parameter $g(x)$ varies from g_0 at $|x| \to \infty$ (leads of the quantum wire) to g_{d} in the region where the two barriers define the quantum dot. We find that the level spacing and the charging energy of the dot always depend on the local value $g(x_{\mathrm{d}})$. However, the power-law for the CB peaks are no longer universal for all temperatures. The power-law exponent $\mathcal{G}_{\mathrm{d}}^{\max}(T) \propto T^{1/g_{\mathrm{eff}}-2}$ of the peak conductance shows a crossover between $g_{\mathrm{eff}} = g_0$ (at low T) and $g_{\mathrm{eff}} = g(x_{\mathrm{d}})$ (at high T). We follow a different approach in chapter 5.4 to describe the situation of a 1D quantum dot in a nanotube quantum wire. The interaction parameter is kept constant in the nanotube, but the tube itself is attached to metallic leads. These contacts are assumed to be tunnel contacts and yield nonanalytic power-laws in temperature for the contact conductance. This is due to the tunneling into the interacting 1D electron system from the Fermi liquid leads. We find that the temperature behaviour of the CB conductance peaks can be determined by contact conductances. Again, a crossover in the temperature power-law for the conductance of the CB peaks is predicted. The low temperature properties are dominated by the leads through the tunnel contacts, and the high-T properties are determined by the local interaction parameter of the nanotube with the dot.

2 Quantum wires and dots

Quantum wires are extremely narrow nanostructures where the electrons are only allowed to move in one direction and are confined in the other two. Hence one expects TLL behaviour in quantum wires or systems containing these 1D wires. However in order to examine the effects due to the interaction of the electrons in the wire very clean devices are needed, and only one subband should be occupied by the electrons. The situation becomes even more experimentally sophisticated when controlled impurities or tunnel barriers in the quantum wires are desired. We discuss two realizations of clean single channel quantum wires here: first, semiconductor wires fabricated with the so called cleaved edge overgrowth technique (CEO), and second single wall carbon nanotubes (SWCN). Both present fairly clean and well defined 1D electron systems. The two realizations have their advantages and disadvantages as we will briefly discuss in this chapter.

2.1 Semiconductor quantum wires

Early quantum wires on semiconductor basis were realized by beam epitaxy and chemical etching [23, 24, 25] of GaAs/AlGaAs heterostructures (fig. 1). A periodic confinement potential is established by lines of charged Si donors in the bridges. In such wires usually a couple of 1D subbands are occupied (schematically depicted in fig. 2). The periodic arrays of wires were studied by Raman scattering

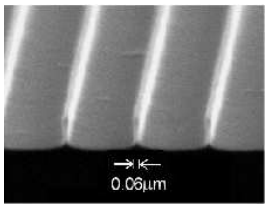

Figure 1: Array of parallel quantum wires produced by etching (courtesy C. Schüller, Zentrum für Mikrostrukturforschung, Hamburg)

and revealed the typical collective charge and density excitations for one dimensional systems [26, 27, 28]. The involved energies exceeded the subband spacing of the one-dimensional modes and intra and interband excitations could be interpreted in terms of the TLL model [29]. First electronic transport measurements in one-dimensional wires were also done on similar but wider wires [25]. The conductance was measured for one and ten parallel wires and showed quantization in entire $2e^2/h$ units per channel.

Signatures of Luttinger liquid physics (a T-dependent conductance) were reported in experiments done on gated quantum wires [30, 31]. They are created by putting metallic gates on top of a two-dimensional electron gas and applying voltages to deplete the electron gas underneath. This can produce wires of varying length and width. By changing the width in a controlled fashion also the number of transverse modes can be tuned. In [30] a temperature dependent reduction of the quantized conductance of the quantum wires was measured. This was attributed to elastic scattering in the wires.

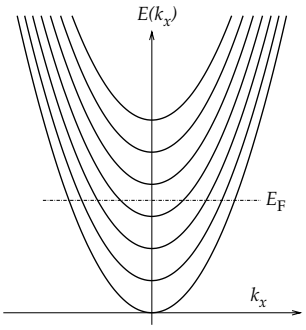

Figure 2: Idealized bandstructure for a quasi one-dimensional wire where x runs along the wire axis. The Fermi level is chosen as to occupy only four subbands.

Also by using a pair of split gates it is possible to define a one-dimensional channel within the 2DEG. If the elastic scattering length is longer than the 1D channel, transport through the channel is ballistic and one observes conductance plateaus. The temperature dependence of the conductance steps was measured employing the split gate technique for producing quantum wires in [32, 33].

The growth of wires in v-grooves offers a hard confinement of the charge carriers as opposed to the soft electrostatic confinement by gates. Here the substrate is corrugated such that the GaAs tends to grow in the bottom of the v-groove patterns. In this way a crescent shaped quasi 1D channel between semi-insulating AlGaAs barriers is formed. The 1D subband separation in v-grooves wires is usually larger than in gated wires [34, 35] and additional placed gates may allow to perform two and four terminal transport measurements which showed quantized conductance steps.

Today, very clean semiconductor quantum wires are fabricated with the cleaved edge overgrowth (CEO) technique [36, 37, 38, 39]. Moreover experiments with localized impurities could be realized. Here, the the wire is realized by making first a GaAs quantum well between two AlGaAs layers as illustrated in fig. 3. Then

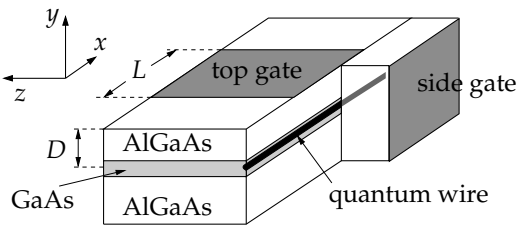

Figure 3: CEO quantum wire preparation and sample geometry (see text).

an evaporated tungsten top gate is deposited on the structure. This separates the two dimensional electron gas below (distance $D \approx$500nm) into two halves when it is negatively biased. After cleaving the sample a second modulation doping sequence is grown on the cleavage plane. This introduces electrons at the edge of the quantum well and creates confined edge states along the cleave. A side gate is placed on the perpendicular second doping sequence. The strongest 1D confinement is obtained when the top gate is biased negatively and depletes the 2 DEG

underneath such that only the wire is a possible conduction channel and the side gate is biased positively to push the electrons against the edge. The confinement then stems from the quantum well (y-direction), the cleaved edge modulating sequence (z-direction) and to some extent from the side and top gates. Electrons enter from one part of the 2DEG the one-dimensional region, travel through the quantum wire (x-direction) and exit into the second part of the 2DEG. The connection to the measuring apparatus is realized by Ohmic contacts formed by diffused Indium-dots in the electron gas. The subband spacing between the 1D bands is up to 25mev and they can be (de)populated successively one-by-one. So real one channel quantum wires can be achieved. Quantum wires produced with the CEO technique show very flat conductance plateaus when the density is reduced and subbands are depleted successively by biasing the top gate. This flatness indicates that backscattering is almost absent in these wires and transport is ballistic. However, conductances systematically lower than the universal quantum were reported [37]. Partly this can be explained by weak disorder in the wire and a connection to the 2DEG. This correction of the universal conductance scales with temperature and/or the wire length [40] which was also measured in conventional quantum wires [30]. However, in the CEO wires the assumption of non-interacting Fermi liquid leads is not necessarily met. The 1D system stretches along the entire edge (below the top gate as well as close to the 2DEG) and the leads can show non-Fermi liquid behaviour, too. We will come back to this point later in chapter 5.3.

One also succeeded to place non-invasive voltage probes to the CEO wire by adding supplementary top gates [41, 42]. This setup allows four-terminal and two-terminal measurements on the same wire. In that way the voltage probes almost do not disturb the current flow and it was shown that the resistance between the non-invasive probes vanish and thus the electrons propagate ballistically in the 1D system. Then the residual resistance can be attributed to the current contacts, *viz*. the 1D–2D coupling.

By fabricating two parallel CEO wires which are separated by a tunnel barrier and examining the tunneling between the two one-dimensional wires one can investigate the excitation spectrum of the interacting electrons in one dimension [43]. A specific amount of energy and momentum can be supplied to the system through an applied source-drain voltage between the wires and a magnetic field perpendicular to the two-wire plane. Because of conservation of energy and momentum in the particular geometry, tunneling is forbidden unless there exist elementary excitations that match elementary (collective excitations) in the system which are equal to the provided momentum and energy. From the tunneling current one can deduce the dispersion relations of the two one dimensional wires and detect the deviation from a genuine noninteracting system.

2.2 Molecular quantum wires – carbon nanotubes

One dimensional systems can also be realized by molecules. Carbon nanotubes as such a type of 1D conductors have been the focus of intense studies since their discovery in 1991 [44, 45]. These hollow cylinders are formed by rolling carbon

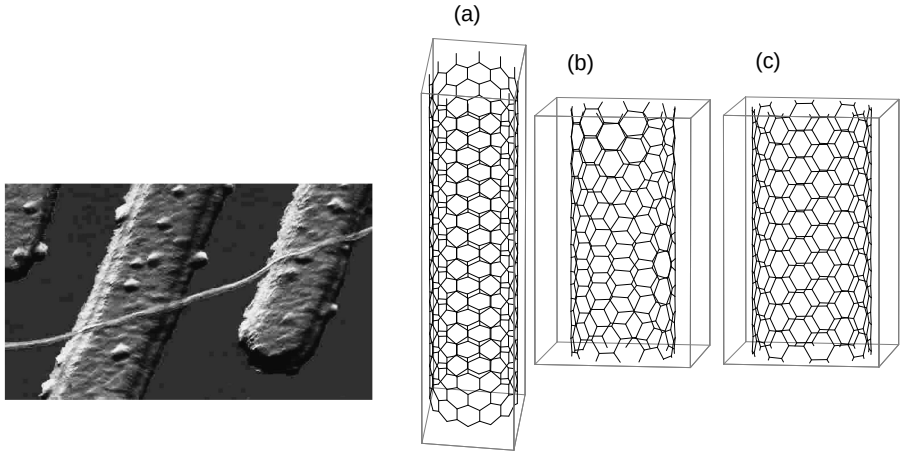

Figure 4: Left: Single wall nanotube over Pt electrodes. The distance between the electrodes is approximately 120nm (Copyright of this image by Cees Dekker and DIMES). Right: Lattice structure for zigzag [12,0] tube (a), chiral [8,6] tube (b), and armchair [8,8] tube (from [46])

sheets of hexagonal symmetry into tubes of various diameter.

Electronic structure

An ideal carbon nanotube (CN) can be thought of as a hexagonal network of carbon atoms that has been rolled up to make a seamless cylinder (fig. 4). The elementary translation vectors, $\vec{a}_1$ and $\vec{a}_2$ connect second neighbours on the elementary hexagon. Thus the geometry of the tube can be characterized by the wrapping vector $\vec{R}_{m,n} = m\vec{a}_1 + n\vec{a}_2$. Depending on n and m, three different types of nanotube can be obtained: zigzag ($n = 0$), armchair ($n = m$) or chiral (all other combinations of (n, m)) as depicted in fig. 4. For example, if a zigzag or armchair nanotube has 10 hexagons around its circumference, the 11th hexagonal will coincide with the first. Just a nanometer across, the cylinder can be tens of microns long, and each end is "capped" with half of a Fullerene molecule.

The unique electronic properties of carbon nanotubes are due to the quantum confinement of electrons normal to the nanotube axis. In the radial direction, electrons are confined by the monolayer thickness of the graphene sheet. Around the circumference of the nanotube, periodic boundary conditions come into play. These properties are due to the peculiar band structure of the π electrons [47]. The actual band structure of the nanotube is derived from the 2D dispersion relation calculated for a single graphene layer by taking into account the boundary condition for the $\vec{k}$ vector perpendicular to the tube axis imposed by the folding of the sheet. This leads to three generic cases [48] for a general wrapping vector $\vec{R}_{n,m}$: the valence

bands that are fully occupied in the ground state are separated from the unoccupied conduction bands by a finite gap. Then the system is either semiconducting or isolating. For particular choices of m and n however the gap will close and two pairs of levels cross at the Fermi energy at two Fermi points. For armchair nanotubes this always happens for the x-direction along the tube axis at $k_\pm = \frac{2}{3}\pi/a$. The situation is illustrated in fig. 5. The low energy properties of these metallic nan-

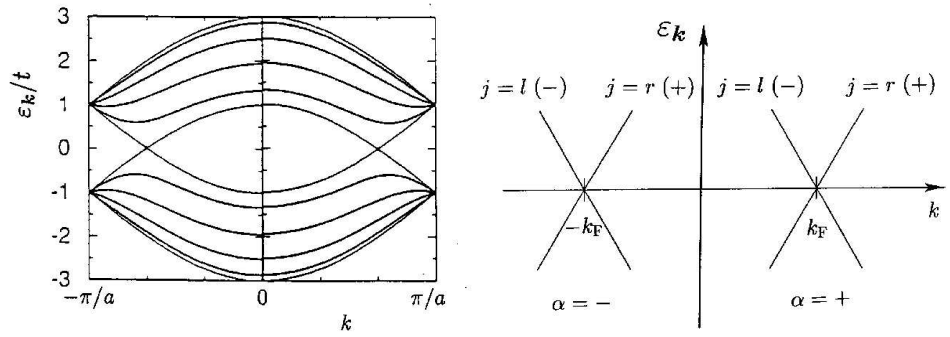

Figure 5: Left: band structure of an armchair (5,5) nanotube. t denotes the transfer integral in the tight binding approximation. Right: schematic bandstructure with the two Fermi points $\alpha = \pm$ and left and right moving electrons labelled by $j = \pm$.

otubes can be described by considering the states near the Fermi energy only. In this regime the four crossing one-dimensional bands can be approximated by linear dispersion relations. The 1D energy dispersion of an armchair CN was recently measured and displayed linear behaviour around the Fermi energy[49]. Due to the peculiar bandstructure and the enormous subband separation of the order eV these metallic armchair nanotubes can be regarded as real one-dimensional electron systems. Therefore a description in terms of TLL is possible, however four modes (two charge and two spin modes) carry current in the ground state. Hence the conductance of a clean CN quantum wire is expected to be quantized in units $4e^2/h$ and impurities should lead to power-laws with appropriate exponents due to the interaction.

Production of nanotubes

There are efficient methods to synthesize SWNT like laser evaporation and carbon arc synthesis or vapor growth. In laser evaporation sequenced laser pulses are used to evaporate a target containing carbon mixed with a small amount (1-2%) transition metal (Co/Ni). The vapor is then condensed at a cooled (Cu) collector at the end of a heated flow tube [50]. About 70% of the graphite is converted into SWNTs in this method, and tubes of various chiralities arise, although about half of them are armchair tubes. Also a carbon arc in a helium flow can be used to produce nanotubes. The CNs (20%) together with other nanoparticles, amorphous graphite

and Fullerenes deposit on a cathode in the generator [51]. In the vapor growth method hydrocarbons like CH_4, C_6H_6 and H_2 gases are reacted in presence of Fe, Co or Ni particles. This produces among other carbon fibers also nanotubes.

All methods have in common that no specific CNs are produced but the bundles, ropes or mats of the contain a blend of all types: semiconducting, metallic and isolating ones, single and multiwall types. Depending on the synthesization method and the use of catalysts the composition the percentages of the various types change but the final product always remains a mixture. Only further characterization techniques as scanning electron microscope or transmission electron microscope imaging[52, 53], or even electronic transport measurements can disclose the actual nature of the produced tubes.

Transport experiments on CNs

The strength and length of nanotubes makes it relatively straight forward to attach metallic electrodes. Electron beam or other lithography methods can be used to define those electrodes. Two approaches are possible: either the electrode metal is evaporated on top of the tubes, which are deposed on a substrate, or the tubes are placed on prefabricated electrodes. The latter method is shown in fig. 4, left. A gate electrode can be realized by a nearby surface electrode or doped substrate. Transport measurements at room temperature reveal conductances up to $3e^2/h$ [54, 55]. The deviation from the theoretically expected value $4e^2/h$ is usually attributed to the the contact resistance between CN and the metallic leads. This assumption supported is by measurements at lower temperatures. At intermediate T the conductance decreases monotonically when T decreases and is independent on the gate voltage. The quantitative temperature behaviour depends on the nature of the contacts. One finds different power-laws in temperature for the conductance $\mathcal{G} \propto T^{\alpha}$ of a CN for metal-on-tube devices and the tube-on-metal variety [56]. This can be understood from the type of contact to the nanotube: if the metallic electrode is placed on top of the CN the tube structure is destroyed below the metal and electrons have to tunnel into the end of the 1D electron system. Due to the interacting 1D electron system the tunneling current becomes temperature dependent in a power-law fashion which is in accordance with TLL predictions and the exponent has to be a certain $\alpha = \alpha_{\mathrm{end}}$ which depends on the interaction strength. On the other hand in the tube-on-metal geometry the electrons in the CN are only confined by the ends of the tube itself, and therefore the electrons tunnel from the metal contacts into the bulk of the TLL quantum wire. And this yields a different power-law exponent α_{bulk}. If the temperature is even lowered (below $\approx$50 K) the conductance drops steadily and develops roughly periodic oscillations in the gate voltage. Towards a few Kelvin the oscillations become peaks isolated by zero conductance regions. This is due to charging and single electron tunneling [57] where the segment of the nanotube between the contacts represents a quantum dot [58, 59, 60]. We discuss this phenomenon and its distinctive TLL features in the next chapter. A single impurity in a nanotube as a specimen for a single tunnel barrier in a TLL can be produced by buckle a tube [46]. The impurity can be created with an

atomic force microscope tip [61] and the sharp bend behaves like a tunnel junction. The conductance through such a barrier shows the characteristic TLL power-law dependencies. Crossings of individual nanotubes can also act as tunnel junctions [62]. In both cases the tunneling resistance of the junction is always higher than the contact resistance between the tube and the metallic electrodes.

2.3 Quantum dots

Quantum dots are structures where electrons are confined in all three spatial dimensions, the dot size being of the order of the Fermi wavelength in the host material. A quantum dot can hold a few up to hundreds of electrons. In many respects the dots behave like artificial atoms, the inverse square law Coulomb attraction between the nucleus and the electrons replaced by a linear, harmonic oscillator like force provided by the confinement. Self-consistent numerical solutions of the Schrödinger equation for heterostructures which provide confinement in all three dimensions show that the confinement can be often approximated by parabolic harmonic potential [63]. In the experiment, unlike in atoms, the number of electrons can be precisely controlled and changed during an experiment, allowing to "sweep" through the periodic table of these artificial atoms [64]. Like quantum wires and other nanostructures dots are studied with both transport measurements and optical spectroscopy, without magnetic field and in high fields. They are interesting from a fundamental physics point of view and also for their potential applications. Applications include transistors that can control currents on a single electron level. The electronic many body structure of quantum dots itself is extensively studied within Hartree–Fock approximation, density functional theory or Monte Carlo simulations. However, we want to focus on the charging effects in the DC transport through a quantum dot (which we eventually assume to be one dimensional).

Coulomb blockade and single electron tunneling

A basic effect comes into play when one tries to pass a current through a quantum dot. To do this a dot is coupled to three terminals: particle exchange can only occur between dot and the source or drain by tunneling. The third terminal provides an electrostatic or capacitative coupling and can be used as a gate electrode (fig. 6). When the tunneling resistances of the junctions are much higher than the quantum resistance h/e^2 electrons traverse the dot by sequences of uncorrelated tunneling events (*sequential tunneling*). Classically transport has to occur via a discrete change of charge e in the dot. In a simple single-particle picture this extra charge on the QD changes the electrostatic potential by the charging energy $E_c = e^2/C$ where C is the capacitance between the dot and its environment. The electronic interaction is only taken into account for in terms of the phenomenologically introduced E_c and it accounts for all the many-body effects. A microscopic description in the one dimensional case is given the following chapters. This charging energy becomes important when it exceeds the thermal energy $k_B T$. Hence, the tunneling of elec-

trons changes the electrostatic energy of the island by a discrete number. However a voltage V_g applied to the gate can change the dot's electrostatic energy continuously: if one sweeps the gate voltage a continuous number of charges $n_g = V_g C_g$ is induced (where we neglect the capacitance of the tunnel junctions). The relevant effects can be understood in terms of the following phenomenological arguments. This buildup of charge in the dot can be compensated in periodic intervals by tun-

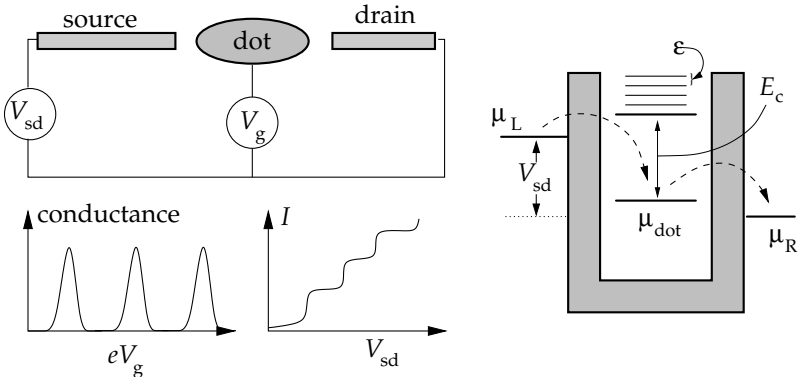

Figure 6: Left: quantum dot connected to leads source and drain and the gate (top) and sketched periodic Coulomb blockade peaks in the conductance when the gate voltage is changed (bottom, left), as well as the nonlinear I–V_{sd} and the Coulomb staircase (bottom staircase). Right: Potential landscape of dot and leads (see text).

neling of discrete charges (the electrons) on or off the island. The competition of continuous and discrete charge leads to the Coulomb blockade oscillations in the transport through a quantum dot when the source drain voltage is fixed and V_g changed. Fig. 6 (right) illustrates the situation in terms of the electrochemical potentials of the leads and dot. The states in the leads are filled up to μ_L and μ_R which are connected through $V_{sd} = (\mu_L - \mu_R)/e$. The electrochemical potential of the quantum dot is defined by the energy difference $\mu_{dot}(n) = E_0^*(n+1) - E_0^*(n)$ between two consecutive ground state energies $E_0^*(n)$ corresponding to n electrons in the dot. At zero temperature transport through the quantum dot can only occur when there are available states in the energy window between μ_L and μ_R. In particular in the linear regime ($\mu_L \approx \mu_R$) the electrochemical potentials of the leads and the quantum dot have to be aligned to allow electric current to flow. This can be achieved by tuning the gate voltage and consequently the induced charge $-en_g$. In the single particle picture of this orthodox theory [65] we have

$$\mu_{dot}(n) = \frac{e^2}{C}\left[n + \frac{1}{2} - n_g\right]. \tag{1}$$

From eq. (1) we get for the distance in the gate voltage between consecutive Coulomb oscillations $\Delta V_g/\delta = e/C = E_c/e$, where δ corrects for the difference between C_g and C and should be determined independently. The elementary charge e is taken

positive. In between the Coulomb oscillations the number of electrons is fixed and it changes by one in each cycle (from $n \rightarrow n+1$ with increasing V_g). Hence the measured distance between the Coulomb oscillations gives information about the charging energy of the dot. If there is a finite energy window eV_{sd} and the gate voltage is kept constant transport can occur through several electronic states of the dot. Anytime the source-drain voltage exceeds an integer multiple of the addition energy e^2/C a new charge channel opens and a current step occurs. Hence the nonlinear current–voltage characteristic exhibits the so called Coulomb staircase with steps at the threshold values e^2/C. In addition to the groundstate to groundstate processes also transitions can contribute that involve excited states with fixed electron numbers. Additional structure due to excited states of the dot can be discerned in nonlinear transport [66]. The level spacing between these states ε is usually much smaller than the charging energy E_c and is best observed at low temperatures in the dI/dV_{sd} where it is manifest as discrete peaks.

In the actual transport experiment there are three temperature regimes: first the high-T regime $k_B T \gg E_c$ where no single charge effects can be discerned. The conductance $\mathcal{G}_\infty$ is independent of the electron number and stems from the Ohmic combination of the two barrier conductances. Second in the *classical Coulomb blockade* regime $\varepsilon \ll k_B T \ll E_c$ many excited states are involved in the transport due to thermal excitation. The CB can be described by the so called "orthodox" theory [67, 68, 65]. The lineshape of an individual conductance peak is given by [67],

$$\mathcal{G}/\mathcal{G}_\infty = \mu[2k_B T \sinh(\mu/k_B T)]^{-1} \tag{2}$$

where μ measures the distance from the center of the peak. In this regime the maximum is independent on temperature and yields $\mathcal{G}_\infty/2$, while the width of the peak is linear in T. In the third, low temperature or *quantum Coulomb blockade* regime $k_B T \ll \varepsilon, E_c$ transport occurs only through a single level. The quantum Coulomb blockade peak has a lineshape [69]

$$\mathcal{G} = \mathcal{G}_\infty \frac{\varepsilon}{4k_B T} \frac{1}{\cosh^2[\mu/2k_B T]}. \tag{3}$$

The conductance maximum acquires a linear temperature dependence. The peak height decreases when the temperature is increased which is contrary to the high temperature behaviour. These orthodox approaches to the CB phenomenon account for the electronic interaction only in terms of the phenomenological charging energy and the transport is described in the sequential tunneling regime. A microscopic description of the many-particle system is not included.

Certainly also higher order coherent processes may occur at very low temperatures or when the coupling between the dot and the leads is strong. Then electrons tunnel coherently from one side of the dot to the other lead [70]. A prominent higher oder phenomenon is the Kondo effect in quantum dots that can occur as a spin effect [71, 72]. In contrast to first order processes -on a short time scale- virtual tunneling events can effectively flip the spin of the dot. Then the leads and the dot can form a correlated spin-singlet state which gives rise to the Kondo effect [73].

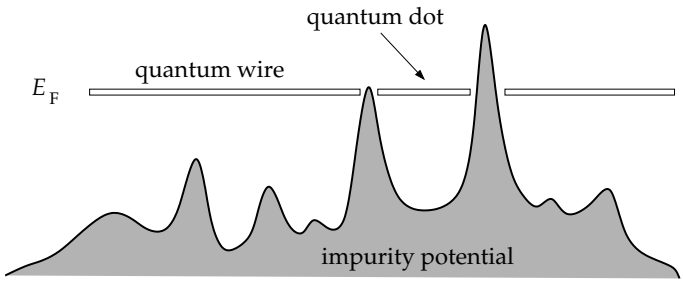

Figure 7: Sketch of the CEO wire quantum dot. The two highest impurity potentials define the tunnel junctions. The entire system (left and right quantum wire sections and the quantum dot consist of a TLL).

Below the characteristic Kondo temperature and for an odd number of electrons on the dot the conductance increases with decreasing T even in the valleys where the current is Coulomb blocked. However, we focus only on the sequential transport and Coulomb blockade effects in this thesis.

2.4 One-dimensional quantum dots

On the one hand the mutual Coulomb repulsion between the electrons leads to the above mentioned single electron phenomena. On the other hand in one dimension the interaction can be well described in terms of the TLL and causes the characteristic power-laws. In addition spin-charge separation due to the non-equal charge and spin collective excitation velocities of the respective modes can be seen in non-linear transport. Thus a combination of quantum wires and quantum dots are ideal systems to study interactions on a fundamental level. Here, we discuss two designs of one-dimensional quantum dots immersed in a quantum wire where transport measurements were performed.

CEO based 1D quantum dots

When the gates in the CEO quantum wires are increasingly biased (fig. 3) and the electron density decreased one first observes the usual conductance steps. But eventually even the lowest electronic subband is depopulated and the conductance drops to zero (upper plot in fig. 8). Then the mean electron density of the wire is so low that some maxima of the random potential of the impurities are higher than the Fermi level. First, the highest potential maximum crosses the Fermi energy, and and the wire splits into two parts. A 1D quantum island can be formed between two such potential maxima which traverse the Fermi level like in fig. 7. At temperatures lower than the charging energy of this island, the linear conductance shows several discrete peaks due to Coulomb blockade (inset of fig. 8). Transport in this regime occurs by transferring exactly one electron through the quantum island and hence a one dimensional SET is created. The system consists of a 1D quantum dot

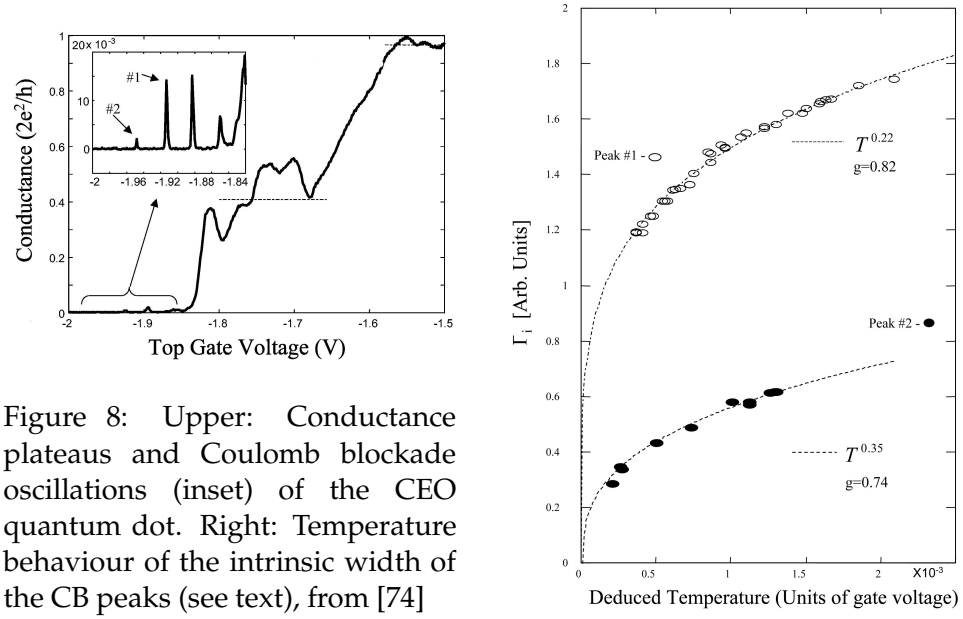

Figure 8: Upper: Conductance plateaus and Coulomb blockade oscillations (inset) of the CEO quantum dot. Right: Temperature behaviour of the intrinsic width of the CB peaks (see text), from [74]

connected to interacting TLL leads. The temperature behaviour of the CB peaks did not exhibit a simple linear dependence as expected from the orthodox approach. However, the CB peak conductance was analyzed in view of a double barrier in a TLL which predicts a power-law in temperature for the maximum of the CB peak $\mathcal{G}_{\mathrm{d}}^{\max}(T) \propto T^{1/g_0-2}$, g_0 being the interaction parameter that can have values between zero and one. fig. 8 shows the "intrinsic width" Γ_i (the integrated area below the peaks) of the two CB peaks and power-law fits to the data. Since the width of the peaks has a linear temperature dependence the power-law is $\Gamma_i \propto T^{1/g_0-1}$ theoretically. From this measurement the interaction parameter can be extracted and yields g_0 =0.74 and 0.84 and reveals the TLL behaviour of the 1D system. The different values for different peaks were attributed to the change in electron density when moving from one peak to the next. However, a significantly lower value of the g_0-parameter is expected from the charging energy of the quantum island which can be obtained from the distance between the CB peaks. The expected value is 0.4 and thus much smaller than the one extracted from the power-law [74]. We discuss a refined TLL model to match the experimental situation and geometry and elucidate this discrepancy in chapter 5.

Nanotube-based 1D quantum dots

Since the metal-nanotube contacts are mostly poor and have to be treated as tunnel junctions a CN itself between the metallic electrodes behaves as a 1D quantum dot. This becomes evident when the transport is measured at low (He) temperatures. Changing the chemical potential of the quantum dot by a gate voltage distinct Coulomb blockade peaks were observed [58, 59]. The effect of the interaction is reflected in the charging of the tube segment between the (Fermi-liquid) con-

tacts. The charging was found to be consistent with the expected self capacitance of a finite nanotube. However, the distinct TLL behaviour of the CB peaks cannot be disclosed in this geometry because the setup corresponds to a conventional quantum dot connected to leads. The peculiar nanotube feature is reflected in the relatively high charging energy and hence the high operating temperature of the SET device.

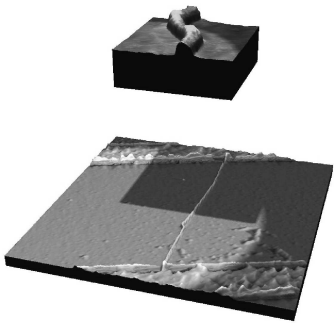

Figure 9: Double buckle nanotube device between Au electrodes on top of a Si/SiO_2 substrate. The distance between the two buckles is approximately 25nm (Copyright of this image by Cees Dekker and DIMES)

The situation where the 1D quantum dot is immersed in a nanotube quantum wire was recently achieved. Here the dot is formed by two structural defects of the tube. These kinks act as tunnel junctions and electric transport shows the typical Coulomb blockade structure [75]. The length of this segment was determined to be 120nm with a charging energy of about 20meV whereas the entire nanotube was twice as long.

A SET operated at room temperature has been made by putting an metallic nanotube between Au contacts and then manipulating the tube with the tip of an atomic force microscope [76]. In this way two buckles in a distance of 25 nm have been deliberately created as illustrated in fig. 9. Buckles in a nanotube behave much like electronic tunnel junctions [62], an hence a quantum dot is formed between the two defects. Because of the small distance between the buckles the dot has a very high charging energy of about 120meV. Therefore Coulomb blockade peaks could be observed up to temperatures of 100K (fig. 10). The temperature dependence of

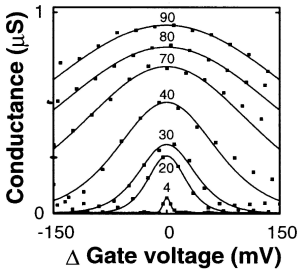

Figure 10: Coulomb blockade peaks between temperatures 4...90K of the carbon nanotube quantum dot, operated as an SET (from[76]).

the peak shape seems very peculiar. The temperature behaviour is neither what one

could expect from the orthodox theory nor from a standard TLL description. From the TLL model adapted to the characteristics of metallic nanotubes one predicts $\mathcal{G}_{\mathrm{d}}^{\max}(T) \propto T^{\alpha_{\mathrm{end}}-1} \propto T^{-0.33}$. Hence a decrease of the height of the peak is expected when the temperature is increased! The analysis of the experimental data however revealed a power-law dependence of $\mathcal{G}_{\mathrm{exp}}^{\max}(T) \propto T^{0.68}$ and showed a linear increase in temperature of the width of the CB peaks at half maximum. This experimental finding stimulated new theoretical interpretations. Some authors claimed that the unusual power-law exponent is due to a type of "correlated sequential tunneling" [77] which replaces the usual uncorrelated sequential tunneling and yields a new exponent $\alpha_{\mathrm{end-end}} = 2\alpha_{\mathrm{end}}$ which matches the observed behaviour at lower temperatures up to 30K [78]. Others tried to unify the TLL behaviour at low energies and resonant tunneling prescribed by the Breit-Wigner formula. The approach predicts exponents different from $2\alpha_{\mathrm{end}}$, and an increased conductance is expected when the temperature is decreased in a certain high temperature interval [79]. This means that the power-law does not need to be universal in all temperature regimes. An unanimous interpretation of the measured data in this intra-molecular quantum dot is not available and gives rise to discussion.

We try to explain the power-law behaviour by focusing on the effect of the metallic leads which are attached to the nanotube with the intra-tube quantum dot and find consistent temperature behaviours of the Coulomb blockade shapes (Chapter 5.4).

2.5 Summary

Quantum wires are systems where the electronic motion is restricted to one dimension by an electrostatic quantum confinement. This can be realized in semiconductor structures by elaborated gating techniques or -naturally- in molecular quantum wires. In the latter case the electronic structure of graphite yields one dimensionality in so-called single wall carbon nanotubes. Quantum wires yield a quantized conductance of e^2/h per 1D channel when Fermi liquid leads are perfectly attached. Impurities in a QW lead to power-law dependencies in temperature for the conductance in terms of the TLL model. If a one-dimensional quantum dot is immersed in a quantum wire the lineshapes of the Coulomb blockade peaks reveal characteristic power-laws in temperature due to the interaction. Hence intra-quantum wire dots are ideal systems to probe the effect of the Coulomb interaction in 1D. However transport experiments on quantum wires –both on semiconductor basis as well as on carbon nanotube basis– show unexpected temperature dependencies of the lineshapes and remain to be interpreted consistently.

3 The Tomonaga–Luttinger liquid and bosonization

In the 1950's and 1960's Tomonaga [80] and Luttinger [81] studied theoretical models for 1D metals. They found that the properties of these systems were entirely different from what was expected by Landau's Fermi liquid theory. Instead of the usual quasiparticle picture in higher dimensions, the electrons are described by collective charge and spin density waves which travel at different velocities. The latter effect is called spin charge separation and is due to the mutual Coulomb interaction of the electrons. The interaction can be characterized by a single parameter g_0 which plays a central role in the physical properties of such a 1D metal. g_0 is determined by the strength of the interaction and characterizes the degree to which the system deviates from a Fermi liquid. Tomonaga-Luttinger liquids (TLLs) exhibit features like the unusual conductivity behaviour as a function of temperature, voltage or frequency. These effects are enhanced when impurities are present. Reviews of the TLL theory are found in [15, 82, 83, 84, 85, 86]. We describe the model for spinless electrons here.

3.1 Fermi liquid – Tomonaga-Luttinger liquid

In two and three dimensions many systems of interacting fermions are well described by the Fermi liquid theory developed by Landau [87, 88]. The elementary low-energy excitations are superposition of single particle excitations and particle hole pairs, and they are called quasiparticles. The quasiparticles evolve from the states of the free Fermi gas when the interactions are switched on adiabatically. The quasiparticles posses the same quantum numbers and obey the same statistics, but their dynamic properties are renormalized by the interaction. This concept is successful because at low temperatures the phase space for scattering processes of the fermions is strongly restricted: most particles are frozen in the Fermi sea. Weakly excited particles cannot scatter into the Fermi sea, and so the lifetime τ of particles close to the Fermi surface is finite $1/\tau \sim \epsilon(\vec{k}) - E_{\mathrm{F}}$. The excitation energies are described by the poles of the one particle Green function $G(\vec{x}, t) = \langle 0|T\psi(\vec{x}, t)\psi(0, 0)|0\rangle$, where T is time ordering,

$$G(\vec{k}, \omega) = \frac{1}{\epsilon_0(\vec{k}) - \hbar\omega - \Sigma(\vec{k}, \omega)}. \tag{4}$$

Here, the self-energy $\Sigma(\vec{k}, \omega)$ contains all the many-body and interaction effects, and $\epsilon_0(\omega)$ is the bare dispersion. The imaginary part of the self-energy provides the damping of these excitations. If Σ is sufficiently analytic the solution of the equation $\epsilon_0(\vec{k}) - \hbar\omega - \Sigma(\vec{k}, \omega) = 0$ is unique, and one finds for the residue [89],

$$z_{\vec{k}} = \left[1 - \frac{\partial \mathrm{Re}\Sigma(\vec{k}, \omega)}{\hbar\partial\omega}\right]^{-1}_{\hbar\omega=\epsilon(\vec{k})}. \tag{5}$$

The residue $z_{\vec{k}}$ leads to a finite jump in momentum distribution function $n(\vec{k})$ in the ground state of a Fermi system (Fig. 11). This discontinuity is vital for the existence

of the quasiparticles. In one dimension however there are no well defined poles in

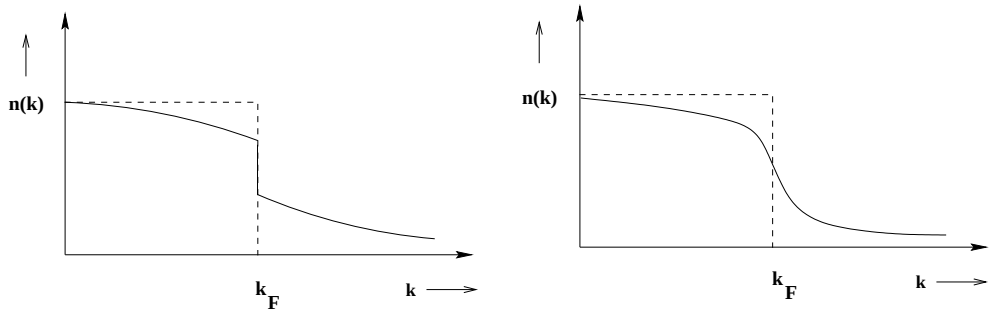

Figure 11: Momentum distribution functions $n(k)$ with discontinuity at the Fermi energy k_F for a Fermi liquid (left). Continuous distribution for interacting one-dimensional systems (right).

the Green function, and the momentum distribution function does not have a jump at the Fermi surface (consisting of two isolated Fermi points). For one dimensional interacting systems one finds[15],

$$n(k) = n(k_F) + \text{const} \times \text{sgn}\,(k - k_F)|k - k_F|^{\xi}, \tag{6}$$

The exponent ξ is a positive number whose value depends on the strength of the interaction. In the non-interacting case $\xi = 0$ such that the discontinuity is recovered. Since the quasiparticle picture breaks down in one dimension an appropriate description for interacting fermions is required. It turns out that the elementary excitations in a one dimensional system can always be written in terms of particle-hole pairs which themselves obey bosonic commutation relations[90].

3.2 Bosonization

The TLL model allows to treat an interacting electron system in strictly one dimension. If only forward scattering processes are involved correlation function can be calculated without resorting to perturbation theory. The model is limited to energies close to the Fermi surface where the dispersion of the electrons is approximately linear as depicted in Fig. 12. The linearization of the dispersion gives rise to the two branches of left and right movers, indicated by the $j = \pm$. The central ingredient is the *bosonization identity* [90, 91, 92] which allows to express the fermionic electron operator in terms of bosonic phase fields ϑ and Π (periodic boundary conditions are used where L is the system length which eventually is let to infinity $L \to \infty$)

$$\psi_{\pm}(x) = \lim_{\lambda \to 0} \frac{1}{\sqrt{2\pi\lambda}} U_{\pm}\, \mathrm{e}^{\pm i k_F x \pm i\sqrt{\pi}\vartheta(x) - i\sqrt{\pi}\int^x \mathrm{d}y\, \Pi(y)}. \tag{7}$$

k_F is the Fermi wavevector, the cutoff parameter λ is let to zero at the end of calculations, $U_{\pm}$ are unitary ladder operators which change the number of particles on

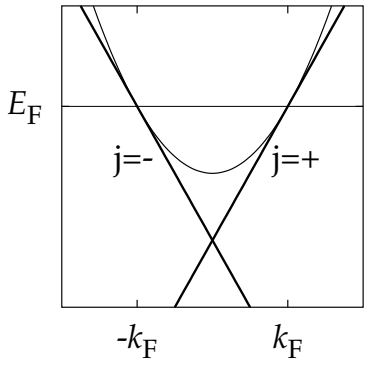

Figure 12: Linearized dispersion around the two Fermi points in 1D. This results in the two fermion species $j = \pm$ on the respective branches.

the $\pm$-branches. The fields are constructed such a way that they obey the canonical commutation relation $[\vartheta(x); \Pi(y)] = i\delta(x-y)$. They are defined in terms of the Fourier modes of the particle density operators

$$\rho_j(q) = \sum_k (c^\dagger_{j,k+q} c_{j,k} - \delta_{q,0} \langle c^\dagger_{j,k} c_{j,k} \rangle_0), \tag{8}$$

with $c^\dagger_{\pm,k}$ being the fermion creator on the $\pm$-branch. The density operators obey the commutation relation

$$\left[\rho_j(q), \rho_{j'}(q')\right] = -j\delta_{j,j'}\delta_{q,q'}\frac{qL}{2\pi}. \tag{9}$$

The explicit from of the phase fields is

$$\vartheta(x) = i\frac{\sqrt{\pi}}{L}\sum_{q\neq 0}\frac{1}{q} \mathrm{e}^{-\lambda|q|/2}\, \mathrm{e}^{-iqx}\left[\rho_+(q) + \rho_-(q)\right] + \frac{\sqrt{\pi}}{L}xN, \tag{10}$$

$$\Pi(x) = -\frac{\sqrt{\pi}}{L}\sum_{q\neq 0} \mathrm{e}^{-\lambda|q|/2}\, \mathrm{e}^{-iqx}\left[\rho_+(q) - \rho_-(q)\right] - \frac{\sqrt{\pi}}{L}J, \tag{11}$$

where $N = N_+ + N_-$ and $J = N_+ - N_-$ describe charge and current excitations formed by $N_\pm$ particles added to the ground state on the $\pm$-branches.

The TLL model comprises a local approximation of the physical model near the Fermi points in terms of the $\pm$-branches while the real electrons have a single dispersion relation. As a consequence the particle density $\rho(x) = \psi^\dagger(x)\psi(x)$ carries an additional $2k_F$ component which stems from the interference between the left and right movers in the same channel

$$\rho(x) = \rho_0 + \rho_+(x) + \rho_-(x) + \frac{k_F}{\pi}\cos[2k_F x + 2\sqrt{\pi}\vartheta(x)]. \tag{12}$$

The microscopic cutoff in eq. (7) is chosen $\lambda^2 = k_F^{-1}$, and the contribution of the operators $U^\dagger_\pm U_\mp$ changing particle numbers $N_\pm$ by one is neglected in the limit $L \to \infty$. $\rho_0 = k_F/\pi$ is the mean particle density. In general the electron density

is $-e\rho(x)$, where we take $e > 0$ and if there is an external electrical potential $U(x)$ present the charge density couples the field as

$$H_U = -e\int \mathrm{d}x\, U(x,t)\rho(x). \tag{13}$$

In the long wavelength limit $\rho(x) \approx \rho_+(x) + \rho_-(x)$, the phase fields obey the following continuity equations for the particle current j and density ρ,

$$\partial_x \vartheta(x,t) = \sqrt{\pi}\rho(x) \tag{14}$$

$$\partial_t \vartheta(x,t) = v_\mathrm{F}\Pi(x,t) = \sqrt{\pi} j(x,t). \tag{15}$$

The actual charge current and density carry the elementary charge e each. The entire Hamiltonian for electrons in one dimension interacting through the interaction potential $V(x,y)$ reads in its bosonized form

$$H_\mathrm{TLL} = \frac{\hbar v_F}{2}\int \mathrm{d}x \left[\Pi(x)^2 + (\partial_x\vartheta(x))^2\right] + \frac{1}{2\pi}\int \mathrm{d}x \int \mathrm{d}y\, \partial_x\vartheta(x) V(x,y)\partial_y\vartheta(y). \tag{16}$$

Here, the interaction is taken into account only in terms of forward scattering. An equivalent formulation in terms of real boson operators can be obtained by normalizing the density operators

$$b_q^\dagger = \sqrt{\frac{2\pi}{L|q|}}\left[\Theta(q)\rho_+(q) + \Theta(-q)\rho_-(q)\right], \tag{17}$$

$$H_\mathrm{TLL} = \hbar\sum_q \omega(q) b_q^\dagger b_q, \qquad \omega(q) = v_\mathrm{F}|q| / \sqrt{1 + \frac{\hat{V}(q)}{\pi\hbar v_\mathrm{F}}}. \tag{18}$$

$\hat{V}(q)$ is the Fourier transform of the interaction potential. In the long wavelength limit where the momentum dependence of the interaction potential can be neglected ($\hat{V}(q \to 0)$) the Hamiltonian becomes

$$H_0 = \frac{\hbar v_\mathrm{F}}{2}\int \mathrm{d}x\, \left[\Pi(x)^2 + \frac{1}{g_0^2}(\partial_x\vartheta(x))^2\right]. \tag{19}$$

The interaction is completely characterized by the *Luttinger liquid interaction parameter*,

$$g_0 = \left[1 + \frac{\hat{V}(q\to 0)}{\pi\hbar v_\mathrm{F}}\right]^{-\frac{1}{2}}. \tag{20}$$

For $0 < g_0 < 1$ the parameter describes a repulsive interaction, $g_0 = 1$ corresponds to non-interacting electrons and $g_0 > 1$ would mean an attractive interaction between the electrons. The equations (7)-(20) basically comprises what is called the *Tomonaga–Luttinger liquid model* (TLL). In the thermodynamic limit ($L \to \infty$) a variety of effects can be revealed utilizing analytic methods non perturbatively.

Attempts of bosonization in higher dimensions were made but did not lead to satisfactory results [93]. To exploit the bosonization machinery strictly 1D systems are necessary. Finite size effects and bosonization for the TLL are discussed in [94, 95, 96] and correlation functions are calculated there. Open boundaries in order to treat tunneling into the ends of quantum wires are studied in [97]. Bosonization can also be employed on the Hubbard model and shows the separation of spin and charge excitations in one dimension [98]. The spin-$\frac{1}{2}$ Heisenberg chain may also be treated by bosonization after mapping to a spinless fermion problem. Then various correlation functions can be calculated [99].

3.3 Conductivity of a TLL quantum wire

The fingerprint of a noninteracting 1D system is its quantized conductance in multiples of the universal value $\mathcal{G}_0 = e^2/h$. Then, the transport is ballistic throughout the wire of length L, and one can use the Drude conductivity $\sigma = e^2\rho_0\tau/m_*$. We have for the relaxation time $\tau = L/v_\mathrm{F}$, and the (spinless) electron density is $\rho_0 = k_\mathrm{F}/\pi$ where $k_\mathrm{F} = m_* v_\mathrm{F}/\hbar$. Taking into account that electrons can travel either to the left or right by a factor one half the conductance σ/L is quantized in the units $\mathcal{G}_0 = e^2/h$ for one channel. If subsequent 1D electronic subbands are filled the conductance appears as a series of plateaus with values equal to $\mathcal{G}_\mathrm{Q} = \mathcal{G}_0$ multiplied with the number of wire modes.

However, in the presence of interactions the conductance for an infinitely long quantum wire, modeled as a TLL, is renormalized by the interaction parameter g_0 [16]. Using the Kubo formula [100, 101] and calculating the correlators in the bosonized forms one gets the conductivity: the average current $I(t)$ is related to a driving electric field $E(x,t)$ via

$$I(t,x) = \int \mathrm{d}y \int \frac{\mathrm{d}\omega}{2\pi}\, \mathrm{e}^{-i\omega t}\sigma(x,y,\omega)E(y,\omega). \tag{21}$$

The nonlocal conductivity $\sigma(x,y,\omega)$ is obtained by the Kubo formula at the Matsubara frequencies $\omega_n = 2\pi n/\beta$ with the inverse temperature $\beta = 1/k_\mathrm{B}T$ and imaginary time τ,

$$\sigma(x,y,\omega) = \frac{e^2}{\omega}\int_0^{\hbar\beta} \mathrm{d}\tau \langle T_\tau j(x,\tau)\, j(y,0)\rangle \mathrm{e}^{-i\omega_n\tau}\Big|_{\omega_n=-i\omega+0^+}. \tag{22}$$

The imaginary time ordered current-correlator can be calculated by using the explicit bosonized forms in eqs. (11) and (15). This gives

$$\sigma(x,y,\omega) = \frac{2e^2}{h}\omega_n\, G_{\omega_n}(x,y), \tag{23}$$

where $G(x,y;\tau,\tau') = \langle T_\tau[\vartheta(x,\tau)\vartheta(y,\tau')]\rangle$, is the time ordered Green function for the model (see appendix A). We obtain the DC conductivity by taking the limit $\omega_n \to 0$. The Green function corresponding to the TLL Hamiltonian in eq. (19) has a simple form and gives rise to the DC conductance $\mathcal{G} = e^2 g_0/h$. The AC-transport

properties of infinite quantum wires even with long range interactions were studies in [102, 103]. However, experimentally probed quantum wires are always of finite length and they are connected to Fermi liquid leads. Experiments showed that clean ballistic wires exhibit an almost perfectly quantized conductance in terms of $\mathcal{G}_0$ when measured at relatively high temperatures. This was explained by including Fermi liquid leads that apparently determine the conductance completely. In [19, 104] the transmission and transport through a finite, clean wire modeled by a stepwise constant interaction parameter (g_1 on a length L that describes the quantum wire region and g_0 elsewhere that characterizes the leads) is calculated. This was done by writing the time evolution of the current j and a generalization of the Landauer formula. The DC conductance then only depends on the g_0, which is set to unity to model Fermi liquid leads. Also employing the Kubo formula and calculating the Green function for such a piecewise constant interaction parameter leads to an unrenormalized DC conductance e^2/h for a one channel TLL quantum wire [17, 18]. This is also true if an additional intermediate step in the interaction parameter value is included $g_1 \leq g_3 \leq g_0 = 1$ [105]. Alternatively, one can interpret the perfect conductance in terms of a compensating renormalized electric driving field [20, 21]. Then the renormalized driving field exactly cancels the renormalization effect on the conductivity. Hence, even a clean 1D quantum wire with interacting electrons exhibits the bare conductance quantum when it is contacted by Fermi liquids. So, the conductance behaves as predicted by models for noninteracting 1D electrons [106, 107, 108]. Distinct TLL features come into play when impurities are present in the quantum wire.

3.4 Impurity potentials in a Luttinger liquid

If one introduces an impurity in a TLL, which can be a barrier, a constriction, a localized impurity or a geometrical defect (in CNs), the quantum wire becomes insulating at zero temperature (provided that a repulsive interaction is assumed) [109]. A nonmagnetic impurity at the position x_i couples to the charge density $\rho(x)$ and causes backscattering with $2k_\mathrm{F}$ momentum transfer. The Hamiltonian for a single localized impurity $H_\mathrm{i} = \int \mathrm{d}x\, \psi^\dagger(x) U_\mathrm{imp}(x) \psi(x)$ is obtained from eq. (12) and yields

$$H_\mathrm{i} = V_\mathrm{i}\rho_0 + \frac{V_\mathrm{i}}{\sqrt{\pi}} \left.\frac{\vartheta(x)}{\partial x}\right|_{x=x_\mathrm{i}} + U_\mathrm{i} \cos[2k_\mathrm{F}x_\mathrm{i} + 2\sqrt{\pi}\vartheta(x_\mathrm{i}, t)], \tag{24}$$

where the impurity potential is $U_\mathrm{imp}(x) = V_\mathrm{i}\delta(x - x_\mathrm{i})$, and $U_\mathrm{i} = V_\mathrm{i}\rho_0$. The first constant term in eq. (24) only shifts the energy scale, and the second term can be eliminated by a unitary transformation of the complete Hamiltonian $H_0 + H_\mathrm{i}$ [eqs. (19) and (24)]. We will always omit these two terms in the following.

The current through the entire system is determined through the current at the barrier at x_i, and therefore we need to evaluate $\partial_t \vartheta(x_\mathrm{i}, t) \propto j(x_\mathrm{i})$ [from eq. (15)]. The Hamiltonian $H_0 + H_\mathrm{i}$ can be interpreted as a potential model with the variable $\vartheta(x_\mathrm{i})$, coupled to a harmonic bath which is composed of the fields $\vartheta(x \neq x_\mathrm{i})$ in

H_0. Integrating out all degrees of freedom other than $\vartheta(x_\mathrm{i}) \equiv \theta_\mathrm{i}$ we get an effective Euclidean action (see Appendix C.1)

$$S_\mathrm{eff}[\theta_\mathrm{i}] = \frac{1}{2\beta}\sum_n \frac{\theta_\mathrm{i}(\omega_n)\theta_\mathrm{i}(-\omega_n)}{G_{\omega_n}(x_\mathrm{i},x_\mathrm{i})} + U_\mathrm{i}\int_0^{\hbar\beta} \mathrm{d}\tau \cos[2k_\mathrm{F}x_\mathrm{i} + 2\sqrt{\pi}\theta_\mathrm{i}], \tag{25}$$

where G_{ω_n} is again the Fourier transform of the Green function. The electric current is given by the time evolution of $\theta_\mathrm{i}(t)$. That such an impurity potential at zero temperature is equivalent to a weak link and therefore electronic transport is only possible by tunneling of electrons from one side of the barrier to the other can be seen from a renormalization group analysis of the action (25). We apply a renormalization group transformation on the corresponding partition function $\int \mathcal{D}\theta \exp[-S_\mathrm{eff}]$ in Appendix D by integrating out fast modes θ_f with $|\omega| > \mu$ (where the energy μ separates slow from fast modes) and rescaling the remaining frequencies. The scaling flow equation for the impurity potential strength U_i reads

$$\frac{\mathrm{d}U_\mathrm{i}}{\mathrm{d}l} = (1-g_0)\,U_\mathrm{i}(l), \tag{26}$$

where $\mathrm{d}l = -\mathrm{d}\ln\mu$. This means that whenever $0 < g_0 < 1$ an initially small barrier scales to the fixed point at ∞ as shown in Fig. 13. Hence, a single impurity in a TLL

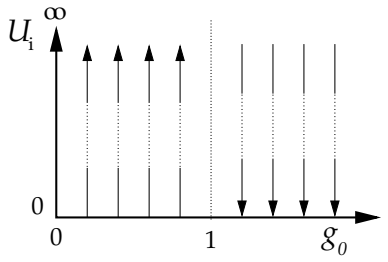

Figure 13: Renormalization flow of the delta-impurity strength U_i in a TLL as a function of the TLL interaction parameter g_0.

is completely insulating and electronic transport is limited to tunneling through it. On the other hand if interactions are attractive ($g_0 > 1$) the barrier scales to zero, and the DC conductance should have the perfect value $e^2 g_0/h$. In the noninteracting case $g_0 = 1$ the impurity strength remains invariant under renormalization, and transport is determined by the transmission probability of the barrier.

Interrupting the renormalization flow at low but finite energies an effective barrier height $U_\mathrm{i} \propto \epsilon^{g_0-1}$ (to leading order) must be considered and power-law corrections to the conductance are expected. Indeed, weak scattering at random impurities gives rise to deviations $\delta\mathcal{G}$ from the universal conductance steps [110, 40, 111]. The deviation acquires a temperature dependence connected to the interaction parameter through $\delta\mathcal{G} \propto T^{f(g_0)}$ where f is a rational function of g_0. Another approach starts off from of a one-dimensional Wigner crystal which is pinned by an arbitrary impurity potential [112]. In this situation also power-laws in temperature are predicted for the conductance where the exponent stems from the electrostatic energy of the electrons in the crystal. Hence, power-laws in the temperature dependence of the conductance plateaus are due to the electronic interaction and therefore distinct TLL behaviour.

Tunneling through a high barrier

At low energies, traversal of a high potential barrier is by tunneling, equivalent to the transport of electrons through a tunnel junction [109]. The transport is induced by an external driving potential $U(x)$ which couples to the electron density and causes only forward scattering. In principle also the $2k_{\mathrm{F}}$-part of the density appears [eq. (12)], however we assume the driving potential very smooth with a drop of magnitude U only at the barrier position. Then all backscattering can be attributed to the strong impurity potential. The corresponding electrostatic energy is then given by

$$H_U = -\frac{eU}{\sqrt{\pi}}\,\theta_{\mathrm{i}}, \tag{27}$$

and needs to added to the effective action in eq. (25). The electronic transport is characterized by the evolution of θ_{i}, influenced by the bulk modes away from the barrier position. In the action (25) a strong impurity potential means extremely deep minima of the cosine term. Then, the variable θ_{i} can be assumed to acquire only discrete values $\theta_{\mathrm{i}}(t) = n\sqrt{\pi}$. For example a change by $\Delta n = 1$ corresponds to the transfer of one electron through the barrier. In order to calculate the current the transition probabilities $P_n(t)$ from an initial state $\theta_{\mathrm{i}}^{\mathrm{i}}$ at $t = 0$ to a final state $\theta_{\mathrm{i}}^{\mathrm{f}}(t) = n\sqrt{\pi}$, $n = 1, 2, 3\ldots$ are required. For an initially prepared state $\theta_{\mathrm{i}}^{\mathrm{i}}(0) = 0$ the expectation value at time t is the sum over all possible values $\theta_{\mathrm{i}}^{\mathrm{f}}(t)$ weighted with the corresponding probability

$$\langle\theta_{\mathrm{i}}(t)\rangle = \sqrt{\pi}\sum_n nP_n(t). \tag{28}$$

Using the continuity equation (15) the electric current is then the derivative with respect to time

$$I(t) = -\frac{e}{\sqrt{\pi}}\langle\partial_t\theta_{\mathrm{i}}(t)\rangle = -e\sum_n n\dot{P}_n(t) \tag{29}$$

The action $S_{\mathrm{eff}}[\theta_{\mathrm{i}}] + H_U[\theta_{\mathrm{i}}]$ resembles the action of a Brownian particle moving in a tilted periodic washboard potential coupled to a dissipative environment. This problem has been extensively studied [113, 114]. We use the known results from the quantum Brownian motion problem to determine the average steady current. Usually, the time evolution of the average current is governed by the density functional for the model in consideration. The matrix elements of the density functional contain the $P_n(t)$, and they can be obtained by imaginary time pathintegrals. The method is briefly sketched in appendix B and leads to the formal solution for the probabilities P_n,

$$P_n(\theta_{\mathrm{i}}^{\mathrm{f}}, t; \theta_{\mathrm{i}}^{\mathrm{i}}) = \int \mathcal{D}\theta_{\mathrm{i}}\mathcal{D}\theta_{\mathrm{i}}' A_0[\theta_{\mathrm{i}}]A_0^*[\theta_{\mathrm{i}}']\mathcal{F}[\theta_{\mathrm{i}}, \theta_{\mathrm{i}}'], \qquad \mathcal{F}[\theta_{\mathrm{i}}, \theta_{\mathrm{i}}'] = \mathrm{e}^{\Phi[\theta_{\mathrm{i}}, \theta_{\mathrm{i}}']}, \tag{30}$$

$$\Phi[\theta_{\rm i}(t),\theta_{\rm i}'(0)] = \frac{1}{\pi\hbar}\int_0^t {\rm d}t_2 \int_0^t {\rm d}t_1 \left[\dot\theta_{\rm i}(t_2) - \dot\theta_{\rm i}'(t_2)\right] \times \\ \times \left[W(t_2-t_1)\dot\theta_{\rm i}(t_1) - W^*(t_2-t_1)\dot\theta_{\rm i}'(t_1)\right], \tag{31}$$

$$\ln A_0[\theta_{\rm i}] = -\frac{i}{\hbar}\int_0^t {\rm d}t' \left[U_{\rm i}\cos[2k_{\rm F}x_{\rm i} + 2\sqrt{\pi}\theta_{\rm i}(t')] + \frac{eU}{\sqrt{\pi}}\theta_{\rm i}(t')\right]. \tag{32}$$

The functional $A_0[\theta_{\rm i}]$ gives the probability amplitude without coupling to the bulk modes $\vartheta(x \neq x_{\rm i})$. A tunneling event which is characterized by a change of $\theta_{\rm i}$ from one minima to the other yields $i\Delta/2$. This tunneling probability amplitude depends on the actual phenomenology of the barrier/tunnel junction. Without any influence due to the Feynman–Vernon influence functional $\mathcal{F}[\theta_{\rm i},\theta_{\rm i}']$ the tunneling rate would be $\Delta^2/4$. This corresponds to tunneling of a single electron through the barrier. We consider only processes up to Δ^2 and hence neglect higher oder processes due to multi-electron transfers through the barrier. The effect of the harmonic bath of the bulk modes is captured by the influence functional $\mathcal{F}[\theta_{\rm i},\theta_{\rm i}']$ which contains the kernel

$$W(t) = \int_0^\infty {\rm d}\omega \frac{J_{\rm b}(\omega,x_{\rm i})}{\omega^2}\left[\frac{1-\cos\omega t}{\tanh\beta\hbar\omega/2} + i\sin\omega t\right]{\rm e}^{-\omega/\omega_{\rm c}}, \tag{33}$$

with a high energy cutoff $\omega_{\rm c}$. The spectral density $J_{\rm b}(\omega,x_{\rm i})$ is obtained from the kernel of the quadratic term in the effective action (25) by analytic continuation $\omega_n \to -i\omega$,

$$J_{\rm b}(\omega,x_{\rm i}) = -{\rm Im}\frac{1}{G_{-i\omega}(x_{\rm i},x_{\rm i})}. \tag{34}$$

The spectral density contains the effect of the correlations in the system through the Green function. We calculate the stationary current for large times t considering only the low-order processes $n = \pm 1$ of the order Δ^2. This corresponds to incoherent tunneling of single electrons through the high barrier and suffices for an analysis of linear transport. Then the current through the barrier is determined by the forward and backward tunneling rates γ and $\bar\gamma$ which are the asymptotic values of $\dot P_{\pm1}(t\to\infty)$. The expression for the current eq. (29) simplifies to

$$I(t) = e\left[\gamma(eU) - \bar\gamma(eU)\right], \tag{35}$$

and we have for the sequential forward tunneling rate

$$\gamma(eU) = \frac{\Delta^2}{4}\int_{-\infty}^{\infty}{\rm d}t\ {\rm e}^{\,ieUt/\hbar - W(t)} \tag{36}$$

The backward tunneling rate obeys the principle of detailed balance [115] $\bar\gamma(eU) = \gamma(-eU) = \exp(-\beta eU)\gamma(eU)$. The eqs. (29)–(36) provide a closed solution for the tunneling current through a high barrier in a TLL. For the model of a TLL with homogeneous zero-range interaction that is only characterized by the parameter

g_0 we have the Green function $G_{\omega_n}(x_\mathrm{b}, x_\mathrm{b}) = g_0/2\omega_n$ which is independent of the barrier position. This yields for the spectral density

$$J_\mathrm{b}(\omega) = 2\omega/g_0. \tag{37}$$

In this case the rate integrals can be calculated exactly [116] and we get

$$\gamma(E) = \left(\frac{\Delta}{2}\right)^2 \frac{1}{\omega_\mathrm{c}} \frac{\mathrm{e}^{\beta E}}{2} \Gamma(2/g_0) \left(\frac{\hbar\beta\omega_\mathrm{c}}{2\pi}\right)^{1-2/g_0} \left|\Gamma\left(\frac{1}{g_0} + i\frac{\beta E}{2\pi}\right)\right|^2. \tag{38}$$

$\Gamma(\cdot)$ is the gamma function with complex arguments. From the current $I(U) = e[1 - \mathrm{e}^{-e\beta U}]\,\gamma(eU)$ the linear conductance $I(U)/U$ for $U \to 0$ of such a tunnel junction is determined

$$\mathcal{G}_\mathrm{b}(T) = \frac{1}{R_\Delta} \frac{\Gamma^2(1/g_0)}{\Gamma(2/g_0)} \left(\frac{2\pi k_\mathrm{B} T}{\hbar\omega_\mathrm{c}}\right)^{2/g_0 - 2}. \tag{39}$$

Here, $R_\Delta = 2\hbar\omega_\mathrm{c}^2/\pi e^2\Delta^2$ describes the intrinsic tunneling resistance of the junction without interaction effects. The conductance shows a typical power-law in temperature dependence explicitly on the interaction through g_0. Since a high and localized delta-impurity effectively cuts the TLL, the formula (39) describes tunneling between two semi-infinite TLL quantum wires connected by a tunnel junction that is characterized by the matrix element Δ. One could also pursue a model where from the beginning two TTLs with open boundaries are considered, and the tunneling rates are calculated by the Fermi golden rule [97]. Such a perturbative approach has the advantage that tunneling between different wires can be described as well. For instance if electrons tunnel from a metallic Fermi liquid lead (g_0 =1) into the end of a TLL one needs to replace $2/g_0 \to 1 + 1/g_0$ in equation (39). The temperature dependence of the conductance of a TLL–FL contact has a power-law [109, 117],

$$\mathcal{G}_\mathrm{c}(T) \propto T^{1/g_0 - 1}. \tag{40}$$

The single barrier problem in a TLL was first studied in [16, 22]. This was done by deriving the effective action and mapping on the Caldeira–Leggett model [118]. The problem was also approached by use of conformal invariance, and one succeeded to map onto an integrable model (the boundary sine-Gordon model) [119]. A tunnel junction realized by two semi-infinite TLLs with open boundary conditions and a long range interaction was investigated in [120]. The role of contacting the TLL with a single barrier potential was studied in terms of the piece-wise constant interaction parameter model in [121]. This approach predicts two asymptotic power-law exponents either for very low or hight temperatures corresponding to the two values g_0 or g_1. The AC transport properties of a TLL with a tunnel barrier are treated in [122].

A natural step towards a quantum wire with disorder is the inclusion of a second barrier as an impurity in the TLL quantum wire. It is then possible to have resonant transmission. For strong barriers this happens when the energy on the

island between the two barriers, which practically constitutes a quantum dot, is degenerate for two charge states. This can be arranged by tuning the chemical potential of the island through an attached gate voltage [109]. The situation is equivalent to the Coulomb blockade (CB) physics as outlined in chapter 2.4. The shape of the CB peaks and their temperature behaviour depend in a power-law fashion on the interaction strength. A microscopic description for the charging energies and a detailed model of this single electron tunneling in terms of a refined TLL model is given in the following chapter 4.

3.5 Summary

Let us summarize the principal properties of one-dimensional interacting electron systems which can be describes in terms of the TLL model and bosonization.

In one dimension no quasiparticles exist but rather collective spin and charge excitations. Bosonization is a nonperturbative method. In the TLL model a continuum theory of *interacting fermions* can be translated into a theory of *non-interacting bosons* and solved exactly. Only forward scattering is taken into consideration. The bosonized theory has decoupled spin and charge components which are not manifest in the fermionic language. The TLL model is valid at low energies in the vicinity of small multiples of k_F. Bosonization is strictly limited to one-dimensional systems. The interaction is manifest in a single parameter g which appears as a power-law exponent in various physical quantities.

4 Transport through a one-dimensional quantum dot immersed in a TLL

In experiments for probing Luttinger liquid behavior a quantum dot is often realized by by two localized impurities. This can be done by lowering the electronic density in a one-dimensional system (like in the CEO wires) and hence lowering the Fermi energy. Eventually impurity potential traverse the Fermi energy and build impurity potentials in the dot. If the wire is tuned in a way that only two of those potentials are traversing the Fermi energy a quantum dot is created. On the other hand controlled impurities can be formed by tipping nanotubes which themselves are realizations of one-dimensional electron systems. By tipping the tube one can create buckles in the nanotube which represent tunnel barriers. From these considerations we model the before mentioned experimental setup with a Luttinger liquid quantum wire plus two localized $\delta-$like impurity potentials.

4.1 Double barrier structure as a quantum dot

Two high barriers at the positions $x_1 < x_2$ that form the one-dimensional quantum dot of length $a = x_2 - x_1$ yield the Hamiltonian

$$H_{\text{dot}} \sum_{n=1,2} U_n \cos\left[2k_{\text{F}}x_n + 2\sqrt{\pi}\vartheta(x_n)\right]. \tag{41}$$

Again, as in the one-impurity scenario, we attribute the backscattering only to the the barrier potential. We also assume potential drops only at the barrier positions and an otherwise smooth driving field. Then the electric potential landscape that realizes the driving voltage through the system couples to the long wavelength part of the charge density,

$$H_U = -\frac{e}{\sqrt{\pi}} \int \mathrm{d}x\, U(x,t)\partial_x\vartheta(x,t). \tag{42}$$

Eventually the form of $U(x,t)$ will be further specified as to describe a source-drain voltage at the quantum dot (constant in the region $x < x_1$ and $x > x_2$ respectively) and a gate voltage to shift the chemical potential of the quantum dot (only present at $x_1 < x < x_2$). This configuration corresponds to two tunnel junctions which cut the TLL wire into the three regions: the actual quantum dot part between x_1 and x_2, and the two leads parts $x < x_1$ and $x > x_2$. The electrons will tunnel one-by-one through the junctions which corresponds to changes in the impurity modes by $\sqrt{\pi}$ as for the single barrier.

4.2 The effective action

For the transport through the double barrier structure it is sufficient to know the time evolution of the phase fields at the two barrier positions $\theta_i(\tau) = \vartheta(x_i,\tau)$. The average current through the entire system is written as

$$I(t) = -\frac{e}{2\sqrt{\pi}}\left[\langle\dot{\theta}_1(t)\rangle + \langle\dot{\theta}_1(t)\rangle\right] \equiv -\frac{e}{2}\langle\dot{N}_+(t)\rangle. \tag{43}$$

The brackets $\langle \dots \rangle$ here denote the average performed with the reduced density matrix for the degrees of freedom at $x = x_1, x_2$. Hence, we can derive an effective action only for the $\theta_i(t)$ which we write in terms of of the (anti-) symmetric combinations,

$$N_\pm := \frac{1}{\sqrt{\pi}} \left[\theta_2 \pm \theta_1\right]. \tag{44}$$

N_- describes the number of additional particles in the dot with respect to the average number in the ground state $n_0 = a\rho_0$ where $a = x_2 - x_1$ is the length of the dot and $\rho_0 = k_\mathrm{F}/\pi$ the mean particle density of the wire. The variable N_+ measures the particles transfered through both barriers.

To block the two modes θ_i and integrate out the superfluous degrees of freedom $\vartheta(x \neq x_i, \tau)$ two delta functionals are introduced. The calculation of the effective action is given in the appendix C.2. We can write the effective action for a double barrier in a Tomonaga-Luttinger liquid quantum wire with an external driving potential $U(x)$ in the form

$$S_\mathrm{eff}[N_+, N_-] = S_1[N_+, N_-] + S_U[N_+, N_-] + S_\mathrm{dot}[N_+, N_-]. \tag{45}$$

The effect of the bulk modes and of the electronic interaction is contained in the S_1 and S_U parts of the effective action. They can be written as,

$$S_1[N_+, N_-] = \frac{1}{2\beta} \sum_{n,r=\pm} N_r(\omega_n) K_r(\omega_n) N_r(\omega_n) \tag{46}$$

$$S_U[N_+, N_-] = \frac{1}{2} \sum_{n,r=\pm} E(x, \omega_n) N_r(\omega_n)) L_r(x, \omega_n). \tag{47}$$

The particular forms of the kernels $K_\pm(\omega_n)$ and $L_\pm(x, \omega_n)$ depend on the specific assumptions of the model. They can be specified for different cases of the electronic interaction, like long range or short range, homogeneous or nonhomogeneous interaction strength, or the true configuration of the electric field. In any case the effective action can be written in the from above as quadratic form in the variables $N_\pm$.

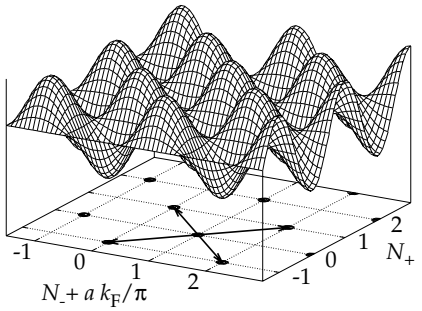

Figure 14: Impurity potential term of eq. (49) in the $(N_+, N_- + ak_\mathrm{F}/\pi)$-space. The arrows on the base indicate the most significant processes for high barriers where only nearest neighbour minima are connected, each contributing the tunneling matrix element Δ.

The part $S_{\rm dot}$ corresponds to the action stemming from eq. (41). The explicit form of this dot action for equal barriers $U_1 = U_2 = U_{\rm imp}$ reads in terms of the $N_\pm$,

$$S_{\rm dot}[N_+, N_-] = U_{\rm imp} \cos \pi N_+ \cos\left[\pi N_- + k_{\rm F} a\right] \tag{48}$$

$$\equiv U_{\rm imp} \cos \pi N_+ \cos \pi n, \tag{49}$$

where $n = N_- + n_0$ is the number of electrons in the dot.

The shape of this potential term is illustrated in Fig. 14. The effective action in eq. (45) resembles the action for a Brownian particle characterized by the coordinates (N_+, n) in a two-dimensional washboard potential. We use the same approach as in the single barrier case where the particle was subject to a tilted one-dimensional washboard potential. For very high impurity potentials the minima which are indicated by the dots on the projection in fig. 14 are very deep. These are the stationary states for $\vec{N} \equiv (N_+, n)$. A change can only occur between the minima and is characterized by the appropriate tunneling matrix element Δ. The arrows in fig. 14 describe the energetically preferred transitions from the chosen state (0,1). Varying $\vec{N}$ corresponds to electron tunneling through a barrier. Transitions are most favorable between nearest neighbour minima in the potential landscape and can be identified with electron tunneling through one of the barriers (the basic tunneling events are shown in fig. 15).

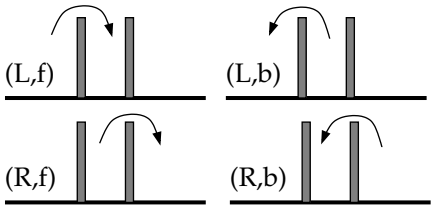

event	n'	N'_+
(L,f)	$n+1$	$N_+ - 1$
(L,b)	$n-1$	$N_+ + 1$
(R,f)	$n-1$	$N_+ - 1$
(R,b)	$n+1$	$N_+ + 1$

Figure 15: The basic tunneling processes through the double barrier: forward (f) and backward (b) through either the left (L) or right (R) barrier and the corresponding changes in N_+ and n.

Any of the four processes forward (f), i.e. to the right, and backward (b) tunneling through each of the two barriers, i.e left (L) or right (R) is characterized by a change in (N_+, N_-). For instance the tunneling process (R,f) is mapped onto the transition $n \to n-1$ and $N_+ \to N_+ - 1$.

4.3 Sequential electron tunneling rates

To calculate the stationary current for through the quantum dot structure the evolution of $N_+(t \to \infty)$ is needed [eq. (43)]. The brackets $\langle \cdot \rangle$ include the thermal and a statistical average with the reduced density matrix for the degrees of freedom corresponding to the two impurity modes at $x_{1,2}$. The conditional probabilities of finding $(\vec{N}_{\rm f}, t; \vec{N}_{\rm i})$ for the initial state $\vec{N}_{\rm i}$ at time zero and the final state $\vec{N}_{\rm f}$ at time t

is, as in the single barrier problem, written in terms of the pathintegrals,

$$P(\vec{N}_{\rm f},t;\vec{N}_{\rm i}) = \int \mathcal{D}\vec{N}\mathcal{D}\vec{N}' A_0[\vec{N}]\; A_0^*[\vec{N}']\; \mathcal{F}[\vec{N},\vec{N}'], \tag{50}$$

$$\mathcal{F}[\vec{N},\vec{N}'] = {\rm e}^{\Phi(\vec{N},\vec{N}')} \equiv {\rm e}^{\Phi_+(N_+,N_+')+\Phi_-(N_-,N_-')} \tag{51}$$

$$\begin{aligned}\Phi_r[N_r,N_r'] =& i\delta_{r,-}\frac{\mu}{2\hbar}\int_0^t {\rm d}t_1\left[N_r^2(t_1)-N_r'^2(t_1)\right]\\ &+\int_0^t {\rm d}t_2\int_0^{t_2}{\rm d}t_1\left[\dot N_r(t_2)-\dot N_r'(t_2)\right]\\ &\times\left[W_r(t_2-t_1)\dot N_r(t_1)-W_r^*(t_2-t_1)\dot N_r'(t_1)\right],(r=\pm)\end{aligned} \tag{52}$$

$$\ln A_0 = -\frac{i}{\hbar}S_U[N_+(t),n(t)] - \frac{i}{\hbar}S_{\rm dot}[N_+(t),n(t)]) \tag{53}$$

$A_0[\vec{N}]$ is the probability amplitude of following the paths $N_+(t)$ and $n(t) = N_-(t) + n_0$ without the coupling to the bulk modes and gives $i\Delta/2$ for tunneling through one of the barriers. We tacitly specified a field configuration that mimics a connection of the quantum dot to a source-drain voltage $V_{\rm sd}$ and a gate voltage $V_{\rm g}$:

$$U(x,t) = \begin{cases} -V_{\rm sd}/2 & \text{for} \quad x < x_1 \\ V_{\rm g} & \text{for} \quad x_1 < x < x_2 \\ V_{\rm sd}/2 & \text{for} \quad x > x_2 \end{cases} \tag{54}$$

$$S_U = -\frac{eV_{\rm sd}}{2}N_+ - e\,\delta\,V_{\rm g}n. \tag{55}$$

The parameter δ is introduced because the gate voltage is usually coupled capacitively to the quantum dot, and one has to take into account the capacitances of the gate $C_{\rm g}$ and the quantum dot C. Here, we let $\delta = C_{\rm g}/C$. We assume that the source-drain voltage drops equally at the barriers. Eventually we calculate the linear current and take the limit $V_{\rm sd} \to 0$. Thus our assumption will not affect the results. The Feynman–Vernon influence functional $\mathcal{F}[\vec{N},\vec{N}']$ [123] captures the effects of the interactions and contains the two dissipative kernels $W_r(t)$. They are obtained from the kernels $K_\pm(\omega_n)$ in the Euclidean effective action above (45) via

$$W_r(t) = \int_0^\infty {\rm d}\omega\;\frac{J_r(\omega)}{\omega^2}\left[\frac{1-\cos\omega t}{\tanh\beta\hbar\omega/2}+i\sin\omega t\right], \tag{56}$$

To ensure convergence an exponential cutoff is introduced where $\omega_{\rm c}$ exceeds any other energy in consideration. The function $J_r(\omega)$ is the spectral density which is directly related to the kernel $K_r(\omega_n)$ in the effective action eq. (45). We obtain the spectral densities $J(\omega)$ by analytic continuation

$$J_r(\omega) = -{\rm Im}\frac{1}{\pi}K_r(\omega_n\to -i\omega). \tag{57}$$

The mass term μ in eq. (52) relates to the charging energy E_c of the quantum dot and is the local part of the kernel

$$E_c = \frac{\hbar}{2} K_-(\omega_n \to 0). \tag{58}$$

The equations (50)-(57) represent a formal solution for the time evolution of $N_+(t)$ and lead the electric current through the quantum dot immersed in the Luttinger liquid quantum wire [from eq. (43)],

$$I = \frac{e}{2} \lim_{t\to\infty} \sum_{\vec{N}_f} N_{+,f}\, \dot{P}(\vec{N}_f, t; \vec{N}_i). \tag{59}$$

The relevant paths which describe a charge transfer from the left or right lead through the two barriers involve a change of N_+ by $\Delta N_+ = 2$. Let us note that we will not consider direct transitions where $N_+ \to N_+ \pm 2$ and simultaneously $n = \text{const}$, because they require the penetration of of much higher barriers. This can be seen in fig. 14 for a transition from (0,3) to (2,3) which means surmounting the maximum between start and end point. On the other hand the processes that involve changes ΔN_+, $\Delta n = \pm 1$ entail tunneling through lower barriers. Therefore, in our model the transport of electrons through the double barrier takes place in two steps: first tunneling from the left (right) lead into the dot, second tunneling from the dot to the right (left) lead. The paths for the integration in eq. (50) are

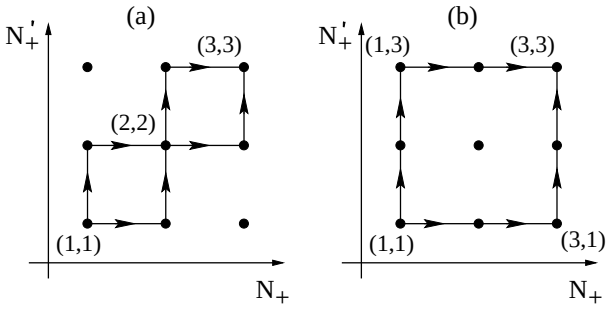

Figure 16: Paths of the (a) sequential tunneling process (b) coherent process.

shown in fig.16 in the (N_+, N'_+) plane. The left diagramme (a) shows the *sequential tunneling* where the tunneling events through the left and right barrier are uncorrelated. With the boundary conditions $N_+(0) = N_+(0)' = 1$ and $N_+(t) = N'_+(t) = 3$ four paths that cross the point (2,2) are possible. The sojourn at the diagonal point (2,2) implies that an electron actually resides in the dot between the to uncorrelated tunneling events leading to the state (3,3). On the contrary the two paths that do not cross the main diagonal (right in fig. 16) correspond to cotunneling (b). Those processes are not considered here. A discussion of the higher order cotunneling process is found in [124].

Let us calculate the tunneling rates $\Gamma(E)$ of the four sequential events depicted in fig. 15 as the time derivative of the conditional probabilities for large times,

$$\Gamma(E) = \lim_{t\to\infty} \dot{P}(t) \tag{60}$$

This is done by parameterizing the paths in the probabilities in eq. (50), and then taking the derivative with respect to time. The probabilities only depend on the state N_- via the electrostatic energy. We illustrate the computation with the process (R,f) and parameterize the paths $N_+(t) = N_+(0) - \Theta(t)$ and $n(t) = n(0) - \Theta(t)$ where $\Theta(t)$ is the Heavyside function. We get

$$P_{\mathrm{R,f}}(n,t) = \frac{\Delta^2}{4}\int_0^t \mathrm{d}t_1 \int_0^{t_1} \mathrm{d}t_2 \Bigg[\exp\left\{-W(t_2-t_1)\right\} \times \exp\left\{\frac{i}{\hbar}\left[\frac{E_\mathrm{c}}{2}(2n-2n_0-1) - e\left(\delta V_\mathrm{g} - \frac{V_\mathrm{sd}}{2}\right)\right](t_2-t_1)\right\}\Bigg], \tag{61}$$

where $W(t) = W_+(t) + W_-(t)$. From eq. (61) we have then for the tunneling rate

$$\Gamma(E) = \frac{\Delta^2}{4}\int_{-\infty}^{\infty} \mathrm{d}t\, \mathrm{e}^{-W(t)+iEt/\hbar} \tag{62}$$

$$= \frac{\Delta^2}{2}\int_0^{\infty} \mathrm{d}t\, \mathrm{e}^{-\mathrm{Re}W(t)} \cos\left[Et/\hbar - \mathrm{Im}W(t)\right]. \tag{63}$$

The characteristic energy E depends on the actual tunneling event. We have for forward and backward tunneling through the left or right barrier the following energies:

$$E_{\mathrm{L,f}}(n) = E_\mathrm{c}\left[-n+n_0-\frac{1}{2}\right] + e\left[-\frac{V_\mathrm{sd}}{2}+\delta V_\mathrm{g}\right] \tag{64}$$

$$E_{\mathrm{L,b}}(n) = E_\mathrm{c}\left[n-n_0-\frac{1}{2}\right] + e\left[\frac{V_\mathrm{sd}}{2}-\delta V_\mathrm{g}\right] = -E_{\mathrm{L,f}}(n-1) \tag{65}$$

$$E_{\mathrm{R,f}}(n) = E_\mathrm{c}\left[n-n_0-\frac{1}{2}\right] + e\left[-\frac{V_\mathrm{sd}}{2}-\delta V_\mathrm{g}\right] = -E_{\mathrm{R,b}}(n-1) \tag{66}$$

$$E_{\mathrm{R,b}}(n) = E_\mathrm{c}\left[-n+n_0-\frac{1}{2}\right] + e\left[\frac{V_\mathrm{sd}}{2}+\delta V_\mathrm{g}\right] \tag{67}$$

The tunneling rates also obey the detailed balance $\Gamma(-E) = \exp(-\beta E)\Gamma(E)$. We notice that the electronic integration and the temperature β influence the shape of the rates. It depends on the $W(t)$ or the spectral density $J(\omega)$, which arises from the kernel $K(\omega)$ in the effective action. We give the exact form of the rate for the TLL with a constant zero-range interaction below.

4.4 Coulomb blockade peak conductance

We want to determine the shape of the Coulomb blockade peaks that appear in the conductance when the chemical potential of quantum dot and the leads are aligned.

We have in the effective Euclidean action the potential terms from the local part of the kernel $K(\omega_n \to 0)$ which yields the charging energy and the parts from the external potentials,

$$\frac{E_c}{2}\left[n - n_0 - n_g\right]^2 + U_{imp}\cos\pi N_+ \cos\pi n - \frac{E_c}{2}\left[2n_0 n_g + n_g^2\right] - \frac{eV_{sd}}{2}N_+, \quad (68)$$

where $n_g = eV_g\delta/E_c$ is the number of induced electrons due to the coupling to the gate. It can be varied continuously through the gate voltage V_g, while n is changed only by integers as it stems from charge tunneling onto the dot. The first term $E_0^*(n)$ blocks fluctuations in the number of electrons on the dot n by the charging energy E_c, so that in general no electrons can tunnel onto and of the dot. However, by adjusting n_g through the gate voltage this Coulomb blockade can be waved. If $n_0 + n_g$ is tuned to be a half-integer the two charge states n and $n+1$ are degenerate and yield the same energy. In this situation the characteristic Coulomb blockade peaks in the linear conductance occur. The last term in (68) changes the electrochemical potentials of the leads with respect to the Fermi energy, $\mu_{L,R} = E_F \mp eV_{sd}/2$ where we let $\mu_F = 0$. The condition for two charge states to be degenerate corresponds to aligning the electrochemical potentials $\mu_L = \mu_{dot} = \mu_R$. From the groundstate energies we get the electrochemical potential of the dot as the difference between $E_0^*(n+1) - E_0^*(n)$,

$$\mu_{dot}(n+1) = E_c\left[n - n_0 - n_g + \frac{1}{2}\right]. \quad (69)$$

This dot potential is minimized at the half-integer values of $n_0 + n_g$, and since we are interested in the linear transport $V_{sd} \to 0$ only the two charge states n and $n+1$ can be involved in the transport through the dot. By tuning the n_g the chemical potentials of the dot and the leads are periodically aligned depending on the number of charges n. The distance between the Coulomb blockade peaks in the gate voltage is then $\Delta V_g = E_c\delta/e$. Having information on δ one can compare the microscopically obtained charging energy E_c to the experimentally measured period of the Coulomb blockade oscillations.

Since we assume uncorrelated sequential tunneling events we can set up a Master equation for the probability $P(n,t)$ of finding the charge state n at time t [67, 65]. $P(n,t)$ changes by tunneling in and from the leads which is described by the rates, and only the immediately precursing event is taken into account,

$$\begin{aligned}\dot{P}(n,t) = &-\left[\Gamma_{L,b}(n) + \Gamma_{R,f}(n) + \Gamma_{L,f}(n) + \Gamma_{R,b}(n)\right]P(n,t)\\ &+\left[\Gamma_{L,b}(n+1) + \Gamma_{R,f}(n+1)\right]P(n+1,t)\\ &+\left[\Gamma_{L,f}(n-1) + \Gamma_{R,b}(n-1)\right]P(n-1,t),\end{aligned} \quad (70)$$

where $\Gamma_{i,j}(n) \equiv \Gamma(E_{i,j}[n])$ with i =R,L and j =f,b from eqs. (64)-(67). The rates and probabilities determine the current

$$I = \frac{e}{2}\sum_n\left[\Gamma_{R,b}(n) + \Gamma_{L,b}(n) - \Gamma_{R,f}(n) - \Gamma_{L,f}(n)\right]P(n). \quad (71)$$

We want to calculate the stationary DC current in the linear transport regime where the potentials $\mu_{\mathrm{L,R}} = \mu_{\mathrm{dot}}$ are aligned. Only the two charge states n and $n+1$ are involved then, and the rates that carry away from those two states can be neglected. We can solve the Master eq. (70) in the stationary limit $\dot{P}(t) = 0$ and using $P(n+1) = 1 - P(n)$, which gives for the probability $P(n)$,

$$P(n) = \frac{\Gamma_{\mathrm{L,b}}(n+1) + \Gamma_{\mathrm{R,f}}(n+1)}{\Gamma_{\mathrm{L,f}}(n) + \Gamma_{\mathrm{R,b}}(n) + \Gamma_{\mathrm{L,b}}(n+1) + \Gamma_{\mathrm{R,f}}(n+1)}. \tag{72}$$

We plug this into the expression for the current and have,

$$I = -e\frac{\Gamma_{\mathrm{L,f}}(n)\Gamma_{\mathrm{R,f}}(n+1) - \Gamma_{\mathrm{R,b}}(n)\Gamma_{\mathrm{L,b}}(n+1)}{\Gamma_{\mathrm{L,f}}(n) + \Gamma_{\mathrm{R,b}}(n) + \Gamma_{\mathrm{L,b}}(n+1) + \Gamma_{\mathrm{R,f}}(n+1)}. \tag{73}$$

Using the detailed balance condition $\Gamma(-E) = \exp(-\beta E)\Gamma(E)$ and the symmetries of the energies,

$$\begin{aligned} E_{\mathrm{R,b}}(n) &= -\mu_{\mathrm{dot}}(n+1) + eV_{\mathrm{sd}}/2 = -E_{\mathrm{R,f}}(n+1) \\ \text{and} \quad E_{\mathrm{L,f}}(n) &= -\mu_{\mathrm{dot}}(n+1) - eV_{\mathrm{sd}}/2 = -E_{\mathrm{L,b}}(n+1), \end{aligned} \tag{74}$$

the differential conductance for the the Coulomb blockade peaks can be written as

$$\mathcal{G}_{\mathrm{d}}(\beta,\mu) = \left.\frac{\partial I}{\partial V_{\mathrm{sd}}}\right|_{V_{\mathrm{sd}}=0} = \frac{e^2\beta}{4}\frac{\mathrm{e}^{-\beta\mu/2}}{\cosh\frac{\beta\mu}{2}}\Gamma(\mu). \tag{75}$$

Here, μ depends on the gate voltage through n_{g} and is the distance from the resonance case where the potentials $\mu_{\mathrm{L}} = \mu_{\mathrm{dot}} = \mu_{\mathrm{R}}$ are aligned. $\Gamma(\beta,\mu)$ is the tunneling rate expression from eq. (63) which contains the interaction effects and additional temperature behaviour. Eq. (75) describes the line shape of Coulomb blockade peaks centered about $\mu = 0$ for a quantum dot formed by two high delta potentials in a Tomonaga-Luttinger-liquid quantum wire. The explicit form of the tunneling rate and hence also the CB lineshape depends on the assumed interaction potential in the model. We give analytic results for the standard TLL model with homogeneous, zero-range interaction below.

4.5 Results for zero-range homogeneous interaction strength

For the basic TLL with zero-range interaction of constant strength $H = H_0 + H_{\mathrm{dot}} + H_U$ [eqs. (19), (41) and (42)] the tunneling rate in in the expression for the conductance peak can be calculated analytically for low temperatures. This is because the spectral density can be separated into an ohmic part resembling a single barrier and a periodic dot part describing the excitation structure of the quantum dot.

We obtain for the kernel (46) in the effective action,

$$K_{\pm}(\omega_n) = \frac{\pi\omega_n}{g_0}\left[1 \pm \mathrm{e}^{|\omega_n|\frac{ag_0}{v_{\mathrm{F}}}}\right]^{-1}, \tag{76}$$

where we used the Green function for this model from appendix A,

$$G_{\omega_n}(x,x') = \frac{g_0}{2\omega_n} e^{-|\omega_n||x-x'|g_0/v_\mathrm{F}}, \tag{77}$$

and the expressions from appendix C.2, which become eq. (76) due to the translational invariance of the propagator. We can write the spectral density in terms of $J_\mathrm{b} = 2\omega/g_0$ from eqs. (34,37)[66, 124]

$$J_\mathrm{d}(\omega) = J_+(\omega) + J_-(\omega) = \frac{1}{2} J_\mathrm{b}(\omega, x_i) \left[1 + \varepsilon \sum_{n=1}^{\infty} \delta(\hbar\omega - n\varepsilon)\right] \tag{78}$$

$$= J_\Omega(\omega) + J_\varepsilon(\omega). \tag{79}$$

The energy $\varepsilon = \pi\hbar v_\mathrm{F}/a g_0 = 2 g_0 E_\mathrm{c}$ is the discrete level spacing of the plasmon states in the quantum dot. Because of the constant, homogeneous interaction strength the Green function and spectral density does not depend on the barrier positions explicitly. The ohmic part J_Ω describes the properties of the semi-infinite leads left and right of the quantum dot, and the J_ε describes the equidistant modes of the quantum island. This discrete spectrum can be interpreted as the excitations of a plasmon that is pinned by the two impurity potentials. The wavevectors are then quantized in units $q_n = \pi n/a$ and the level spacing is obtained from the dispersion $\omega(q) = v_\mathrm{F} q/g_0$ of the TLL in the region $[x_1; x_1 + a]$,

$$\varepsilon = \hbar[\omega(q_{n+1}) - \omega(q_n)] = \frac{\pi\hbar v_\mathrm{F}}{a g_0} = 2 g_0 E_\mathrm{c}. \tag{80}$$

The energies $\varepsilon < E_\mathrm{c}$ set the range of validity of our model. In the following we will examine the case of the *quantum Coulomb blockade* where

$$k_\mathrm{B} T \ll \varepsilon < E_\mathrm{c}. \tag{81}$$

The part $W_\Omega(t)$ and $\Gamma_\Omega(E) = \gamma_{(g_0 \to 2g_0)}(E)$ is readily obtained from the single impurity case [eqs. (33) and (38)]. Since the kernel $W_\varepsilon(t)$ is periodic in ε, we can Fourier expand $\exp\{-W_\varepsilon(t)\}$,

$$\mathrm{e}^{-W_\varepsilon(t)} = \sum_{p=0}^{\infty} w_p(\varepsilon) \mathrm{e}^{-ip\varepsilon t/\hbar}. \tag{82}$$

Now the forward tunneling rate is calculated [66]

$$\Gamma(E) = \sum_{p=0}^{\infty} w_p(\varepsilon) \gamma_{(g_0 \to 2g_0)}(E - p\varepsilon) \tag{83}$$

$$w_p(\varepsilon) = \left(1 - \mathrm{e}^{\varepsilon/\hbar\omega_\mathrm{c}}\right)^{1/g_0} \frac{\Gamma(1/g_0 + p)}{p!\Gamma(1/g_0)} \mathrm{e}^{-p\varepsilon/\hbar\omega_\mathrm{c}} \tag{84}$$

where $\Gamma(\,\cdot\,)$ is the gamma function and $\gamma(\,\cdot\,)$ the single barrier rate from eq. (36) with a doubled parameter g_0 as the argument. The calculation leading to $w_p(\varepsilon)$

is given in appendix E. If $k_B T \ll \varepsilon$ we only keep the $p = 0$ term in the Fourier expansion. This leads to the conductance of the CB peak in the quantum regime and zero-range homogeneous interaction,

$$\mathcal{G}_d(T,\mu) = \frac{1}{4R_\Delta} \frac{|\Gamma(1/2g_0 + i\mu/2\pi k_B T)|^2}{\cosh \mu/2k_B T} \left(\frac{\varepsilon}{\hbar\omega_c}\right)^{1/g_0} \left(\frac{2\pi k_B T}{\hbar\omega_c}\right)^{1/g_0 - 2} \frac{e^{-|\mu|/\hbar\omega_c}}{\Gamma(1/g_0)}. \tag{85}$$

where $R_\Delta = 2\hbar\omega_c^2/\pi e^2\Delta^2$ is defined as in the single barrier case but here describes the two tunnel junctions in series. We observe from eq. (85) that the maximum of the CB peak ($\mu = 0$) scales in temperature as,

$$\mathcal{G}_d^{\max}(T) \propto T^{1/g_0 - 2}. \tag{86}$$

This expression coincides in the noninteracting limit $g_0 = 1$ with the form given in eq. (3). However, in the presence of Coulomb interactions the TLL model predicts a deviation from the linear behaviour in T for the height of a CB peak. The conductance scales in a power-law fashion which is determined by the interaction strength g_0. Generally the conductance maximum of the Coulomb blockade peak scales in nontrivial power-law $\mathcal{G}_d^{\max} \propto T^{\nu_{\text{eff}}}$ with an effective exponent. This effective ν can itself depend on the temperature. We will examine the effects on the power-law behaviour of an additional spin degree of freedom, a long-range interaction and the influence of a nonhomogeneous interaction strength along the TLL in the next chapters.

Resonant tunneling through a double barrier in a TLL was first extensively studied in [109], and also the spin degree of freedom was considered. The temperature dependence of the Coulomb blockade peak in the spinless case and the peculiar power-law was examined in [125]. Also coherent charge transport [124] in the double barrier TLL and resonant tunneling through a quantum dot connected to semi-infinite TLL leads was addressed [126]. There the sequential tunneling rates were calculated by Fermi's golden rule. The nonequilibrium transport through a dot coupled to TLL leads was discussed in [127] where the tunneling process was assumed to be coherent. Spin blockade effects in the nonlinear transport regime were found [128].

In the following we will discuss how particular properties of the interaction influence the power laws measured in experiments.

4.6 Summary

A 1D quantum dot immersed in a quantum wire can be modeled by a double barrier structure in an TLL. Then an effective theory depending only on the relevant degrees of freedom describing the charge states in the dot and the imbalanced particles is obtained by use of imaginary time pathintegrals and mapping on the Caldeira-Leggett model for dissipative quantum systems. From the effective action the microscopic charging energy is derived immediately. Electronic transport

is described by a Master equation for the tunneling rates, and it can be solved analytically in the linear, CB regime. The conductance depends through the tunneling rate crucially on the spectral densities of the system, which contain information on the level spacing (plasmon quantization) of the dot and the continuous, Ohmic spectrum of the leads. The key quantity in these calculations is the time ordered Green function which determines the spectral density through the dissipative kernel in the effective action. Finally a closed form for the CB peak lineshape is given.

5 Effects due to the interaction landscape

In this section we discuss various extensions to the basic TLL model which is based on a zero range interaction and infinite system length.

5.1 Interaction of finite range

As a first extension to the basic TLL model (19) we investigate the effect of a long-range interaction potential: $V^{\mathrm{fr}}(x) = 2V_0/(\alpha d)^2 \exp(-\alpha|x|)$ where α is a phenomenological screening parameter which determines the range of the interaction with respect to a reference length d, e.g. the diameter of a quantum wire. The form can be obtained by assuming a three dimensional screened Coulomb interaction and projecting it onto the wire axis [103]. In this particular case the Fourier transform of the potential can be evaluated analytically and the bosonic dispersion relation of the plasmons (18) reads

$$\omega(k) = v_{\mathrm{F}}|k|/\sqrt{1+\frac{\hat{V}^{\mathrm{fr}}(k)}{\pi\hbar v_{\mathrm{F}}}}, \qquad \hat{V}(k) = \frac{4V_0}{d^2}\frac{1}{k^2+\alpha^2}. \tag{87}$$

The effect of the non-zero range nature of the interaction potential is reflected in the asymptotic limits of low and high frequency, as illustrated in figure 17. At low energies the slope of the dispersion is governed by the interaction parameter $g_0 = [1+4V_0/\pi\hbar v_{\mathrm{F}}(\alpha d)^2]^{-1/2}$ for $\hat{V}^{\mathrm{fr}}(k\to 0)$. At large energies the dispersion converges to the non-interacting case $\omega(k) = v_{\mathrm{F}}|k|$. These features of the interaction potential and dispersion hold for any long range interaction [102].

The Hamiltonian for this model is [eqs. (18) and (41)],

$$H = H_0' + H_{\mathrm{dot}} = \hbar\sum_k \omega(k) b_k^\dagger b_k + H_{\mathrm{dot}}, \tag{88}$$

The effective Euclidean action is calculated along the lines given in appendix C.2. We can write the kernel in the effective action (46) in terms of the the non-local conductivity $\sigma_{\omega_n}(k) = 2e^2\omega_n G_{\omega_n}(k)/h$ of a pure quantum quantum wire described by H_0', [129],

$$K_\pm(\omega_n) = \frac{e^2\omega_n}{2\hbar}\frac{1}{\sigma(x=0,\omega_n)\pm\sigma(x=a,\omega_n)}. \tag{89}$$

The two impurities are located at $x_1 = 0$ and $x_2 = a$ and the relatively simple form of the dispersion allows for the analytical calculation of the conductivity [103] using the Kubo formula as in equation (22),

$$\sigma(k,\omega_n) = v_{\mathrm{F}}\frac{e^2}{h}\frac{2\omega_n}{\omega^2(k)+\omega_n^2} \tag{90}$$

$$\Rightarrow \sigma(x,\omega) = \mathrm{Re}\;\sigma(0,\omega)\exp(ik_\omega|x|) + i\;\mathrm{Im}\;\sigma(0,\omega)\;\exp\left(-\frac{\alpha\omega}{v_{\mathrm{F}}k_\omega}|x|\right), \tag{91}$$

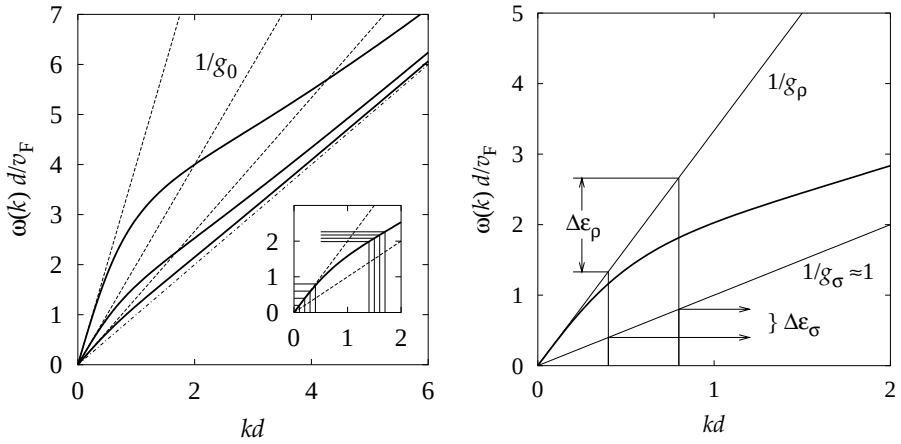

Figure 17: Dispersion relations for the long range interaction potential $V^{\rm fr}(x)$ where we chose αd=1. Left: dispersion for interaction parameters g_0 =0.25, 0.5 and 0.75 (full lines from top to bottom), the respective asymptotic curves (dashed lines) and the dispersion for the non-interacting case (dashed-dotted line). Inset: Plasmon dispersion for g_0=0.5 and asymptotics (dashed lines).The plasmon energies corresponding to equidistant wavenumbers $k_n d = n \times 0.1$ are indicated for low and high energies. Right: typical dispersions for charge and spin collective excitations and the two lowest but one energies due to the pinned plasmons (approximate level spacing of the quantum dot).

Here, k_ω is the inverse of the dispersion relation for positive and real k. The real and imaginary parts of $\sigma(0,\omega)$ can be determined and read [130],

$$\begin{matrix}\mathrm{Re}\\ \mathrm{Im}\end{matrix}\ \sigma(0,\omega) = \frac{e^2}{h}\frac{\omega}{v_{\rm F}\alpha}\left[\left(g_0^2 - \frac{\omega^2}{v_{\rm F}^2\alpha^2}\right)^2 - 4\frac{\omega^2}{v_{\rm F}^2\alpha^2}\right]^{-1/2}\frac{1-l^{\pm}}{\sqrt{|l^{\pm}|}}, \tag{92}$$

$$l^+ = -k_\omega^2/\alpha^2, \qquad l^- = \omega^2/v_{\rm F}^2 k_\omega^2.$$

We find that the microscopic charging energy $E_{\rm c} = \hbar K(\omega_n \to 0)/2$ is enhanced with respect to the zero range limit ($\alpha \to \infty$) given in eq. (58). We have for the long range potential $V^{\rm fr}$ [131]

$$E_{\rm c} = \alpha\frac{\pi}{2}\hbar v_{\rm F}\left[g_0 + \alpha a g_0^2 - g_0^3 + (g_0^3 - g_0)\mathrm{e}^{-\frac{\alpha a}{g_0}}\right]^{-1}. \tag{93}$$

We can now extract the spectral densities $J_\pm(\omega)$ from the kernel by analytic continuation. A clear separation into an ohmic part stemming from the leads and a part containing the level structure of the quantum dot is not possible here. This is due

to the long range nature of the interaction potential. We obtain

$$J_\pm(\omega) = \frac{e^2\omega}{2h\mathrm{Re}\ \sigma(0,\omega)}\Upsilon_\pm(k_\omega, g_0, \alpha a)$$

$$\Upsilon_\pm(k, g_0, \alpha a) = \frac{1 \pm \cos ka}{(1 \pm \cos ka)^2 + (\Xi_\pm(k, g_0, \alpha a) \pm \sin \alpha a)^2} \tag{94}$$

$$\Xi_\pm(k, g_0, \alpha a) = \frac{\mathrm{Im}\ \sigma(0,\omega)}{\mathrm{Re}\ \sigma(0,\omega)}\left(1 \pm \mathrm{e}^{-\frac{\alpha a \omega(k)}{v_\mathrm{F} k}}\right).$$

The complete spectral density $J(\omega) = J_+(\omega) + J_-(\omega)$ is plotted in Fig. 18 for three different α. It displays the following features due to the long range interaction:

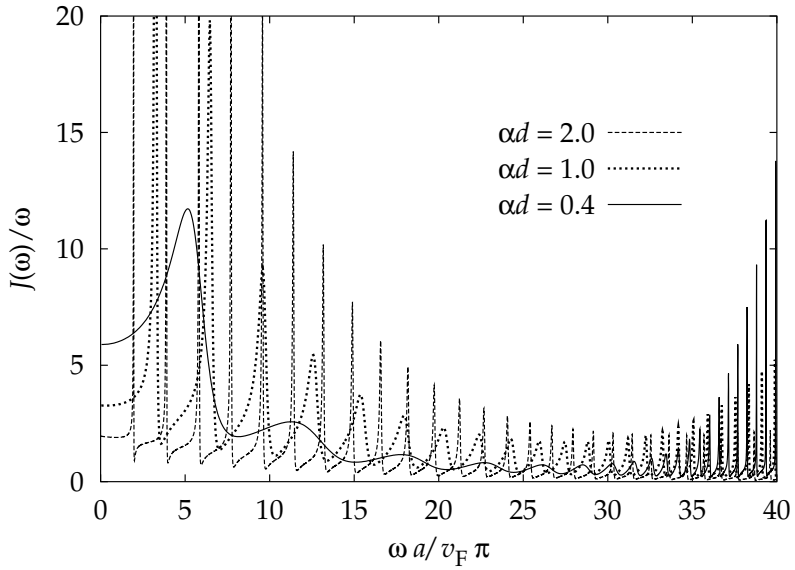

Figure 18: Spectral densities $J(\omega)/\omega$ for the interaction $V(x) = 2V_0/(\alpha d)^2 \exp(-\alpha|x|)$ as a function of normalized frequency $\omega a/v_\mathrm{F}\pi$ where $a/d = 10\pi$ and g_0=0.5. The interaction range is tuned by $\alpha d = 2,\ 1,\ 0.4$ (increasing range).

there are broadened, delta-function-like peaks which tend to become equidistantly spaced for large ω. The peaks become very narrow for large energies. This effect is enhanced when the range of the interaction is decreased. Actually the limit $\alpha \to \infty$ leads to non-interacting electrons as seen in the form of $V^\mathrm{fr}(x)$. Further, the peaks are strongly broadened when the interaction range is increased. Again, for a large ω, independent of the value of α, the peaks become narrow, almost delta-function-like peaks, and attain an equidistant spacing which we would expect for non-interacting electrons in one dimension which are confined to a region of length

a. This is illustrated in the inset of Fig. 17. We suggest the following interpretation: the interacting electrons are described by their collective excitations in terms of the plasmon fields. The barriers pin these plasmons and a situation similar to a standing wave occurs. The excitation energies of the system then approximately correspond to $\omega(q_m = m\pi/a)$. This explains why the maxima are shifted when the interaction range is increased. It is due to the non-linearity of the dispersion relation for the plasmons at "smaller energies" while the dispersion becomes linear again after a certain energy ω_p [103]. On the other hand, the effective Hamiltonian is equivalent to one for a quantum Brownian particle (corresponding to the coordinates $N^\pm$) in a dissipative environment and external potential. In this context the spectral density describes the possible "channels" for energy dissipation between the environment and the Brownian particle in a potential. One finds in the zero-range case that the peak positions correspond to (single) particle states in the dot. This analogy leads us to interpreting the peaks as states of the quantum dot which may contribute to transport through the dot. Because the interaction couples the dot with the leads, the "levels" of the quantum dot are broadened. The leads contribute mainly to the spectral density through a quasi Ohmic background. In the case of free electrons, the spectral density can be separated into a sum of delta function peaks describing the states of the dot and an Ohmic part ($\propto \omega$) corresponding to the leads [see eq. (79)]. This separation also works if one takes a zero-range interaction. Basically this tells us that a zero-range interaction creates an isolated quantum dot coupled to leads. Taking into account a long-range interaction, accounts for the correlation effects better, and the corresponding spectral density describes the overall spectral properties of the entire system including the left lead, the dot and the right lead. To sum up, first the interaction shifts the energy levels of the dot, and second the levels are broadened due to the coupling to the leads.

The nonzero range of the interaction is also manifest in the power-law exponents for the CB peak conductance. This can be seen from the low frequency limit of the spectral density,

$$J(\omega \to 0) = \frac{\omega}{2g_0}\left[1 + g_0^4\left(\frac{2aE_\mathrm{C}}{\pi\hbar v_\mathrm{F}}\right)^2\right], \tag{95}$$

This limit describes the dissipative influence of the low-frequency charge excitations in the external leads, $x < x_1$ and $x > x_2$. It holds also for finite frequencies. However, these must be smaller than the frequency scale corresponding to the range of the interaction, and smaller than the characteristic excitation energy of the correlated electrons in the dot. The limit in eq. (95) suggests that the long range interaction also alters the shape of the CB peaks. We have shown that the maximum $\mathcal{G}_\mathrm{d}^\mathrm{max}(\mathcal{T})$ of the conductance peaks of the Coulomb blockade oscillations exhibit a nonanalytic power-law due to the interaction in eq. (85). In the quantum CB the exponent is directly related to the limit in eq. (95). Defining

$$\frac{1}{g_\mathrm{eff}} := \frac{J(\omega \to 0)}{\omega}, \tag{96}$$

and recalling the expression for the CB peak conductance [eq. (75)] the results can be used for $J_b = 2\omega/g_{\rm eff}$. This yields for the temperature dependence of the peak maximum,

$$\mathcal{G}_d^{\max}(T) \propto T^{1/g_{\rm eff}-2}. \tag{97}$$

In contrast to a treatment with zero-range interaction, the exponent depends in a nontrivial way on the geometry of the system and the parameters of the interaction reflected by the charging energy $E_C(\alpha, a, g_0)$ in eq. (95). In the zero range case $g_{\rm eff}$ becomes simply equal to g_0 and the coupling of the dot seems to be disguised – only the properties of the leads are manifest in terms of g_0. Thus the finite range nature of the interaction should be manifest in the shape of the Coulomb peaks in experiments. We discuss a more realistic long range interaction which is appropriate for describing the situation in the CEO wires and also include the spin degree of freedom in the next section.

5.2 Spin and long–range interaction

We discuss two extensions to the standard TLL (spinless and zero-range interaction as described in chapter 3) here. First, we take into account the spin degree-of-freedom. Second, we assume a realistic long-range interaction to model the situation in the CEO quantum wires. We discuss our findings in context of the CEO experiment [74].

5.2.1 TLL with spin

When the electrons carry a spin the electron spectrum has two branches $s = \uparrow\downarrow$ for spin up and down particles, respectively. One can proceed the Bosonization as in the spinless case and write the fermion operator in terms of bosonic phase fields that are defined analogously to eqs. (10) and (11),

$$\psi_{\pm,s}(x) = \lim_{\lambda\to 0} \frac{U_{\pm,s}}{\sqrt{2\pi\lambda}}\, \mathrm{e}^{\pm ik_\mathrm{F}x \pm i\sqrt{\pi}\vartheta_s(x) - i\sqrt{\pi}\int^x \mathrm{d}y\, \Pi_s(y)}. \tag{98}$$

It is convenient to define linear combinations of ϑ_s and Π_s that describe the spin and charge density excitations,

$$\vartheta_\rho(x) = \frac{1}{\sqrt{2}}\left[\vartheta_\uparrow(x) + \vartheta_\downarrow(x)\right], \quad \Pi_\rho(x) = \frac{1}{\sqrt{2}}\left[\Pi_\uparrow(x) + \Pi_\downarrow(x)\right] \tag{99}$$

$$\vartheta_\sigma(x) = \frac{1}{\sqrt{2}}\left[\vartheta_\uparrow(x) - \vartheta_\downarrow(x)\right], \quad \Pi_\rho(x) = \frac{1}{\sqrt{2}}\left[\Pi_\uparrow(x) - \Pi_\downarrow(x)\right]. \tag{100}$$

The generalization of the particle density operator in terms of the phase fields is straightforward,

$$\rho(x) = \rho_0 + \frac{\sqrt{2}}{\sqrt{\pi}}\partial_x\vartheta_\rho(x) + \frac{2k_\mathrm{F}}{\pi}\cos[2k_\mathrm{F}x + \sqrt{2\pi}\vartheta_\rho(x)]\cos[\sqrt{2\pi}\vartheta_\sigma(x)]. \tag{101}$$

We have $\rho_0 = 2k_\mathrm{F}/\pi$ for the mean density while we assume a zero mean density for the spin. Then, the long wavelength part of the spin density fluctuations is obtained from ϑ_σ,

$$\rho_\sigma(x) \approx \sqrt{\frac{2}{\pi}}\,\partial_x\vartheta_\sigma(x). \tag{102}$$

The low energy physics of the 1D electron system is described by a TLL Hamiltonian where the spin and charge parts are completely separated, $H_\mathrm{lr} = H_\rho + H_\sigma$,

$$H_\mathrm{lr} = \frac{\hbar v_\mathrm{F}}{2}\int \mathrm{d}x\left[\Pi_\rho^2(x) + [\partial_x\vartheta_\rho(x)]^2\right] + \frac{1}{\pi}\int \mathrm{d}x\int \mathrm{d}y\,\partial_x\vartheta_\rho(x)V(x-y)\partial_y\vartheta_\rho(y) + \frac{\hbar v_\mathrm{F}}{2}\int \mathrm{d}x\left[\Pi_\sigma^2(x) + [\partial_x\vartheta_\sigma(x)]^2\right]. \tag{103}$$

Here, we do not take into account the exchange interaction between the spins which corresponds to $2k_\mathrm{F}$ momentum exchange, because it is generally very small compared to $\hat{V}(k)$ at small k [29, 132, 133]. Hence, the spin part H_σ describes collective

excitations of noninteracting Fermions in one dimension with an interaction parameter

$$g_\sigma = 1. \tag{104}$$

The spin density waves propagate with the Fermi velocity and have a linear dispersion $\omega_\sigma(k) = v_\mathrm{F}|k|$. On the other hand, the charge modes are subject to the Coulomb interaction through the potential $V(x-y)$. It has the Fourier transform $\hat{V}(k)$ and yields for the dispersion relation of the charge excitations,

$$\omega_\rho(k) = v_\mathrm{F}\,|k|\left[1 - \frac{2\hat{V}(k)}{\pi\hbar v_\mathrm{F}}\right]^{1/2} =: v_\rho(k)|k|. \tag{105}$$

The different renormalization of the propagation velocities for the spin and charge density excitations leads to the *spin charge separation* of the TLL. This is also illustrated in fig. 17.

The contribution of the two localized impurities is obtained along the lines of eqs. (24) and (41), and by use of the expression for the density (101),

$$H_\mathrm{dot} = \rho_0 \sum_{n=1,2} U_n \cos\left[2k_\mathrm{F}x_n + \sqrt{2\pi}\vartheta_\rho(x_n)\right]\cos\left[\sqrt{2\pi}\vartheta_\sigma(x_n)\right]. \tag{106}$$

As in the spinless case the forward scattering stemming from the first two terms in eq. (101) is omitted here. The smooth, slowly varying electric driving field couples to the the long-wave length part of the density (101). The corresponding Hamiltonian is,

$$H_U = -e\sqrt{\frac{2}{\pi}}\int \mathrm{d}x\, U(x,t)\partial_x\vartheta_\rho(x). \tag{107}$$

5.2.2 Long–range potential

As seen in fig. 3 the charges in the one-dimensional wire region in the CEO structure are relatively far away from the top gate which tunes the electron density. Generally, screening is always present in the semiconductor systems. We assume in the following in order to describe the screening in the CEO experiment [74] that it is solely due to an infinite metallic plane at a distance D in the y-direction parallel to the (x,z)-plane. The quantum wire is in the x-direction. Then, the effective electron-electron interaction energy can be calculated by using the method of image charges

$$V^{3d}(\vec{r}-\vec{r'}) = \frac{V_0}{|\vec{r}-\vec{r'}|} - \frac{V_0}{\sqrt{(x-x')^2+(z-z')^2+(y+y'-2D)^2}}, \tag{108}$$

with $V_0 = e^2/4\pi\epsilon_0\epsilon$ and the dielectric constant $\epsilon_0\epsilon$. For simplicity we model the wire of diameter $d \ll D$ with a parabolic confinement of the electrons perpendicular to the wire axis. This leads to the normalized Gaussian confinement wavefunction $\phi(s) = \sqrt{2}\mathrm{e}^{-s^2/d^2}/d\sqrt{\pi}$ where $s = \sqrt{y^2+z^2}$. The Fourier transform of

the effective interaction in the lowest subband can then be obtained from (108) by projecting with the $\phi(s)$,

$$\hat{V}(k) = \int \mathrm{d}s_1\, \mathrm{d}s_2\, \mathrm{d}x\, \phi^2(s_1)\phi^2(s_2) V^{3d}(x = x_1 - x_2, y_1 - y_2, z_1 - z_2)\, e^{ikx} \tag{109}$$

$$\begin{aligned} &= 2V_0 \int \mathrm{d}s_1\, \mathrm{d}s_2\, \phi^2(s_1)\phi^2(s_2)\, \mathrm{K}_0\left[k\sqrt{(z_1 - z_2)^2 + (y_1 - y_2)^2}\right] \\ &\quad - 2V_0 \int \mathrm{d}s_1\, \mathrm{d}s_2\, \phi^2(s_1)\phi^2(s_2)\, \mathrm{K}_0\left[k\sqrt{(z_1 - z_2)^2 + (y_1 + y_2 - 2D)^2}\right], \end{aligned} \tag{110}$$

where $\mathrm{K}_0(z)$ is the modified Bessel function [134] and we used [135]. The two integrals are best solved by changing variables $y_\pm = z_1 \pm y_2$ and $z_\pm = z_1 \pm z_2$. With [135, 136] we get for the effective interaction potential for $D \gg d$,

$$\hat{V}(k) = V_0 \left[\mathrm{e}^{d^2k^2/4}\, \mathrm{E}_1\left(\frac{d^2k^2}{4}\right) - 2\mathrm{K}_0(2Dk) \right], \tag{111}$$

where $\mathrm{E}_1(z)$ is the exponential integral. This expression shows explicitly how the gate screens the Coulomb interaction. In the limit $kd \to 0$, one obtains the finite value $\hat{V}(k \to 0) = 2V_0\,[\gamma/2 + \log(2D/d)]$ ($\gamma = 0.57722$ Euler constant). This implies a finite microscopic interaction parameter

$$g_\rho := \frac{v_\mathrm{F}}{v_\rho(q \to 0)} \left[1 + \eta\gamma + 2\eta \log\left(\frac{2D}{d}\right) \right]^{-1/2}, \tag{112}$$

where $\eta = 2V_0/\pi\hbar v_\mathrm{F}$. The 1D equivalent of the unscreened Coulomb interaction is obtained for $D \to \infty$. We now have the building blocks to investigate the transport through a one-dimensional quantum dot for electrons with a long-range interaction and with spin. Since the charge and spin modes are separated in the Hamiltonians the derivation of the effective action is straightforward.

5.2.3 Effective action

The two localized impurities separate the charge and spin degrees of freedom at the "bulk" positions $x \neq x_1, x_2$ from those at the barriers. As in the spinless case we introduce symmetric and antisymmetric variables for the particle ($\nu = \rho$) and spin densities ($\nu = \sigma$)

$$N_\nu^\pm = \sqrt{\frac{2}{\pi}} \left[\vartheta_\nu(x_2) \pm \vartheta_\nu(x_1) \right]. \tag{113}$$

The quantity N_ρ^- is associated with the fluctuations of the particle number with respect to the mean particle number $n_0 = \rho_0(x_2 - x_1)$. The corresponding excess charge is $-eN_\rho^-$. The variable N_σ^- represents the z-component of the fluctuation of the number of spins on the island which corresponds to a change of spin $N_\sigma^-/2$. The numbers of imbalanced particles and spins between left and right leads are

represented by N_ν^+. The DC current characteristic can then be evaluated by considering the stationary limit of the charge transfer through the dot in the presence of an external voltage as in eq. (43),

$$I = -\frac{e}{2} \lim_{t\to\infty} \langle \dot{N}_\rho^+(t) \rangle \,. \tag{114}$$

The Euclidean effective action is again obtained with the imaginary-time path integral method [137] and is analogue to the technique employed in chapter 4. Since the Hamiltonian does not mix the spin and charge modes the pathintegrations for the partial trace are performed independently. Then, the complete effective action is simply the sum of an effective action corresponding to the zero-range case given in chapter 4.5 with $g_0 = 1$ plus an effective action similar to the one in the foregoing chapter 5.1 for the special long-range interaction. Also the conditional probabilities that eventually describe the tunneling processes and rates [see eqs. (50)–(63)] have the same structure except that the spectral densities are composed by the sum of the corresponding $\pm$ and $\nu = \rho, \sigma$ parts (see below). We write S_{eff} which depends on the four variables defined in (113), in the compact form

$$\begin{aligned} S_{\text{eff}}[N_\rho^\pm, N_\sigma^\pm] \;\; &= \;\; \int_0^{\hbar\beta} \mathrm{d}\tau \; H_{\text{dot}}[N_\rho^\pm, N_\sigma^\pm] - \sum_{r=\pm} \int_0^{\hbar\beta} \mathrm{d}\tau \; N_\rho^r(\tau) \mathcal{L}^r(\tau) \\ &\quad + \sum_{r=\pm} \sum_{\nu=\rho,\sigma} \int_0^{\hbar\beta} \int_0^{\hbar\beta} \mathrm{d}\tau \mathrm{d}\tau' \; N_\nu^r(\tau) K_\nu^r(\tau - \tau') N_\nu^r(\tau') \,. \end{aligned} \tag{115}$$

The Fourier transforms, at Matsubara frequencies $\omega_n = 2\pi n/\hbar\beta$, of the kernels $K_\nu^\pm(\tau)$ and of the effective "forces" $\mathcal{L}^\pm(\tau)$ are determined by the dispersion relations of the collective modes (105),

$$\left[K_\nu^\pm(\omega_n)\right]^{-1} = \frac{8 v_\nu g_\nu}{\pi^2} \int_0^\infty \mathrm{d}q \frac{1 \pm \cos[q(x_1 - x_2)]}{\omega_n^2 + \omega_\nu^2(q)} \,,$$

$$\mathcal{L}^\pm(\omega_n) = \frac{4ev_\mathrm{F}}{\pi^2} K_\rho^\pm(\omega_n) \int_{-\infty}^\infty \mathrm{d}x \; E(x, \omega_n) \int_0^\infty \mathrm{d}q \; \frac{\cos[q(x - x_2)] \pm \cos[q(x - x_1)]}{\omega_n^2 + \omega_\rho^2(q)} \,. \tag{116}$$

Since we did not specify the shape of the electric field $E(x,t)$ here, we have the particular form of the effective force $\mathcal{L}$. Both, $K_\nu^\pm$ and $\mathcal{L}^\pm$ contain the collective bulk modes which introduce the interaction effects to be described below.

We get the *addition energies* from the local part of the kernels $K_\nu^\pm$. While $K_\nu^+(\omega_n \to 0) = 0$ [66, 137], we have $K_\nu^-(\omega_n \to 0) \neq 0$. This defines the costs in energy for changing the number of charges and/or spins on the dot and has the corresponding Euclidean action,

$$S_{\text{ch}}[N_\rho^-, N_\sigma^-] = \sum_{\nu=\rho,\sigma} \frac{E_\nu}{2} \int_0^{\hbar\beta} \mathrm{d}\tau \, (N_\nu^-)^2, \tag{117}$$

with the characteristic addition energies

$$E_\nu = 2\hbar K_\nu^-(\omega_n \to 0) \qquad (\nu = \rho, \sigma). \tag{118}$$

For $\nu = \rho$, this corresponds to the *charging energy* obtained in the spinless case, that is supplied/gained, in order to transfer/remove one charge to/from the dot with respect to the mean value n_0, $N_\rho^- = \pm 1$. for $\nu = \sigma$, the *spin addition energy* E_σ is needed/gained in order to change the spin by exactly $\pm 1/2$. The Coulomb interaction in the dispersion relation of the charge excitations, increases considerably the charging energy E_ρ, compared to the spin addition energy E_σ. We always have $E_\rho > E_\sigma$.

Since the structure of the effective action is the same as in the spinless case, depicted in chapter 4, we can evaluate the tunneling rates through the dot by mapping on a model of a quantum Brownian particle. The tunneling rates depend on the *spectral densities* $J_\nu^\pm(\omega)$ that depend on the frequency dependent parts of the kernels. They are obtained by analytic continuation

$$J_\nu^\pm(\omega) = \frac{2}{\pi} \mathrm{Im} K_\nu^\pm(\omega_n \to +\mathrm{i}\omega)\,. \tag{119}$$

Here, we cannot provide a complete analytic expression for our realistic long-range interaction potential as it is feasible for $V^{\mathrm{fr}}(x)$ in chapter 5.1. However, we can extract their limits for $\omega \to 0$,

$$J_\nu^\pm(\omega \to 0) = \frac{A_\nu^\pm(g_\nu)}{4g_\nu}\omega, \tag{120}$$

$$\text{where:} \quad A_\rho^- = g_\rho^4 \left[\frac{E_\rho}{E_0}\right]^2, \quad E_0 = \frac{\hbar \pi v_{\mathrm{F}}}{2a}, \quad \text{and} \quad A_\nu^\pm = 1 \quad \text{else.} \tag{121}$$

This is a generalized form of eq. (95) from chapter 5.1. The limit describes the influence of the low-frequency charge and spin excitations in the leads, $x < x_1$ and $x > x_2$. It holds also for finite frequencies but they have to be smaller than the frequency scale corresponding to the range of the interaction, and smaller than the characteristic excitation energy of the electrons in the dot. For the quantum Coulomb blockade $\hbar\omega \leq k_{\mathrm{B}}T \ll \varepsilon$ this is the case.

Effect on the external electric field

Let us discuss the influence of the interaction on the electric driving field. This is described by the *effective driving forces*. In general, $\mathcal{L}^\pm(\tau)$ depend in a quite complicated way on the dispersion of the collective modes and on the shape of the electric field. We focus on the DC limit where it is sufficient to evaluate the Fourier components for $\omega_n \to 0$. In this case, the quantity $\mathcal{L}^+(\tau)$, which acts on the total transmitted charge, depends only on the integral of the static electric field over the entire system which is the source-drain voltage $V_{\mathrm{sd}} \equiv \int_{-\infty}^{\infty} \mathrm{d}x\, E(x)$,

$$\mathcal{L}^+(\tau) = \frac{eV_{\mathrm{sd}}}{2}\,, \tag{122}$$

where we used the relation

$$\frac{e^2 v_{\mathrm{F}}}{\hbar \pi^2} \int_0^\infty \mathrm{d}q \, \frac{\omega_n (1 \pm \cos qx)}{\omega_n^2 + \omega_\rho^2(q)} = \sigma_0(0, \omega_n) \pm \sigma_0(x, \omega_n) \,. \tag{123}$$

Here, $\sigma_0(x, \omega_n)$ is the frequency dependent nonlocal conductivity of the Luttinger liquid per spin channel [see eq. (23)]. The DC limit is $\sigma_0(x, 0) = g_\rho e^2/h$.

On the other hand, $\mathcal{L}^-(\tau)$ acts on the excess charge on the island, it does *not* generate a current. It depends on the spatial shape of the electric field and can be written in terms of the total charge Q_E accumulated between the points x_1 and x_2 of a pure TLL quantum wire. In formal terms, the charge Q_E is linear response of the charge density ρ subject to the DC electric field $E(x)$,

$$\mathcal{L}^-(\tau) = \frac{E_\rho Q_E}{e} \,, \tag{124}$$

where the charge can be obtained by the Kubo formula and is given by

$$Q_E = 2 \int_{-\infty}^{\infty} \mathrm{d}y \, E(y) \lim_{\omega \to 0} \left[\frac{\sigma_0(x_1 - y, -\mathrm{i}\omega) - \sigma_0(x_2 - y, -\mathrm{i}\omega)}{\mathrm{i}\omega} \right] . \tag{125}$$

Equivalently, this can also be understood in terms of addition energies. By keeping explicitly the $x_1 - x_2$ dependence in eqs. (116) and (118) we write the effective force as,

$$\mathcal{L}^-(\tau) = \frac{e}{2} E_\rho(x_1 - x_2) \int_{-\infty}^{\infty} \mathrm{d}x \, E(x) \, \left[\frac{1}{E_\rho(x - x_1)} - \frac{1}{E_\rho(x - x_2)} \right] . \tag{126}$$

Let us assume $x_{1,2} = \mp a/2$. If the effective electric field has inversion symmetry, $\mathcal{L}^-$ vanishes. Without inversion symmetry, the electric field generates an effective charge on the island which will influence the transport through the coupling between N_ρ^+ and N_ρ^- also in the dot Hamiltonian H_{dot} as seen below. Physically, this externally induced charge can be interpreted as the continuous charge n_g which is generated by the voltage V_{g} applied to an external gate which electrostatically influences the charge on the island. Thus, the above eq. (124) is the term that represents the effect of the gate voltage in the phenomenological theory of the Coulomb blockade. If we assume the field configuration from eq. (55) where the coupling is with the $N_\rho^\pm$ we recover exactly this coupling to the quantum dot,

$$S_U = -\frac{e V_{\mathrm{sd}}}{2} N_\rho^+ - e \, \delta \, V_{\mathrm{g}} [N_\rho^- + n_0]. \tag{127}$$

5.2.4 Coulomb blockade peaks

Let us focus on the term in the effective action containing the quantum dot Hamiltonian and examine the conditions for current transport. We can write the Hamil-

tonian for the two impurities in eq. (106) in terms of the variables $N_\nu^\pm$

$$H_{\rm dot} = U_{\rm imp}\Big[\cos\frac{\pi N_\rho^+}{2}\cos\frac{\pi N_\sigma^+}{2}\cos\frac{\pi(n_0+N_\rho^-)}{2}\cos\frac{\pi N_\sigma^-}{2} + \sin\frac{\pi N_\rho^+}{2}\sin\frac{\pi N_\sigma^+}{2}\sin\frac{\pi(n_0+N_\rho^-)}{2}\sin\frac{\pi N_\sigma^-}{2}\Big], \qquad (128)$$

where $U_1 = U_2 = U_{\rm imp}/\rho_0$ and eq. (128) is generalization of (49). The dynamics are dominated by tunneling events connecting the minima of $H_{\rm dot}$ in the now four-dimensional $(N_\rho^+, N_\rho^-, N_\sigma^+, N_\sigma^-)$ space [138]. The transitions between the minima of this 4D "washboard" potential correspond to different physical processes of transferring electrons from one side to the other of the quantum dot. We assume that the temperature is higher than the tunneling rate through the single barrier, then the dominant processes are sequential tunneling events [126].Hence, the transfer of charge occurs via uncorrelated single-electron hops on and off of the dot, associated with corresponding changes in the total spin. In this regime, one has to consider minima which correspond to pairs of even or odd N_ρ^- and N_σ^-. The dominant transport processes are those which connect minima via transitions $N_\rho^- \to N_\rho^- \pm 1$ associated with changes of the spin $N_\sigma^- \to N_\sigma^- \pm 1$. This is analogous to the spinless transitions depicted in chapter 4. For each of these processes also the external charge and the spin change by $N_\nu^+ \to N_\nu^+ \pm 1$. These minima are not degenerate because of the charge and spin addition energies E_ρ and E_σ which force the system to select favourable charge and spin states in the island. These selections become essential at low temperatures, $k_{\rm B}T < E_\nu$, when current can only flow if the resonant conditions are fulfilled. This can be achieved in the experiments by tuning external parameters, as to the source-drain voltage or the gate voltage. In particular the induced, continuous charge $n_{\rm g}$ due to the gate voltage $V_{\rm g}$ can create degenerate charge states in the island.

In the linear regime, $U \to 0$ and $k_{\rm B}T \ll E_\nu$, commencing with the island occupied by n electrons, we expect that another electron can enter and leave only if the difference between the ground state energies of $n+1$ and n electrons is aligned with the chemical potential of the external leads which are semi-infinite TLL systems. The ground state of an even number of electrons in the 1D island has the total spin zero. On the other hand, the ground state of an odd number of electrons can be assumed to have the spin $N_\sigma^- = \pm 1$ [139, 140]. This implies the resonance condition

$$\mu_{\rm dot}(n+1, s_n \pm 1) = E_0^*(n+1, \pm s_{n+1}) - E_0^*(n, \pm s_n) = 0 \qquad (129)$$

where $E_0^*(n, \pm s_n) = E_\rho(n - n_0 - n_{\rm g})^2/2 + E_\sigma s_n^2/2$ are the ground state energies with n particles and total spins $s_n = 0$ (n even) or $s_n = 1/2$ (n odd), respectively. With the charge, spin and external gate terms, eqs. (117) and (124), these resonance condition becomes

$$E_\rho\left(n - n_0 - n_{\rm g} + \frac{1}{2}\right) + (-1)^n\frac{E_\sigma}{2} = 0. \qquad (130)$$

The variable $n_g = eV_g\delta/E_\rho$ represents the number of induced particles due to the coupling to a gate at which the voltage V_g is applied, with a proportionality factor δ which can be determined experimentally. The zero of energy is assumed to be given by the external chemical potential in Eq. (129). From the above expression one can see that the distance of the peaks of the linear conductance when changing the gate voltage are given by $\Delta V_g = (E_\rho + (-1)^n E_\sigma)/e\delta \approx E_\rho/e\delta$ since $E_\sigma \ll E_\rho$. Having independent information on δ one can extract the value of the charging energy E_ρ (in principle also for the spin addition energy E_σ) from the experimental data.

CB peak conductance

In order to evaluate the current as a function of temperature and/or source-drain voltage, one needs to consider the behavior of the spectral densities given in eq. (119). We resort to the assumptions in chapter 4 of sequential tunneling, and hence we need to evaluate the tunneling rate. The structure of the pathintegral for the additional spin degree and the actual paths in eqs. (61,63) because physically each tunneling electron described by $N_\rho^\pm$ carries the spin and determines also the evolution of $N_\sigma^\pm$. So, the sum of the spectral densities enter the rate integral.

$$J(\omega) = \sum_{r=\pm} \sum_{\nu=\rho,\sigma} J_\nu^r(\omega)\,. \tag{131}$$

For temperatures much lower than the excitation energy in the quantum dot, the low-frequency behavior of the spectral density is mainly determined by the charge and spin excitations in the leads which is the $J_\Omega(\omega)$ term in eq. (79). Thus, the power-law dependence of the CB conductance peaks is described by a spectral density

$$J_{\rm eff}(\omega) = \frac{\omega}{2}\left(1 + \frac{1 + A_\rho^-}{2g_\rho}\right)\,. \tag{132}$$

Eq. (132) generalizes the result for the spinless electrons and the special long-range interaction in the chapter before. We conclude that the presence of the spin and the long range interaction in the leads introduces an effective interaction strength which is given by the effective interaction parameter,

$$\frac{1}{g_{\rm eff}} = \frac{1}{4}\left(\frac{1 + A_\rho^-}{g_\rho} + 2\right)\,, \tag{133}$$

This effective interaction parameter determines the power-law exponents. The $J_{\rm eff}(\omega) = \omega/g_{\rm eff}$ yields for the CB peak conductance in the quantum CB regime from eq. (85),

$$\mathcal{G}_{\rm d}(T,\mu) \propto T^{1/g_{\rm eff}-2}. \tag{134}$$

Sometimes the "intrinsic width" $\Gamma_i(T)$ of the linear conductance Coulomb peak depends is discussed. This is the integrated conductance over the gate voltage for a

give peak. Because the width of the CB peaks is linear in temperature, the intrinsic width is given in the standard spinless case by $\Gamma_i(T) \propto T^{1/g_\rho - 1}$. Correspondingly, with spin and long-range interaction, one finds

$$\Gamma_i(T) \propto T^{1/g_{\rm eff}-1}\,. \tag{135}$$

Coulomb staircase and spin and charge excitations in the dot

One can investigate the nonlinear current-voltage characteristic by increasing the source drain voltage $V_{\rm sd}$. In this case, the current-voltage characteristic shows the Coulomb staircase associated with transitions between successive ground states of the electrons in the quantum dot. In addition, fine structure appears which reflects the excitation spectra of the correlated electrons in the dot. They can be due to collective charge and spin modes ε_ν below(see b). The possible transitions are restricted by $-V_{\rm sd}/2 < \mu^*_{\rm dot}(n,s_n) < V_{\rm sd}/2$. The chemical potential $\mu^*_{\rm dot}(n,s_n)$ depends on the ground state chemical potential and the charge and spin excitations,

$$\mu^*_{\rm dot}(n,s_n) = \mu_{\rm dot}(n,s_n) + l\varepsilon_\rho + m\varepsilon_\sigma. \tag{136}$$

where $\mu_{\rm dot}(n,s_n)$ is the electrochemical potential of n electrons in the ground state in the quantum dot and m,l integers counting the number of charge and spin excitation quanta. For a completely isolated island, the corresponding energy spectra are discrete, $\omega_\rho(q_n)$ and $\omega_\sigma(q_n)$, due to the discretization of the wave number $q_n = \pi n/a$ associated with the confinement [eq. (80)]. Due to the coupling to the electrons in the leads via the interaction, these levels are broadened as seen in the previous chapter. In the following, we assume that this broadening is negligible. The screened Coulomb interaction causes a non-linear dispersion relation for the charge modes in the infinite TLL system as it is seen in fig. 17. This leads to non-equidistant charge excitation energies in the quantum dot,

$$\varepsilon_\rho(q_n) = \hbar\left[\omega_\rho(q_{n+1}) - \omega_\rho(q_n)\right]\,. \tag{137}$$

Their explicit values depend on the ratio between the distance a and the range of the interaction, D, through the Fourier transform $\hat{V}^{\rm lr}(q)$. For values of a much larger than this range, the first excited charge modes are equidistant (inset of fig. 17, left). They are given by the charge-sound velocity for $q \to 0$, $v_\rho = v_{\rm F}/g_\rho$,

$$\varepsilon_\rho = \frac{\hbar\pi v_\rho}{a} = \frac{\hbar\pi v_{\rm F}}{a g_\rho} =: \frac{2E_0}{g_\rho}\,, \tag{138}$$

where we introduced the reference energy E_0. In the opposite limit $a \ll D$, the nonlinear dispersion is affecting the first excitation. This results in a value smaller than eq. (138),

$$\varepsilon_\rho = \frac{\hbar\pi v_{\rm F}}{a}\left[1 - \gamma\eta + 2\eta\log\left(\frac{2a}{\pi d}\right)\right]^{\frac{1}{2}} =: \frac{2E_0}{f_\rho} < \frac{2E_0}{g_\rho}\,. \tag{139}$$

For the spin excitations, the dispersion in the infinite system is linear and the discrete spectrum is equidistant

$$\varepsilon_\sigma = \frac{\hbar \pi v_\mathrm{F}}{a} \equiv 2E_0. \tag{140}$$

Since $g_\rho \leq 1$ we note that the lowest excitation which appears in an energy window eV_sd in eq. (136) is a spin density excitation corresponding to $l = 0$ and $m = \pm 1$.

5.2.5 Microscopic charging energy

We analyze now in more detail the charging and spin addition energies of the one-dimensional quantum dot as a function of the parameters of our model for the long-range interaction. In addition to the interaction strength V_0, which contains as the essential quantity the dielectric constant ε, we have the Fermi energy E_F and three geometrical parameters: the distance D between the 1D system and the infinite metallic plane, the diameter d of the wire and the length a of the dot.

The spin addition energy can be easily evaluated from the simple, linear dispersion relation and the requisites from chapter 4.5,

$$E_\sigma = \frac{\pi \hbar}{2a}\,. \tag{141}$$

It is the same as the addition energy of non-interacting particles. This reflects the Pauli exclusion principle.

The charging energy E_ρ is evaluated numerically from eq. (118) as a function of a/d. It is shown in fig. 19 for different ratios D/d and different interaction strengths V_0/d with $d = 10\mathrm{nm}$ and $d = 20\mathrm{nm}$. Different V_0/d correspond to different ϵ. Changing E_F between 2 meV and 4 meV, values that cover the experimentally relevant region (CEO experiment from [74]), alters the curves in fig. 19 only less than 10%. For very small a/d, the charging energy diverges. We consider only the physically meaningful region $a/d > 1$ where the length of the dot is larger than the diameter of the wire system. We obtain the asymptotic values for the charging energy,

$$\frac{E_\rho}{E_0} \approx \left[1 + \eta\gamma + 2\eta \log\left(\frac{2D}{d}\right)\right] \equiv \frac{1}{g_\rho^2} \quad (D \ll a)\,, \tag{142}$$

$$\frac{E_\rho}{E_0} \approx \left[1 - \eta\gamma + 2\eta \log\left(\frac{2a}{\pi d}\right)\right] \equiv \frac{1}{f_\rho^2} \quad (D \gg a)\,. \tag{143}$$

E_ρ is only weakly influenced by D/d through the logarithm: changing D/d by a two orders of magnitude changes E_ρ only by about 30%.

The charging energy always increases with increasing interaction range D, because the cost of energy for putting additional electrons into the island increases. For interaction ranges much larger than a the charging energy saturates because only the short-range part of the repulsion between the electrons predominantly contributes. Therefore, E_ρ approaches the asymptotic value of eq. (143) (fig. 19,

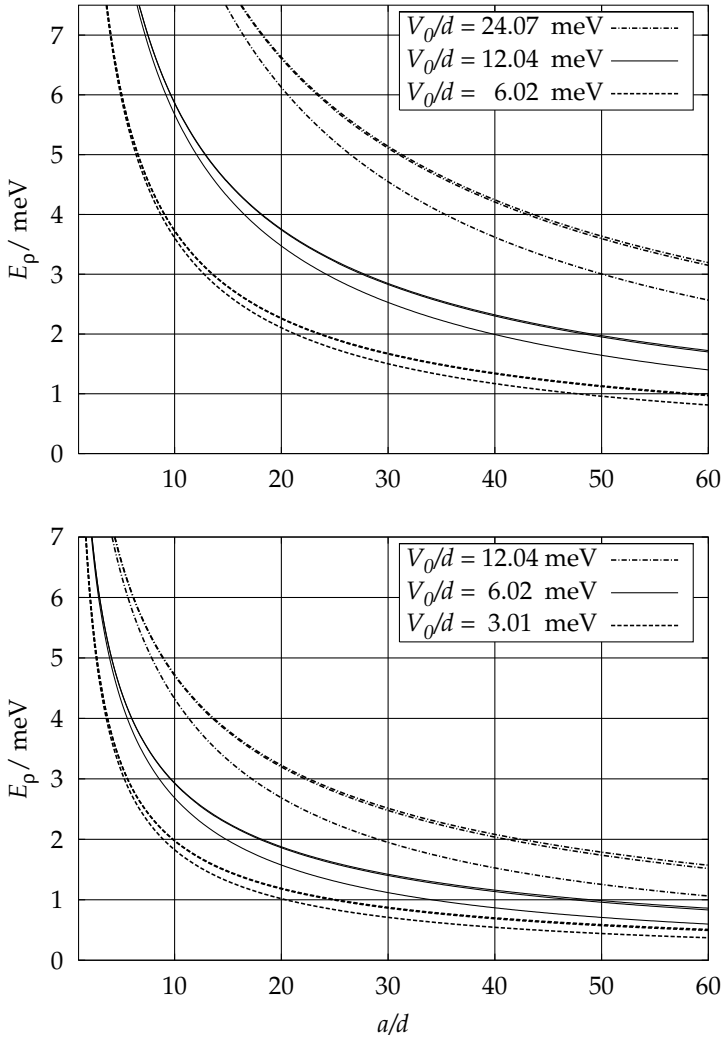

Figure 19: Charging energy E_ρ in meV as a function of a/d (Fermi energy $E_\mathrm{F} = 3$ meV, effective electron mass $m = 0.067m_0$). Top: $d = 10$nm; interaction strengths $V_0/d = 24.08$ meV (dashed-dotted), 12.04 meV (full lines,) 6.02 meV (dotted), corresponding to $\epsilon = 6$, 12, 24 (equivalent to $\eta = 2V_0/\pi\hbar v_\mathrm{F} = 2.04$, 1.02, 0.51, respectively), and $D/d = 1000$, 100, 10 (top to bottom). Bottom: $d = 20$nm; interaction strengths $V_0/d = 12.04$ meV (dashed-dotted), 6.02 meV (full lines,) 3.01 meV (dotted) and $D/d = 500$, 50, 5 (top to bottom).

curves for largest D/d). For a very strong Coulomb interaction ($\eta = 2V_0/\pi\hbar v_F \gg 1$) and $a \gg d$, the saturation value is

$$E_\rho = \frac{e^2}{2\pi\epsilon\epsilon_0 a}\log\left(\frac{2a}{d}\right) =: \frac{e^2}{C}\,. \tag{144}$$

Here, the C is the classical self-capacitance of a cylinder of the length a. The stronger the interaction (increasing V_0) the larger is E_ρ, very similar to the behaviour of a classical capacitor with a dielectric, $C \propto \varepsilon$.

As mentioned above, the non-linear transport shows Coulomb steps with widths given approximately by E_ρ, and fine structure due to the excited states. For a first estimate of the strength of the interaction is useful to estimate how many excited states are present in the energy window given the charging energy E_ρ. Figure 20 shows the ratios between the energy E_ρ and the first collective excited (spin or charge) state in the quantum dot ε_ν ($\nu = \sigma, \rho$). It is plotted as a function of the interaction constant g_ρ. The change in g_ρ could be obtained changing the distance D

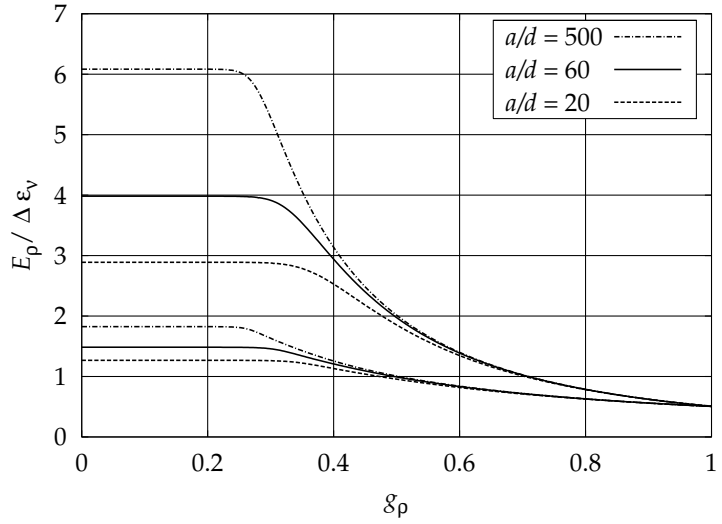

Figure 20: Ratios E_ρ/ε_ν ($\nu = \sigma, \rho$; upper/lower curves for fixed a/d) as a function of the interaction constant g_ρ for $a/d = 20$, 60, 500 with $\epsilon = 12$, $d = 20\,\mathrm{nm}$, $m = 0.067m_0$.

of the gate to the wire system, $g_\rho \to 0$ corresponds to $D \to \infty$ (an infinitely strong interaction). W notice that the ratio E_ρ/ε_ρ is always smaller than $E_\rho/\varepsilon_\sigma$. Therefore, we expect to observe in the energy window E_ρ much more levels due to spin excitations than due to charge excitations; E_ρ/ε_ν always increases when g_ρ decreases (increasing D). It saturates for $D \gg a$,

$$\frac{E_\rho}{\varepsilon_\rho} = \frac{1}{2f_\rho}\,; \qquad \frac{E_\rho}{\varepsilon_\sigma} = \frac{1}{2f_\rho^2}\,. \tag{145}$$

In the opposite limit, $D \ll a$, the behaviour is described by the asymptotic expressions

$$\frac{E_\rho}{\varepsilon_\rho} = \frac{1}{2g_\rho}\,; \qquad \frac{E_\rho}{\varepsilon_\sigma} = \frac{1}{2g_\rho^2}\,. \tag{146}$$

Discussion and comparison with the CEO experiment

We have different possibilities to confront our theoretical predictions regarding the role of the interaction in the one-dimensional system: the interaction parameter can be extracted from the distance between subsequent CB peaks in linear transport. Then, from the CB lineshape that is expected to obey a power-law depending on $g_{\rm eff}$. And finally, from the Coulomb staircase and the involved excited states of the quantum dot that may give rise to a fine structure.

Here, we compare our results with the experimental data obtained in the CEO experiment. In [74] the temperature dependence of the intrinsic width Γ_i of the conductance peaks in the quantum Coulomb blockade regime were investigated (see fig. 8, right). And the was consistently fitted with a power-law,

$$\Gamma_i(T) \propto T^{1/g^*-1}, \tag{147}$$

where $g^* \approx 0.82$ and $g^* \approx 0.74$ for the two peaks. The different exponents for the two peaks were explained by different electron densities in the quantum wires, since the top gate voltage is used to sweep through all the CB peaks and it simultaneously alters the density (fig. 3). In addition, information about the excited energy levels of the correlated electrons were obtained by measuring the nonlinear current voltage characteristics. Five excited levels were observed in the experiment [74]. The parameters from the experimental setup are: length of wire $L \approx 5\,\mu$m; length of the quantum dot $a = 100 - 200$ nm; (non-spherical) diameter of the quantum wire region $d = 10 - 25$ nm; distance to the gate $D \approx 0.5\ \mu$m. The charging energy, as estimated from the distance between the conductance peaks was determined as $E_{\rm C} \approx 2.2$ meV. Since the observed conductance peaks are equidistant within 10% we deduce that $E_\sigma \ll E_\rho$. A rough estimate of the Fermi energy is $E_{\rm F} \approx 3\,$meV. With these values one estimates an interaction parameter of $g_0 \approx 0.4$ without taking into account the spin degree [74], This is not consistent with the above g^* from the power-law fits.

Let us apply our microscopic approach. We estimate the length of the island a from the charging energy in fig. 19. As E_ρ is relatively insensitive with respect to changes of D/d and $E_{\rm F}$, we assume $D/d = 50$, $E_{\rm F} = 3$meV and $d = 20$nm. Furthermore, $V_0/d = 6.02\,$meV for $\epsilon = 12$. With the above 2.2 meV we find $a/d \approx 16$. Since we take into account the spin and use the interaction of finite range, the exponent g^* needs to be identified with the effective interaction $g_{\rm eff}$ in eq. (133). We find using $g^* = 0.82$ and 0.74 an interaction parameter $g_\rho^* = 0.6 \pm 20\%$ by solving eq. (133) for $E_\rho(g_\rho)/E_0$ and comparing with $E_\rho(g_\rho)/2E_0 = E_\rho/\varepsilon_\sigma$ in fig. 20. This would imply that $D \approx d$ [from eq. (112)]. On the other hand, by using eq. (112) with the above parameters, especially $D \approx 50d$, we find an interaction parameter $g_\rho \approx 0.25 \pm 20\%$ which depends only weakly on the ratio D/d. This is clearly not

a quantitatively consistent result. The discrepancy can be reduced by changing ϵ. However within reasonable values of all of the parameters, we have $g_\rho^* \approx 2g_\rho$.

Assuming $g_\rho^* = 0.6$, one gets from fig. 20 $E_\rho/\varepsilon_\rho \approx E_\rho/\varepsilon_\sigma \approx 1$. Thus, about 1 or 2 excited states corresponding to a given electron number should be observed in the nonlinear transport spectroscopy. This is also not found in the experiment. In order to observe a larger number of excited states, the interaction constant must be considerably smaller, $g_\rho < 0.3$, such that the number of spin excited states within the given window of E_ρ is increased (see fig. 20). Despite this inconsistency, the energetically lowest of the excited states seen in the nonlinear transport is predicted to be a spin excitation in terms of our approach.

Summary

In conclusion, we have derived the effective action for a quantum dot formed by a double barrier potential with a realistic long range interaction between the electrons, and including the electron spin. We have identified an effective driving force acting on the charge of the electrons, which turned out to be independent of the shape of the driving electric field. The mass terms are found for both the charge and the spin. They are identified with the charging energy in the case of the addition of charge and with a spin addition energy for the spin degree. Also, an effective force has been found which, in the DC limit, is only nonzero when the driving electric field and/or the barriers are asymmetric. This influences the transport via the coupling of modes at the potential barriers. It can be attributed to charging of the electron island via an external gate.

When we confront out microscopic predictions with the CEO experiment we find that it is not possible to consistently fit all of the experimental data with one, single interaction parameter. It seems that different interaction strengths have to be used for explaining the temperature dependence of the linear transport on the one hand, and the excitation spectrum of the quantum dot on the other. The interaction parameter $g_\rho^* \approx 0.6$, as estimated from the temperature behaviour, is larger than the one obtained from the observed number of the excited states of the dot, which yields $g_\rho < 0.3$. The temperature behaviour of the conductance peaks is dominated by the interaction among the electrons in the entire quantum wire which is situated along the edge of the whole CEO sample. However the excitation spectra probes the interaction strength only close to the quantum dot. Then the strength of the interaction far away from dot region can considerably influence the effective exponent in the power-law for the CB peak. The interaction is weaker in the region where the one-dimensional system is contacted to the 2DEG (fig. 3) due to screening. The influence of these contacts to the quantum wire on the effective power-law exponents is discussed in the next chapter.

5.3 Inhomogeneous interaction strength

As we have seen in chapter 5.2 a sufficient interpretation of the experimental results for the CB peak lineshape in the CEO geometry may require an interaction strength that changes along the quantum wire. Studies with non-monotonous interaction parameters [19, 17] already showed that the electronic transport can be dominated by the leads, where the interaction can be assumed absent and the interaction parameter is set to one, $g_0 = 1$. These approaches explained the non-renormalized conductance in clean wires [30]. On the other hand, it was also found that the power-law exponents g^* for the linear conductance of a single localized impurity in a TLL with zero-range interaction $\mathcal{G}_\mathrm{b} \propto T^{2/g^*-2}$ does not need to be universal for all temperatures when an interaction strength is assumed that is g_1 on a length L and $g_0 > g_1$ elsewhere [121]. Instead, asymptotically $g^* \to g_0$ for very small temperatures and $g^* \to g_1$ for very high temperatures was reported. We expect similar results for our model for the double barrier structure in a TLL quantum wire when the interaction strength is nonhomogeneous. However, we do not want to assume piecewise constant g's but a smooth variation in $g(x)$. We consider a zero-range interaction and do not take into account the spin degree in this chapter. The electron spin can give rise to interesting effects in the non-linear transport regime [128] but has a minor influence on the CB lineshape that we investigate here. Therefore we neglect the spin and concentrate on the charge sector which causes a nonuniversal power-law.

The experimental setup sketched in fig. 3 for the transport measurements on CEO quantum wires suggest that the interaction strength is not necessarily constant along the entire system. Due to gates to achieve the one channel, one-dimensional electron system the Coulomb interaction in the wire maybe screened differently at various positions in the quantum wire. The geometry of the CEO quantum wires suggests a stronger interaction in the center region of the wire system where relatively distant ($D \approx 0.5\mu$m) to the 1D system the top gate is situated to control the electron density. Meanwhile, left and right from the gate the 2D bands "merge" with the 1D electronic subbands. The extremely close 2DEG should lead to a much stronger screening of the Coulomb interaction than in the center. So, the interaction parameter $g(x)$ should change from a value g_0 at $\pm\infty$ to a minimum $g(0) = g_1$ in the center, where we set $x = 0$ below the center of the top gate. However this change should not occur abruptly but in smooth manner.

To model this situation we split the interaction into a constant part V_0 plus an additional potential which stems from the nonexistence of the 2DEG where the top gate is situated. Our interaction parameter is now spatially dependent and gives rise to a perturbation in the TLL Hamiltonian of eq. (16). We have,

$$\frac{1}{g(x)} = \left[1 + \frac{1}{\pi\hbar v_\mathrm{F}}\left[V_0 + V_1\varphi(x)\right]\right]^{\frac{1}{2}} \Leftrightarrow: \frac{1}{g^2(x)} = \frac{1}{g_0^2} + \frac{V_1\varphi(x)}{\pi\hbar v_\mathrm{F}}. \tag{148}$$

We may interpret g_0 as the "leads" interaction parameter and $g(x)$ as the actual local interaction strength in the quantum wire region. The strength of the inhomogeneity is characterized by V_1 and it particular shape by the "form function" $\varphi(x)$.

Possible form functions for the inhomogeneity potentials are

$$\varphi_1(x) = \mathrm{e}^{-\frac{4x^2}{L^2}} \qquad \varphi_2(x) = \frac{1}{1+\left(\frac{2x}{L}\right)^2}$$
$$\varphi_3(x) = \begin{cases} 1 & : \quad |x| < \frac{L}{2} \\ 0 & : \quad \text{else} \end{cases}$$

The length scale L a always refers to the extension or width of the inhomogeneity. Their respective shapes are given in fig. 21. More form functions are found in the appendix G. The inhomogeneity $\varphi_3(x)$ corresponds to the case which was consid-

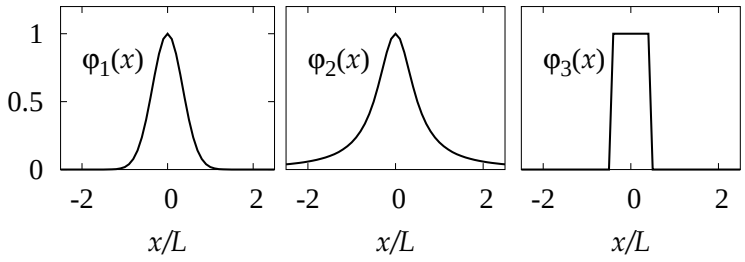

Figure 21: Inhomogeneity potentials $\varphi_i(x)$, $i = 1, 2, 3$.

ered in [19, 17, 121]. The φ's give rise to the "landscape" of the interaction strength $g(x)$ as it is illustrated in fig. 22. The presence of the inhomogeneity with extension L give also rise to an additional energy scale as we eventually will see explicitly

$$\omega_* = \frac{v_\mathrm{F}}{g_0 L}. \tag{149}$$

We write the resulting interaction parameter $g(x)$ as an expansion of the inhomogeneity strength V_1 for later reference,

$$g(x) = g_0 \left[1 - \frac{1}{2}\frac{g_0^2 V_1 \varphi(x)}{\pi\hbar v_\mathrm{F}} + \frac{3}{8}\left(\frac{g_0^2 V_1 \varphi(x)}{\pi\hbar v_\mathrm{F}}\right)^2 - \ldots\right] \approx g_0 \left[1 - \frac{c\varphi(x)}{\eta}\right], \tag{150}$$

which also implicitly defines the constant c here on the right-hand-side.

5.3.1 Green function for the inhomogeneous interaction

The Hamiltonian for a clean TLL (no spin) with zero-range, but spatially dependent interaction reads,

$$H = \frac{\hbar v_\mathrm{F}}{2}\int \mathrm{d}x \, \left[\Pi(x)^2 + \frac{1}{g^2(x)}[\partial_x \vartheta(x)]^2\right], \tag{151}$$

where $g(x)$ is defined in eq. (148) and Π and ϑ correspond to the same quantities as in eqs. (16) and (19).

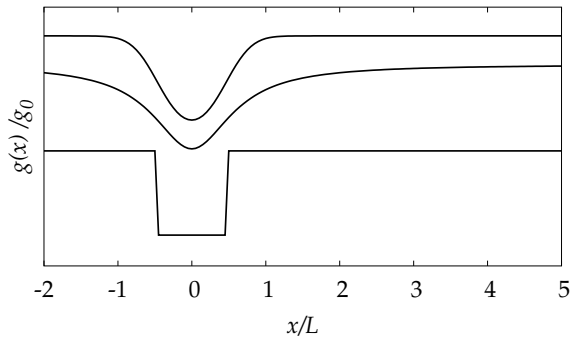

Figure 22: Interaction parameter $g(x)/g_0$ for the different inhomogeneity potentials $\varphi_i(x)$, $i = 1, 2, 3$ (from top to bottom). The curves are offset for each φ.

The transport properties are directly or indirectly related to the propagator or Green function $\langle T_\tau[\vartheta(x,\tau)\vartheta(x',\tau')]\rangle$ where $T_\tau[\dots]$ is the imaginary time ordering operator. Thus the effect of the inhomogeneous interaction strength will already be manifest in the Green function. We have the equation of motion for the propagator (see appendix A.2)

$$\left[\frac{\omega_n^2}{v_\mathrm{F}} - \frac{v_\mathrm{F}}{g_0^2}\partial_x^2 - \frac{V_1}{\pi\hbar}\partial_x\,\varphi(x)\partial_x\right] G_{\omega_n}(x,x') = \delta(x-x'). \tag{152}$$

We treat the term in V_1 as a perturbation and find for the Green function in first order in V_1,

$$\begin{aligned} G_{\omega_n}(x,x') &= G^0_{\omega_n}(x-x') + \frac{V_1}{\pi\hbar}\int \mathrm{d}y\; G^0_{\omega_n}(x-y)\left[\partial_y\varphi(y)\partial_y\right] G^0_{\omega_n}(y-x') \\ &\quad + \frac{V_1^2}{\pi^2\hbar^2}\int \mathrm{d}y \int \mathrm{d}z G^0_{\omega_n}(x-y)[\partial_y\varphi(y)\partial_y]G^0_{\omega_n}(y-z)[\partial_z\varphi(z)\partial_z]G^0_{\omega_n}(y-x') \\ &\quad + \frac{V_1^3}{\pi^3\hbar^3}\dots \\ &=: G^0_{\omega_n}(x-x') + \frac{V_1}{\pi\hbar}\delta G(x,x') + \frac{V_1^2}{\pi^2\hbar^2}\Delta G(x,x') + \dots. \end{aligned} \tag{153}$$

Here we first integrated by parts and used the property $\varphi(|x| \to \infty) = 0$. The unperturbed Green function $G^0_{\omega_n}(x-y)$ is calculated exactly and solves the homogeneous problem for $V_1 = 0$,

$$G^0_{\omega_n}(x-x') = \frac{g_0}{2|\omega_n|}\mathrm{e}^{-g_0|\omega_n(x-x')|/v_\mathrm{F}}. \tag{154}$$

In the following we consider only contributions up to first order in V_1. Defining $\eta = g_0|\omega_n|/v_\mathrm{F}$ and recalling that $c = g_0^3 V_1\omega_n/2\pi v_\mathrm{F}^2$, we can express the Green

function for a general inhomogeneity potential $\varphi(x)$ as,

$$G_{\omega_n}(x_1 < x_2) = \frac{g_0}{2|\omega_n|}\Big[\mathrm{e}^{-\eta(x_2-x_1)} - c\,\mathrm{e}^{-\eta(x_1+x_2)}\int_\infty^{x_1}\mathrm{d}y\,\varphi(y)\mathrm{e}^{2\eta y} - c\,\mathrm{e}^{\eta(x_1+x_2)}\int_{x_2}^{\infty}\mathrm{d}y\,\varphi(y)\mathrm{e}^{-2\eta y} + c\,\mathrm{e}^{-\eta(x_2-x_1)}\int_{x_1}^{x_2}\mathrm{d}y\,\varphi(y)\Big], \tag{155}$$

The case $x_1 > x_2$ is obtained by exchanging x_1 and x_2 in the expression, $G_{\omega_n}(x_1 > x_2) = (x_1 \leftrightarrow x_2)$. The one-point function at $x = x_\mathrm{d}$ has the compact form,

$$G_{\omega_n}(x_\mathrm{d}, x_\mathrm{d}) = \frac{g_0}{2|\omega_n|}\left[1 - c\,\mathrm{e}^{-2\eta x_\mathrm{d}}\int_\infty^{x_\mathrm{d}}\mathrm{d}y\,\varphi(y)\mathrm{e}^{2\eta y} - c\,\mathrm{e}^{2\eta x_\mathrm{d}}\int_{x_\mathrm{d}}^{\infty}\mathrm{d}y\,\varphi(y)\mathrm{e}^{-2\eta y}\right]. \tag{156}$$

Analytic results for $\varphi_1(x)$ and $\varphi_3(x)$

One convenient form to model the inhomogeneity is the Gaussian shape given by $\varphi_3(x)$. This choice allows for the analytic calculation of the Green function in terms of the error function $\Phi(x)$ [134],

$$G_{\omega_n}(x_1 < x_2) = \frac{g_0}{2\omega_n}\left\{\mathrm{e}^{-\eta(x_2-x_1)} - \frac{c}{\eta}\frac{\sqrt{\pi}}{4}\frac{\omega_n}{\omega_*}\Big[\mathrm{e}^{\eta(x_2-x_1)}\left(\Phi\left[2x_1/L\right] - \Phi\left[2x_2/L\right]\right) + \mathrm{e}^{\eta^2L^2/4-\eta(x+x')}\left(1 + \Phi\left[2x_1/L - \omega_n/2\omega_*\right]\right) + \mathrm{e}^{\eta^2L^2/4+\eta(x+x')}\left(1 - \Phi\left[2x_2/L + \omega_n/2\omega_*\right]\right)\Big]\right\}. \tag{157}$$

Setting $x = x' = x_\mathrm{d}$ we obtain the one-point function,

$$G_{\omega_n}(x_\mathrm{d}) = \frac{g_0}{2\omega_n}\Bigg[1 - \frac{\sqrt{\pi}}{4}\frac{c}{\eta}\frac{\omega_n}{\omega_*}\mathrm{e}^{\omega_n^2/4\omega_*^2}\Big\{\mathrm{e}^{-\omega_nR/\omega_*}\left(1 - \Phi\left[\omega_n/2\omega_* - R\right]\right) \tag{158}$$

$$+\mathrm{e}^{\omega_nR/\omega_*}\left(1 - \Phi\left[\omega_n/2\omega_* + R\right]\right)\Big\}\Bigg], \tag{159}$$

where we used

$$\omega_* = \frac{v_\mathrm{F}}{g_0L}, \quad R = \frac{2x_\mathrm{d}}{L}, \quad \text{and} \quad \Phi(x) = \frac{2}{\sqrt{\pi}}\int_0^x \mathrm{e}^{-t^2}\mathrm{d}t.$$

Clearly the extension of the inhomogeneity in the interaction strength gives rise to the energy scale ω_*. The quantity R measures the distance between the "impurity site" x_d and the maximum of interaction strength (minimum of $g(x)$).

The particular form of $\varphi_3(x)$ allows for an analytic evaluation of the Green function [17, 121] without resorting to perturbation theory. The computation for the entire $G_{\omega_n}(x, y)$ given in appendix F. In the region $-L/2 < x < L/2$ we have,

$$G^0_{\omega_n}(x_\mathrm{d}) = \frac{g_1}{2\omega_n} + \frac{g_1}{\omega_n}\frac{(g_0-g_1)^2\mathrm{e}^{-L\omega_ng_1/v_\mathrm{F}} + (g_0^2-g_1^2)\cosh(2x_\mathrm{d}g_1\omega_n/v_\mathrm{F})}{(g_0+g_1)^2\mathrm{e}^{\omega_nLg_1/v_\mathrm{F}} - (g_0-g_1)^2\mathrm{e}^{-\omega_nLg_1/v_\mathrm{F}}}. \tag{160}$$

Here, we have the constant $g_1 = [1 + (V_0 + V_1)/\pi\hbar v_F]^{-1/2} = g(x_d)$. This explicit form of G_{ω_n} was used to show that the linear DC conductance of a TLL quantum wire is determined only by the Fermi liquid leads where $g_0 = 1$.

Linear conductance of a TLL with inhomogeneous interaction strength

Let us examine the effect on the conductance of a quantum wire with the inhomogeneous interaction strength. We can use the Kubo formula to calculate the nonlocal conductivity of the TLL quantum wire as in chapter 3.3. The DC conductance is obtained in the limit $\omega_n \to 0$,

$$\lim_{\omega_n \to 0} \sigma_{\omega_n}(x, x') = \lim_{\omega_n \to 0} \frac{2e^2}{h} \omega_n G_{\omega_n}(x, x'). \tag{161}$$

From our expression for the Green function in eq. (153) we immediately see that the result is independent of the inhomogeneity. We obtain for the DC conductance,

$$\mathcal{G} = e^2 g_0 / h. \tag{162}$$

Thus the conductance of a pure quantum wire is always driven by the "leads" interaction parameter $g_0 = g(x \to \pm\infty)$ and does not depend on the interaction strength landscape. As in experiments the quantum wires are often connected 2 or 3 dimensional Fermi liquid leads where the interaction can be neglected, $g_0 = 1$. So, the measured conductance should be quantized by e^2/h in these cases.

5.3.2 Effective action

We employ the model introduced in chapter 4 to derive the effective action for a one-dimensional quantum dot in a TLL. The particularities due to the inhomogeneous interaction strength are reflected exclusively in the Green function above which appears in the kernels. We have,

$$S_{\text{eff}}[N_+, N_-] = S_1[N_+, N_-] + S_U[N_+, N_-] + S_{\text{dot}}[N_+, N_-],$$

where we use the same notation as in the eqs. (46), (49) and (55),

$$\begin{aligned} S_1[N_+, N_-] &= \frac{1}{2\beta} \sum_{n,r=\pm} N_r(\omega_n) K_r(\omega_n) N_r(\omega_n) \\ S_U &= -\frac{eV_{\text{sd}}}{2} N_+ - e\,\delta\,V_g n, \\ S_{\text{dot}} &= U_{\text{imp}} \cos \pi N_+ \cos \pi n. \end{aligned}$$

The central quantity which determines the spectral density and eventually the lineshape of the CB peaks is the kernel $K(\omega_n)$ which is explicitly written in the appendix. We assume the length of the quantum dot $a = x_2 - x_1$ much smaller than the extension L of the inhomogeneity potential. We assign the dot the "position" x_d such that $x_{1,2} = x_d \mp a/2$. Then we can write $K_\pm(\omega)$ up to the order a/L as

$$K_\pm(\omega_n) = \frac{\pi}{2} \frac{1}{G_{\omega_n}(x_d, x_d) \pm G_{\omega_n}(x_d - \frac{a}{2}, x_d + \frac{a}{2})}. \tag{163}$$

Charging energy

The charging energy is obtained from the limit $\omega_n \to 0$ of the $K_-(\omega_n)$. We have,

$$E_c = \frac{\hbar}{2} K_-(\omega_n \to 0) = \frac{\pi \hbar v_F}{2ag(x_d)^2}. \tag{164}$$

This result is remarkable because it reveals the *local* character of the charging energy. It depends explicitly on the interaction strength at the dot position through $g(x_d)$. This is physically feasible because only the electrons near the dot contribute to the charging and any interaction far away is irrelevant.

Spectral density

The spectral densities are obtained from the frequency parts of $K(\omega_n)$ by analytic continuation $J_\pm(\omega) = -\mathrm{Im}\, K_\pm(\omega_n - i\omega_n)/\pi$. For small a we can write the spectral densities (see appendix H) in the compact form

$$J_\pm(\omega) = \frac{1}{2}\mathrm{Im}\frac{1}{G_{\omega_n \to i\omega}(x_d, x_d)}\mathrm{Re}\left[1 \pm e^{i\omega \frac{ag(x_d)}{v_F}}\right]^{-1}. \tag{165}$$

In the actual transport equations and eventually the tunneling rates only the sum $J(\omega) = J_+(\omega) + J_-(\omega)$ appears. In analogy to the results for the zero-range case [eqs. (79)] we write the complete $J(\omega)$ in terms of the spectral density for a single impurity in a Luttinger liquid. $J_b(\omega, x_d)$. The latter corresponds to $J_b(\omega, x_d) = -\mathrm{Im}[G_{-i\omega}(x_d, x_d)]^{-1}$,

$$\begin{aligned} J(\omega) =& \frac{1}{2} J_b(\omega, x_d)\left[1 + \varepsilon \sum_n \delta(\hbar\omega - n\varepsilon)\right] \\ =& J^1(\omega) + J_\varepsilon(\omega), \end{aligned} \tag{166}$$

where the central quantity describing the dot contribution is,

$$\varepsilon = \frac{\pi \hbar v_F}{ag(x_b)} \tag{167}$$

It is the level spacing of the excited states of the one-dimensional quantum dot. The level spacing as well as the charging energy exclusively depends on the *local* interaction in the quantum dot region, i.e. on the length a and local interaction strength $g(x_d)$. This holds for arbitrary shapes of the inhomogeneity $\varphi(x)$.

The spectral density in our system can be separated into two parts: first, the semi–ohmic part $J^1(\omega)$ which describes the TLL leads directly left an right of the dot. In view of the mapping on a quantum dissipative system the dissipation is half as strong compared to the single impurity case with $J_b(\omega)$. This is reflected by the prefactor $1/2$ in line (166). This is because at the barrier positions $x_d \pm a/2$ the auto-dissipation is only driven by a half infinite TLL (to the left/right at $x \pm a/2$). For a homogeneous interaction strength the spectral density is Ohmic $J_b(\omega) \propto \omega$.

Second, the quantum dot structure $J_\varepsilon(\omega)$ which involves the discrete excitations with a spacing ε. The excitations result from the pinning of the collective (charge) excitations at the impurity sites $x = x_\mathrm{d} \pm a/2$.

Because eq. (166) retains the same structure as in the homogeneous zero-range case, the relevant quantity for the further computation of the tunneling rates is the semi-ohmic part. The shapes of $J^1(\omega)$ for the inhomogeneities $\varphi_i(x)$ with $x_\mathrm{d} = 0$ read

$$J_1^1(\omega) = \frac{\omega}{g_0}\mathrm{Re}\left[1 - \frac{\sqrt{\pi}}{2}\tilde{V}\frac{\omega_n}{\omega_*}\left[1 - \Phi\left(\omega_n/2\omega_*\right)\right]\mathrm{e}^{\left(\frac{\omega_n}{2\omega_*}\right)^2}\Big|_{\omega_n\to -i\omega}\right]^{-1}$$

$$J_2^1(\omega) = \frac{\omega}{g_0}\mathrm{Re}\left[1 - \tilde{V}\frac{\omega_n}{\omega_*}\left(\mathrm{ci}\frac{\omega_n}{\omega_*}\sin\frac{\omega_n}{\omega_*} - \mathrm{si}\frac{\omega_n}{\omega_*}\cos\frac{\omega_n}{\omega_*}\right)\Big|_{\omega_n\to -i\omega}\right]^{-1}$$

$$J_3^1(\omega) = \frac{\omega}{g_1}\mathrm{Re}\left[1 + 2\frac{(g_0-g_1)^2\exp\left(-\frac{\omega_n g_1}{\omega_* g_0}\right) + (g_0^2 - g_1^2)}{(g_0+g_1)^2\exp\left(\frac{\omega_n g_1}{\omega_* g_0}\right) - (g_0-g_1)^2\exp\left(-\frac{\omega_n g_1}{\omega_* g_0}\right)}\Big|_{\omega_n\to -i\omega}\right]^{-1}$$

$J_3(\omega)$ is the exact analytic result obtained from the exact form of the Green function eq. (160). The spectral densities are plotted in fig. 23.

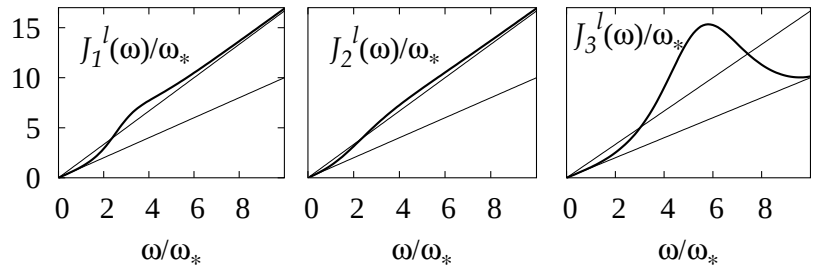

Figure 23: $J_i^1(\omega)$, $i = 1, 2, 3$.

The $J^1(\omega)$'s have the common features:

- for small frequencies $\omega \ll \omega_*$ the spectral density behaves like an Ohmic density corresponding to the leads $|x| \to \infty$, far away from the dot position, $J^1(\omega) = \omega/g_0$
- at high frequencies $\omega \gg \omega_*$ the spectral density attains an asymptotic slope that corresponds to am Ohmic density for a TLL with interaction parameter $g(x_\mathrm{b})$: $J^1(\omega) = \omega/g(x_\mathrm{b})$
- there is a crossover region about $\omega \approx \omega_*$ while the $J(\omega)$ behave smoothly in the other ω regions

The asymptotic slopes $\propto \omega/g_0$ and $\propto \omega/g_1 = \omega/g(x_\mathrm{d})$ respectively were used to infer the power-laws in temperature for the conductance of a single impurity in a

TLL and the $\varphi_3(x)$ inhomogeneity [121]. There, the Green function was calculated analytically for the box inhomogeneity. We provide the conductance for a single impurity in a TLL with a more general inhomogeneous interaction in appendix I.

5.3.3 Coulomb blockade peak lineshape

Since the formula for the spectral density [eq. (166)] is formally written as in the homogeneous, zero-range case (chapter 4.5) we can write the CB peak conductance in the quantum CB regime $\varepsilon \gg k_\mathrm{B}T$ as

$$\mathcal{G}_\mathrm{d}(\mu, T) = \frac{e^2\, \mathrm{e}^{-\mu/2k_\mathrm{B}T}}{4k_\mathrm{B}T\cosh(\mu/2k_\mathrm{B}T)}\, w_0(\varepsilon, T)\, \gamma(\mu, T), \tag{168}$$

which is equivalent to eq. (75) with (83). However, this result is only valid for $a \ll L$ as mentioned before. The gate energy μ denotes the distance from the CB peak maximum. Here, the weight $w_0(\varepsilon) = (\varepsilon/\hbar\omega_\mathrm{c})^{1/g(x_\mathrm{d})}$ stems from the Fourier expansion of the dot part of the spectral density in the rate integral. The rate $\gamma(\mu, T)$ carries the effect of the inhomogeneous interaction strength and a part of the temperature dependency. In contrast to the homogeneous case it has to evaluated numerically from

$$\gamma(\mu, T) = \frac{\Delta^2}{4}\int_{-\infty}^{\infty}\mathrm{d}t\, \exp\left\{ i\frac{\mu t}{\hbar} - \int_0^\infty \mathrm{d}\omega \frac{J^1(\omega)}{\omega^2}\left[\frac{1-\cos\omega t}{\tanh\frac{\hbar\omega}{2k_\mathrm{B}T}} + i\sin\omega t\right] \mathrm{e}^{-\omega/\omega_\mathrm{c}}\right\}. \tag{169}$$

We choose the very well behaving Lorentzian inhomogeneity $\varphi_2(x)$ for the following numerical analysis. The conductance for a Coulomb blockade peak as a function of temperature and gate energy is shown in fig. 24 for the asymptotic interaction parameters $g_0 = 0.6$ and $g(x_\mathrm{d}) = 0.3$. The units are given with respect to

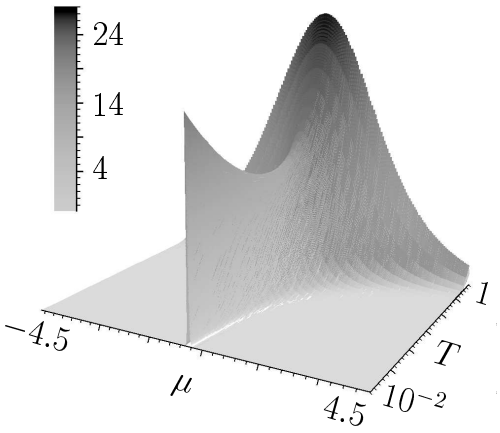

Figure 24: Conductance peak $\mathcal{G}_\mathrm{d}(\mu, T)$ of a 1D quantum dot for the Lorentzian inhomogeneity $\varphi_2(x)$ as a function of the gate energy μ and of the temperature T (units μ_*, T_*); parameters: $x_\mathrm{d} = 0$, $g_0 = 0.6$, $g_\mathrm{d} = 0.3$, $\omega^*/\omega_\mathrm{c} = 10^{-3}$, left: greyscale coding in units $10^{-4}G_0$, $G_0 = (\Delta/4\omega_\mathrm{c})^2(\varepsilon/\hbar\omega_\mathrm{c})^{1/g_\mathrm{d}}e^2/\hbar$).

the crossover energy $\hbar\omega_*$ and $T^* = \hbar\omega^*/k_\mathrm{B}$. It is immediately seen that the temperature behaviour is not universal over the entire range. First, at low temperatures

the peak height decreases with increasing temperature. Then, the slope changes and the height starts to increase when T is rised further. The effect on the expected power-law is better seen in a double-logarithmic plot for the maximum conductance (fig. 25). The maximum of the peak conductance has a minimum around

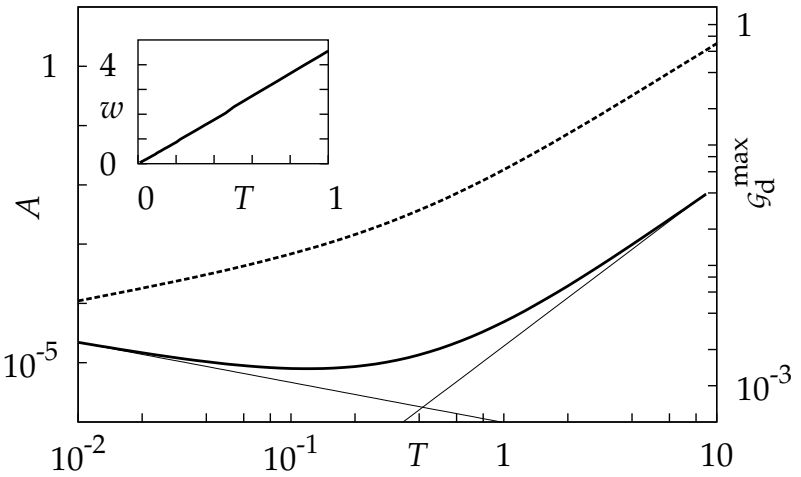

Figure 25: Double-logarithmic plot for the maximum conductance $\mathcal{G}_{\mathrm{d}}^{\max}$ in units $G_0 = (\Delta/4\omega_{\mathrm{c}})^2(\varepsilon/\hbar\omega_{\mathrm{c}})^{1/g_{\mathrm{d}}}e^2/\hbar$ (solid curve) and the peak area A normalized to $G_0\mu^*$ (dashed curve) as a function of temperature. T is measured in units of $T^* = \mu^*/k_{\mathrm{B}}$ ($\mu^* = \hbar\omega^*$); inset: peak width at half maximum W (units μ^*) as a function of T. (parameters are chosen as in fig. 24)

the crossover T_* that corresponds to the saddle in the 3D plot. If the temperature dependence of the maximum is written as $\mathcal{G}_{\mathrm{d}}^{\max}(T) \propto T^{1/g_{\mathrm{eff}}(T)-2}$ [see eq. (85)] we can define the effective interaction parameter $g_{\mathrm{eff}}(T)$. This changes between $g_{\mathrm{eff}}(T \ll T^*) = g_0$ and $g_{\mathrm{eff}}(T \gg T^*) = g(x_{\mathrm{d}})$. The particular minimum of $\mathcal{G}_{\mathrm{d}}^{\max}$ as a function of temperature is due to the peculiar choice of the asymptotic interaction parameters $g(x_{\mathrm{d}}) < 1/2 < g_0$. If both are larger or smaller than the critical value $1/2$ the conductance decreases or increases monotonously when the temperature is increased. However, independently of the details close to the crossover about T_*, the high- and low-temperature behaviour of the CB peak is always dominated by the local and global properties of the interaction represented by $g(x_{\mathrm{d}})$ and g_0. The inhomogeneity in the interaction strength does not disturb the proportionality to T of the width w of the peak which is shown in the inset of fig. 25. This implies that also in the inhomogeneous case the area A under the peak is connected to the peak height through $A \propto T\mathcal{G}_{\mathrm{d}}^{\max}$. This goes also under the name "intrinsic width" Γ_i of the CB peak as in the context of the CEO experiment [74]. From the experimental data the parameter $g^* \approx 0.82$ and 0.74 was extracted from a single power-law fit up to temperatures of 2K. However, from the charging energy and level spacing we expect $g_{\mathrm{d}} \approx 0.3$. This suggests that it was measured at temperatures lower than T_*.

This means that a measurement of the linear conductance of the 1D quantum dot at low temperatures reflects the interaction far away from the barrier, and therefore is a *global probe*. On the other hand, when measuring the Coulomb peak at higher temperatures, $T_* < T$, the interaction close to the dot will dominate. In this region, the experiment is a *local probe* for the interaction.

Summary

In conclusion, we assumed a nonhomogeneous interaction strength $g(x)$ in a quantum wire that contains a one-dimensional quantum dot. The interaction is characterized by the leads interaction parameter $g_0 = g(|x| \to \infty)$ and the local one with a minimum $g(x_\mathrm{d})$ where we assume the dot. We found that experimentally accessible quantities may be regarded as local or global probes. The microscopic charging energy, the level spacing of the dot and the temperature behaviour of the CB peak conductance at very high T are local probes. At small T (with respect to the characteristic energy of the inhomogeneity) however, the conductance peaks detect the global interaction landscape. This is reflected in the crossover in the power-law exponent for $\mathcal{G}_\mathrm{d}^{\max}(T) \propto T^{1/g_\mathrm{eff}(T)-2}$ which yields $g_\mathrm{eff} = g_0$ for $T \ll T_*$ and $[g(x_\mathrm{d})]$ for $T \gg T_*$. We confirm that the DC conductance of a clean TLL quantum wire is e^2/h per channel within our model if the wire is attached to Fermi liquid leads.

5.4 SET and tunnel contacts

In the preceding chapter we discussed the role of the leads that connect the quantum wire to the measuring apparatus in terms of a smooth change in the interaction strength. Here, we pursue a different approach. We assume a quantum wire with a constant, homogeneous (zero-range) interaction, but take into account that the electrons enter the TLL quantum wire by tunneling from a metallic contact. This is fairly the situation for the carbon nanotubes. They are difficult to connect to leads experimentally [56] and the connections between the nanotube and metallic contacts can be regarded as a tunnel junctions.

For armchair nanotubes two pairs of levels cross at the Fermi energy at two Fermi points as illustrated in fig. 5. The low energy of these metallic nanotubes can be described by considering the states near the Fermi energy only. In this regime the four one-dimensional crossing bands can be approximated by linear dispersion relations. Besides the usual quantum numbers for spin and momentum along the tube axis the number $j = r, l$ denotes right and left movers (branches with positive or negative slope), and $\alpha = \pm$ stands for the states around the Fermi points at $\pm k_{\mathrm{F}}$. The spectrum is analogous to that of fig. 12 of the TLL model as described in chapter 3. The electron operator takes a slightly more elaborate form than (7) due to the two transport band structure, and it is useful to introduce symmetric and antisymmetric combinations of the sublattices $\alpha = \pm$. The low energy properties are described by a four channel TLL where only one channel is affected by the interaction [141, 142],

$$H_{\mathrm{nt}} = \sum_p \frac{\hbar v_{\mathrm{F}}}{2} \int \mathrm{d}x \, \left[\Pi_p(x)^2 + \frac{1}{g_p^2} (\partial_x \vartheta_p(x))^2 \right]. \tag{170}$$

The channels are denoted $p = \rho+$, $p = \rho-$, $p = \sigma+$ and $p = \sigma+$ where we have charge (ρ) and spin σ and linear symmetric (+) and antisymmetric (–) combinations of the two Fermi points j. The phase fields are analogous to eqs. (10) and (11) and they obey the canonic commutation relations. If an ideal metallic nanotube which is –described by the Hamiltonian above– is perfectly contacted is expected to reveal a quantized conductance in units of $4e^2/h$.

Carrying out the bosonization procedure and computing the effective 1D interaction, The Coulomb interaction potential for electrons in the tube can be written as [143],

$$V_{\mathrm{nt}}(x - x') = \frac{e^2}{\epsilon_0 \epsilon} \frac{1}{\sqrt{(x - x')^2 + 4R^2 \sin^2[(y - y')/2R] + a_z^2}}, \tag{171}$$

where x runs along the tube axis, $0 < y \leq 2\pi R$ on the circumference, R is the radius, $\epsilon_0 \epsilon$ the dielectric constant and a_z is the average distance between a $2p_z$ electron and the nucleus. The interaction parameters are all $g_p = 1$ except for the $\rho+$ channel,

$$g_{\rho+} \equiv g_{\mathrm{nt}} = \left[1 + \frac{8e^2 \epsilon \epsilon_0}{\pi \hbar v_{\mathrm{F}}} \ln(L/2\pi R) \right]^{-1/2}. \tag{172}$$

Here, L is the length of the nanotube and an infrared cutoff at $k = 2\pi/L$ was used to treat the logarithmic singularity at $\hat{V}_{\rm nt}(k \to 0)$[143, 144]. For a typical $v_{\rm F} \approx 8 \times 10^5$ m/s, $L/R \approx 10^3$ and $\epsilon\epsilon_0 = 1...$ 2.4 ($\epsilon\epsilon_0$ =2.4 is the bulk graphite constant [145]) the interaction parameter has relatively small values $g_{\rm nt} = 0.17...0.3$. Hence, the interaction effects are very pronounced and manifest as the typical TLL power-law exponents. Since the nanotubes constitute a four channel TLL with only one interacting channel ($\rho+$) the power-law exponents are altered with respect to the standard one channel TLL model of chapter 3.4. We need to replace [146] $1/g_0 \to (3 + 1/g_{\rm nt})/4$ in eq. (39) when a single impurity is placed in a nanotube. Consequently, the power-law exponent for the conductance of a TLL-FL contact [eq. (40)] for the nanotubes reads,

$$\alpha_{\rm end} = \frac{1}{4}\left(\frac{1}{g_{\rm nt}} - 1\right). \tag{173}$$

However, for tunneling into the bulk of a nanotube one finds the exponent [141],

$$\alpha_{\rm bulk} = \frac{1}{8}\left(\frac{1}{g_{\rm nt}} + g_{\rm nt} - 2\right), \tag{174}$$

In the room temperature SET experiment [76] the two-terminal conductance of a metallic nanotubes with two defects between the metallic leads was measured. Thus, the setup (fig. 9) consists of a quantum dot immersed in a TLL plus two point like tunnel contacts. At room temperature charging effects should be due to the tiny quantum dot created by the buckles and should not arise from charging of the entire nanotube. Electrons are injected into the tube through a point-like tunnel contact, travel through tube and quantum dot, and they are collected from the metallic lead again by tunneling from the nanotube through a point like contact. We assume that the three tunneling processes (two junctions and the quantum dot phenomenology) are completely independent, and can be treated separately as elements of the circuit. The contacts each contribute through end–tunneling into the nanotube with a conductance,

$$\mathcal{G}_{\rm c}(T) = \frac{1}{R_{\rm c}}\left(\frac{2\pi k_{\rm B}T}{\hbar\omega_{\rm c}}\right)^{\alpha_{\rm end}}, \tag{175}$$

where we denote $R_{\rm c}$ the resistance of the junction. This is the nanotube version of eq. (40). Likewise the maximum of the CB peak conductance is written as a modified eq. (86),

$$\mathcal{G}_{\rm d}^{\rm max}(T) = \frac{1}{R_{\rm d}}\left(\frac{2\pi k_{\rm B}T}{\hbar\omega_{\rm c}}\right)^{\alpha_{\rm end}-1}, \tag{176}$$

where we cast the prefactors in the tunnel resistance $R_{\rm d}$. Usually, the tunnel resistance for a buckle is much larger than for tunneling from the metallic leads [62], hence: $R_{\rm c} < R_{\rm d}$.

The total resistance of the circuit is obtained by adding the resistances of the contacts eq. (175) and the one of the quantum dot. We get the complete conductance

for the CB conductance peak through

$$\mathcal{G}(T,\mu) = \frac{\mathcal{G}_{\rm d}(T,\mu)\mathcal{G}_{\rm c}(T)}{2\mathcal{G}_{\rm d}(T,\mu) + \mathcal{G}_{\rm c}(T)}. \tag{177}$$

The energy μ is as usual the distance from the peak maximum, and $\mathcal{G}_{\rm d}(T,\mu)$ the peak conductance given in eq. (85) in the nanotube version and normalized with respect to $\mathcal{G}_{\rm d}^{\rm max}(T)$. The shape of the CB peaks still remain intact and the temperature dependence of the conductance of the CB peak maximum is given in fig. 26. We plot the two cases of an end and a bulk contacted nanotube with the double buckle dot. In both cases the peak height $\mathcal{G}^{\rm max}(T)$ shows a crossover between global (small T) and local (large T) power laws. For $R_{\rm c} = 0$ (no contact) only the power-law behaviour of the dot is obtained (upper curves in fig. 26). If $R_{\rm c} \neq 0$ the power-law corresponding to the quantum dot is still dominant for high temperatures. On the other hand for lower T the influence of the contacts predominates the power-law. This crossover behaviour is again due to the "inhomogeneous" interaction. At low T the Fermi liquid leads cause the the temperature behaviour through the power-law in $\mathcal{G}_c(T)$. The high-T characteristics however, are determined by the local TLL parameter at the quantum dot. The overall effect of the quantum dot is more pronounced in the configuration where the tube is bulk-contacted because of the the relatively small $\alpha_{\rm bulk} = 0.25$.

Discussion

The result suggests that the unexpected temperature behaviour of the CB peak in the room temperature SET [76] is due to the interplay of the leads which contact the nanotube and the actual quantum dot formed by the buckles. An increase in the peak height with increasing temperature was reported there (see fig. 10 in chapter 2.4) which is in contrast of a decrease expected from the quantum dot power-law of eq. (176). Because the buckles usually yield high resistances with respect to tunneling into the end of a nanotube from the metallic lead, the power-law due to the leads it is very likely to remain over the entire temperature range in the SET experiment. Such an assumption yields a consistent interpretation of the experimental finding.

In conclusion, we find –as in the CEO setup– that the contacts to the TLL system may influence the temperature behaviour of the CB conductance peaks of the intratube quantum dot. The experimentally accessible quantity, i.e. the total conductance, is a local probe for the interaction at the quantum dot only for high temperatures. At low T the contacts to the nanotube dominate the temperature behaviour of the conductance.

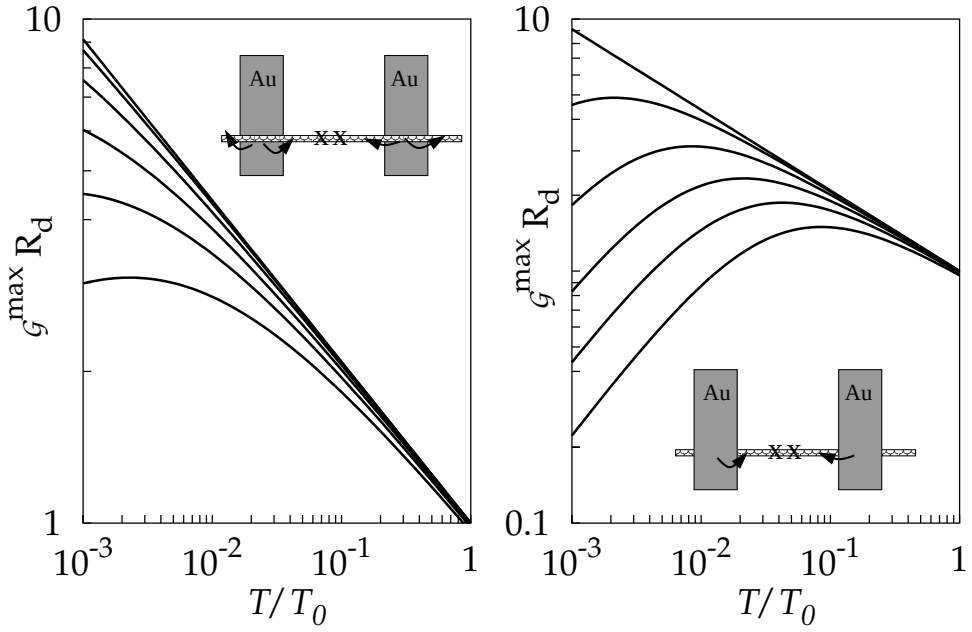

Figure 26: Left: "bulk-tunneling" from Au-contacts into a nanotube with two impurities (tube on top of contacts). Temperature dependence of a conductance peak for a one-dimensional quantum dot in a TLL connected to leads through resistive tunnel contacts with resistances R_d (dot) and R_c (contacts) in units R_d, α_{bulk} =0.25 (g_{nt} =0.27) and $T_0 = \hbar\omega_c/2\pi k_B$. The curves correspond to ratios R_c/R_d =0, 0.0005, 0.002, 0.005, 0.01, 0.02 (from top to bottom). Right: "end-tunneling" from Au lead into nanotube with quantum dot (contacts deposited on top of tube as in the room temperature SET setup). CB peak maximum for the same parameters as in left but the tunneling from the contacts into the nanotube is assumed to be into the end of the tube with the corresponding α_{end} =0.68. The low-temperature power-law stems from the resistive tunnel contacts while the high-temperature power-law is due to the quantum dot.

6 Conclusion

For one-dimensional interacting electrons a useful model is available that allows to treat the many-body system mostly analytically. We use this Tomonaga-Luttinger liquid model (TLL) to examine the interplay of interactions and impurities in quantum wires. In the special case where two high, localized impurities are close to each other in a quantum wire the island in between can be regarded as a one-dimensional quantum dot. Such a system is analyzed in view of the Coulomb blockade phenomenon in terms of the TLL and compared to experimental results.

In the past years experimental realizations of one-dimensional quantum dots were fabricated on semiconductor basis [74]. Also metallic nanotubes with deliberately created structural defects can operate as quantum dots immersed in a TLL [76]. Both geometries can be used to study the Coulomb blockade of the one-dimensional quantum dots.

The standard TLL model for single-channel quantum wires assumes a homogeneous zero-range interaction that is characterized by the single, constant parameter g_0. However, a consistent interpretation seems not feasible in terms of the standard TLL approach for sequential tunneling and Coulomb blockade. For the CEO quantum wire with a quantum dot the interaction parameters obtained from the charging energy and estimates from the level spacing in nonlinear transport did not match the interaction parameter extracted from the power-law behaviour in temperature of the Coulomb blockade peak conductance [147]. Also the unusual temperature behaviour of the conductance of an intra-nanotube one-dimensional quantum dot was not expected from the standard TLL: instead of a decreasing conductance with increasing temperature the conductance increased [76].

As a first approach we take into account the spin degree and assume a long-range interaction appropriate in the CEO case. We find that the theoretically expected interaction parameter is in better agreement with the experimentally extracted one. However, a quantitatively satisfactory interpretation is not reached. Earlier, theoretical and experimental studies of the quantized conductance of clean TLL quantum wires [30, 19, 17, 18] pointed to the importance of the leads that connect the measuring apparatus to the one-dimensional system. Therefore we set up an extended TLL model where the role of the contacts is modeled by a nonhomogeneous interaction strength described by $g(x)$. Here, the interaction is assumed to be weak in the leads $g(|x| \to \infty) = g_0$ and strong where the dot is $g_0 > g(x_{\mathrm{dot}})$ situated. This seems appropriate for the CEO experiment. Our approach shows that the power-law exponents are no longer universal due to the inhomogeneity. They rather depend on the temperature range where the Coulomb blockade is observed.

In the case of a intra-nanotube quantum dot, we model the connection to the metallic leads as point like tunnel junctions. We find again that the power-laws for the temperature dependence of the Coulomb blockade peak conductance is not universal, but there is a competition between power-law exponents due to the tunnel contacts and the power-law of the intra-tube quantum dot.

We conclude that for a consistent interpretation of the temperature dependence of the Coulomb blockade conductance peaks of one-dimensional quantum dots the

standard TLL is not sufficient. To explain this temperature behaviour observed in experiments we need to consider the role of the leads that contact the quantum wire with the external apparatus.

A Green functions

We write the Luttinger Liquid Hamiltonian in terms of the phase fields and assume zero range interaction which is characterized by the dimensionless interaction parameter $g(x)$ which we allow to be dependent on the position x.

$$H = \frac{\hbar v_{\mathrm{F}}}{2} \int \mathrm{d}x \, \left[\Pi(x)^2 + \frac{1}{g^2(x)} (\partial_x \vartheta(x))^2 \right]. \tag{178}$$

The phase fields ("plasmons") ϑ depend directly on the real Boson operators b_k

$$\vartheta(x) = i \sum_k \sqrt{\frac{v_F}{2L\omega_k}} \, \operatorname{sgn} k \, (\mathrm{e}^{-ikx} b_k^\dagger - \mathrm{e}^{ikx} b_k) \tag{179}$$

$$\Pi(x) = -\sum_k \sqrt{\frac{\omega_k}{2Lv_F}} \, \operatorname{sgn} k \, (\mathrm{e}^{-ikx} b_k^\dagger + \mathrm{e}^{ikx} b_k), \tag{180}$$

where ω_k corresponds to the plasmon dispersion and

$$H = \hbar \sum_k \omega(k) b_k^\dagger b_k, \qquad \omega(k) = v_{\mathrm{F}} |k| / \sqrt{1 + \frac{V(k)}{\pi \hbar v_{\mathrm{F}}}}. \tag{181}$$

$V(k)$ is the Fourier transform of the interaction potential. By a Legendre transform we obtain the corresponding action and write it in imaginary time,

$$S = \frac{1}{2} \int_0^{\hbar\beta} \mathrm{d}\tau \int \mathrm{d}x \left[\frac{\hbar}{v_{\mathrm{F}}} (\partial_\tau \vartheta(x,\tau))^2 + \frac{\hbar v_{\mathrm{F}}}{g(x)^2} (\partial_x \vartheta(x,\tau))^2 \right]. \tag{182}$$

The time ordered Green function for this theory is defined by

$$G(x,x';\tau,\tau') = \langle T_\tau [\vartheta(x,\tau)\vartheta(x',\tau')] \rangle, \tag{183}$$

where $\langle \cdot \rangle = \mathrm{Tr}\{\mathrm{e}^{-\beta H} \cdot\}$ denotes the thermal average with respect to the Hamiltonian in consideration, $\beta = 1/k_{\mathrm{B}}T$ is the inverse temperature, and T_τ denotes imaginary time ordering which can be written alternatively as

$$G(x,x';\tau,\tau') = \Theta(\tau-\tau') \langle \vartheta(x,\tau)\vartheta(x',\tau') \rangle + \Theta(\tau'-\tau) \langle \vartheta(x',\tau')\vartheta(x,\tau) \rangle. \tag{184}$$

Here, $\Theta(\tau)$ is the Heavyside function.

A.1 Canonical approach

The thermal averages for the bosons are the well known distributions

$$\langle b_k^\dagger b_k \rangle \equiv N_k = \frac{1}{\mathrm{e}^{\hbar\beta\omega_k} - 1} \quad \text{and} \quad \langle b_k b_k^\dagger \rangle = 1 + N_k. \tag{185}$$

Plugging (185) into (184) and using the basic bosonic commutation relations one arrives at

$$\begin{aligned} G(k,\tau) &= \Theta(\tau)\frac{v_{\mathrm{F}}}{2\omega_k}\left[(N_k+1)\mathrm{e}^{-\tau\omega_k}+N_k\mathrm{e}^{\tau\omega_k}\right] \\ &\quad +\Theta(-\tau)\frac{v_{\mathrm{F}}}{2\omega_k}\left[(N_k+1)\mathrm{e}^{\tau\omega_k}+N_k\mathrm{e}^{-\tau\omega_k}\right] \\ &= \frac{v_{\mathrm{F}}}{2\omega_k}\left(\mathrm{e}^{-|\tau|\omega_k}+2N_k\cosh\omega_k\tau\right). \end{aligned} \tag{186}$$

Next, we perform the usual Fourier transform $G_{\omega_n}(k) = \int_0^{\hbar\beta}\mathrm{d}\tau\exp(i\omega_n\tau)G(k,\tau)$ and use $\omega_n = 2\pi n/\beta$, where n is an integer number. Re-inserting N_k we arrive at the thermal, time ordered Green function,

$$G_{\omega_n}(k) = \frac{v_{\mathrm{F}}}{\omega_n^2+\omega(k)^2}. \tag{187}$$

A.2 Equation of motion

The time ordered Green function of a given theory, i.e. action, obeys a characteristic differential equation, its *equation of motion*. By stating the action and solving the differential equation, often peturbatively, one obtains the Green function. The equation of motion is derived within the functional integral formalism for the field theory. We integrate the Luttinger liquid action (182) by parts and use $\vartheta(\tau+\beta,x)\equiv\vartheta(\tau,x)\equiv\vartheta(\tau,x+L)$

$$S[\vartheta(x,\tau)] = -\frac{\hbar}{2}\int_0^L\int_0^{\hbar\beta}\mathrm{d}x\,\mathrm{d}\tau\left[\frac{1}{v_{\mathrm{F}}}\partial_\tau^2\vartheta(x,\tau)+\partial_x\left[\frac{v_{\mathrm{F}}}{g(x)}\partial_x\vartheta(x,\tau)\right]\right]\vartheta(x,\tau). \tag{188}$$

We define the operator

$$G^{-1}(x,\tau) := \left[\frac{1}{v_{\mathrm{F}}}\partial_\tau^2+\partial_x\frac{v_{\mathrm{F}}}{g(x)^2}\partial_x\right], \tag{189}$$

and insert it into the action

$$S[\vartheta(x,\tau)] = -\frac{\hbar}{2}\int_0^L\int_0^{\hbar\beta}\mathrm{d}x\,\mathrm{d}\tau\,\vartheta(x,\tau)G^{-1}(x,\tau)\vartheta(x,\tau). \tag{190}$$

We define the functional generator

$$\begin{aligned} Z[s(x,\tau)] &:= \frac{1}{Z_0}\int\mathcal{D}\vartheta(x,\tau)\mathrm{e}^{-S[\vartheta(x,\tau)]/\hbar}\mathrm{e}^{\int\int s(x,\tau)\phi(x,\tau)dxd\tau}, \\ &\text{where}\quad Z_0 = \int\mathcal{D}\,\vartheta\mathrm{e}^{-S[\vartheta]/\hbar} \end{aligned} \tag{191}$$

and have the functional derivative

$$\left.\frac{\delta F[f(x)]}{\delta f(x)}\right|_{x=x'} = \lim_{\epsilon\to0}\frac{1}{\epsilon}\left(F[f(x)+\epsilon\delta(x-x')]-F[f(x)]\right)$$

The thermal average of any operator $A(x,\tau)$ in terms of the functional integrals reads (automatically τ–ordered)

$$\langle T_\tau A(\vartheta(x_1,\tau_1),\vartheta(x_2,\tau_2)\dots)\rangle = \frac{1}{Z_0}\int \mathcal{D}\vartheta\; A(\vartheta(x_1,\tau_1),\vartheta(x_2,\tau_2)\dots)\mathrm{e}^{-S[\vartheta(x,\tau)]/\hbar}.$$

Let us calculate

$$Z_0\frac{\delta}{\delta\vartheta(x',\tau')}Z[s(x,\tau)] = \int \mathcal{D}\vartheta\left[G^{-1}(x,\tau)\vartheta(x',\tau')/\hbar + s(x',\tau')\right]\times \\ \exp\left\{-S[\vartheta]/\hbar + \int\int \mathrm{d}x\,\mathrm{d}\tau\, s(x,\tau)\vartheta(x,\tau)\right\}$$

and differentiate further with respect to $s(x,\tau)$

$$\int \mathcal{D}\vartheta\left[\delta(x-x')\delta(\tau-\tau') + \vartheta(x,\tau)G^{-1}(x,\tau)\vartheta(x',\tau')/\hbar + s(x',\tau')\vartheta(x,\tau)\right]\times \\ \times\exp\left\{-S[\vartheta]/\hbar + \int\int \mathrm{d}x\,\mathrm{d}\tau s(x,\tau)\vartheta(x,\tau)\right\}$$

Because the average is taken with respect to $\vartheta(x,\tau)$ we have for the left-hand-side

$$\int \mathcal{D}\vartheta\,\mathrm{e}^{-S[\vartheta]/\hbar}\mathrm{e}^{\int\int s\vartheta\mathrm{d}x\,\mathrm{d}\tau} = Z_0\langle \mathrm{e}^{\int\int s\vartheta\mathrm{d}x\,\mathrm{d}\tau}\rangle \quad\Rightarrow\quad \frac{\delta}{\delta\vartheta}\langle \mathrm{e}^{\int\int g\vartheta\mathrm{d}x\,\mathrm{d}\tau}\rangle = 0.$$

Putting $s(x,\tau)\equiv 0$ at the end of our calculation we obtain

$$0 = \frac{1}{Z_0}\int \mathcal{D}\vartheta\left[\delta(x-x')\delta(\tau-\tau') + \vartheta(x,\tau)G^{-1}(x,\tau)\vartheta(x',\tau')/\hbar\right]\mathrm{e}^{-S[\vartheta(x,\tau)]/\hbar} \\ \Leftrightarrow G^{-1}(x,\tau)\int \mathcal{D}\vartheta\left[\vartheta(x,\tau)\vartheta(x',\tau')\right]\mathrm{e}^{-S[\vartheta(x,\tau)]/\hbar}/Z_0 = -\delta(x-x')\delta(\tau-\tau') \\ \Leftrightarrow G^{-1}(x,\tau)\langle T_\tau\left[\vartheta(x,\tau)\vartheta(x',\tau')\right]\rangle = -\delta(x-x')\delta(\tau-\tau').$$

Hence the equation of motion for the (imaginary) time ordered Green function reads

$$\left[\frac{1}{v_\mathrm{F}}\partial_\tau^2 + \partial_x\frac{v_\mathrm{F}}{g(x)^2}\partial_x\right]G(x,x';\tau,\tau') = -\delta(x-x')\delta(\tau-\tau'). \tag{192}$$

Since the operator $[\dots]$ is selfadjoint the Green function $G(x,x';t,t')$ has to be symmetric in x and t. Hence $G(x,x';t,t') = G(x',x;t',t)$.

B Quantum dissipative systems

Often open quantum systems can be modeled by a system–plus–reservoir approach. The techniques to described such systems are extensively reviewed and applied in [115]. In the Caldeira–Leggett [118] model the reservoir is built by a bath of N harmonic oscillators described by the coordinates $\mathbf{x}(t) = [x_1(t),\dots x_N(t)]$ and the

Hamiltonian $H_{\rm R}$. Those are coupled linearly to the actual quantum system $H_{\rm S}[q(t)]$ under investigation. The time evolution of the quantum system is determined by the density functional $\mathcal{W}(t)$ or its matrix representation. One can write the functional in real time in terms of pathintegrals with respect to the $q(t)$ and $\mathbf{x}(t)$ [148]. Since one is interested in the dynamics of the system of the $q(t)$ rather than the combined set of system plus reservoir, one traces out the degrees-of-freedom that characterize the harmonic bath $\mathbf{x}(t)$. This leads to the reduced density functional $\mathcal{W}_{\rm S}(t) = \int \mathcal{D}\mathbf{x}(t)\mathcal{W}(t)$ which describes the time evolution of the quantum system $H_{\rm S}$ under influence of the bath $H_{\rm R}$. The technical difficulties arise in calculating the reduced or effective density matrix. Under the presumption that the coupling between the system and the reservoir is absent at $t = 0$ but switched on abruptly at $t = 0^+$ one can choose an initial state $\mathcal{W}(0) = \mathcal{W}_{\rm S}(0)\mathcal{W}_{\rm R}(0)$ where $\mathcal{W}_{\rm S}(0)$ is the density functional of the isolated system and $\mathcal{W}_{\rm R}(0) = {\rm e}^{-\beta H_{\rm R}}/Z_{\rm R}$ the functional for the unperturbed bath. If the system is ergodic, the density functional does not depend on the initial conditions at large times. Then, for this Feynman–Vernon product initial state the trace over the bathmodes can be carried out and a closed formula for the reduced density functional is available [123]. We quote the result without resorting to the actual form of the $H_{\rm S}$, $H_{\rm R}$ and couplings. The effective density matrix for $q_{\rm f} = q(t)$ and $q_{\rm i} = q(0)$ is

$$\mathcal{W}[q_{\rm f}, q'_{\rm f}; t] = \int \mathcal{D}q\mathcal{D}q' A_0(q,t) A_0^*(q',t) \mathcal{W}(q_i, q'_i; 0) \mathcal{F}_{\rm FV}[q(t), q'(t')]$$

$$A_0(q,t) = {\rm e}^{-iS_{\rm S}[q(t)]/\hbar}, \quad \mathcal{F}_{\rm FV}[q(t), q'(t')] = {\rm e}^{\Phi_{\rm FV}[q,q']},$$

$$\Phi_{\rm FV}[q,q'] = \frac{1}{\hbar}\int_0^t {\rm d}t_2 \int_0^t {\rm d}t_1 \left[\dot{q}_{\rm i}(t_2) - \dot{q}'_{\rm i}(t_2)\right] \left[W(t_2 - t_1)\dot{q}_{\rm i}(t_1) - W^*(t_2 - t_1)\dot{q}'_{\rm i}(t_1)\right],$$

$$W(t) = \int_0^\infty {\rm d}\omega \frac{J(\omega)}{\omega^2} \left[\frac{1 - \cos\omega t}{\tanh \beta\hbar\omega/2} + i \sin\omega t\right].$$

The kernel $W(t)$ contains all the information due to the dissipation through the *spectral density* $J(\omega)$. The spectral density can be obtained in the *imaginary time pathintegal* formalism for the reduced density matrix [115]. One can show that there is a connection between the effective Euclidean action $S^{\rm E}_{\rm eff}[q(\tau)] \equiv S^{\rm E}_{\rm S}[q(\tau)] + S^{\rm E}_{\rm infl}[q(\tau)]$, which is obtained by integrating out the bath modes in imaginary time $\tau = it$, and the real-time formulae above. Then calculating the reduced equilibrium density matrix by a partial trace ${\rm tr}_{\rm R}$ over the reservoir variables is considerably eas-

ier than in the real time formalism, and one ends up with a form

$$\mathcal{W}_\beta^{\mathrm{E}}(q'',q') = \mathrm{tr}_{\mathrm{R}}\, \mathrm{e}^{-\beta(H_{\mathrm{S}}[q(\tau)]+H_{\mathrm{R}}[x(\tau)]+H_{\mathrm{C}}[q(\tau),x(\tau)])}/Z \tag{193}$$

$$= \frac{1}{Z}\int_{q(0)=q'}^{q(\hbar\beta)=q''} \mathcal{D}q \oint \mathcal{D}x\, \mathrm{e}^{-S[q,x]/\hbar} \tag{194}$$

$$\equiv \frac{1}{Z}\int_{q(0)=q'}^{q(\hbar\beta)=q''} \mathcal{D}q\, \mathrm{e}^{-S_{\mathrm{S}}[q]/\hbar}\, \mathrm{e}^{-S_{\mathrm{infl}}^{\mathrm{E}}[q(\tau)]/\hbar}, \tag{195}$$

where the *influence functional* $\mathcal{F}^{\mathrm{E}}[q(\tau)] = \exp\{-S_{\mathrm{infl}}^{\mathrm{E}}[q(\tau)]/\hbar\}$ captures the influences of the bath (R) and coupling (C). The pathintegral with respect to $x(\cdot)$ runs over all periodic paths with period $\hbar\beta$. For a harmonic bath the influence action is written as a quadratic form

$$S_{\mathrm{infl}}^{\mathrm{E}}[q(\cdot)] = \int_0^{\hbar\beta} \mathrm{d}\tau \int_0^{\tau} \mathrm{d}\tau'\, q(\tau)k(\tau-\tau')q(\tau'), \tag{196}$$

and one can show that the spectral density in the dissipative kernel $W(t)$ is obtained from the Fourier representation of k at the Matsubara frequencies ω_n eq. (196) by analytic continuation [115],

$$J(\omega) = -\mathrm{Im}\frac{1}{\pi}k(\omega_n \to -i\omega). \tag{197}$$

Hence, by determining the effective action in imaginary time one gets the kernel $k(\tau)$ and from this the spectral density $J(\omega)$ by analytic continuation. $J(\omega)$ describes the spectrum of the modes through which energy can dissipate between the system and the bath/reservoir. The density functional in real time is then obtained in terms of the dissipative kernel $W(t)$ and one can investigate the dynamics of the system under influence of the coupling to the reservoirs.

C Effective actions

One can map the model for a δ-impurity in a quantum wire consisting of the TLL Hamiltonian H_{TLL} , the barrier H_{i} and the driving potential H_U [eqs. (16), (24) and (27)] on the system-plus-reservoir model above. The individual impurity mode(s) $\theta_{\mathrm{i}} = \vartheta(x_{\mathrm{i}})$ play(s) the role of the system variables $q(t)$ and the other bulk modes $\vartheta(x \neq x_{\mathrm{i}})$ are regarded as the bath (corresponding to $\mathbf{x}$ above). Since the current through a quantum wire with impurities is sufficiently determined by the evolution of the impurity modes one seeks an effective theory for θ_{i}. The difficulty is that one cannot immediately distinguish between the impurity and bulk modes in the Hamiltonian. One rather has to integrate out the superfluous degrees-of-freedom and then identify the effective and influence actions.

C.1 Single barrier effective action

We perform the partial trace with respect to $\vartheta(x,\tau)$ in terms of imaginary-time pathintegrals. To avoid that the pathintegration $\int \mathcal{D}\vartheta$ also traces out $\vartheta(x_\mathrm{i})$ the impurity mode is fixed by a delta functional [149] analogue to the Dirac-delta function

$$\delta[F_i(x,\tau)] \equiv \int \mathcal{D}\lambda_i(\tau) \mathrm{e}^{-i\int_0^{\hbar\beta} \mathrm{d}\tau F_i(x,\tau)\lambda(\tau)}. \tag{198}$$

The inclusion of $\delta[\vartheta(x_\mathrm{i}) - \theta_\mathrm{i}]$ in the pathintegral prevents θ_i from being traced out in the partition sum,

$$\mathrm{e}^{-S^\mathrm{E}_\mathrm{eff}[\theta_\mathrm{i}]/\hbar} = \int \mathcal{D}\vartheta\, \delta[\vartheta(x_\mathrm{i}) - \theta_\mathrm{i}] \mathrm{e}^{-S_\mathrm{TLL}[\vartheta]/\hbar - S_\mathrm{i}[\theta_\mathrm{i}]/\hbar - S_U[\theta_\mathrm{i}]/\hbar} \tag{199}$$

$$= \int \mathcal{D}\lambda\ \mathrm{e}^{i\int \mathrm{d}\tau\, \lambda(\tau)\theta_\mathrm{i}(\tau)} \int \mathcal{D}\vartheta\ \mathrm{e}^{-S_\mathrm{TLL}[\vartheta]/\hbar - i\int \mathrm{d}\tau\, \lambda(\tau)\vartheta(x_\mathrm{i},\tau)} \mathrm{e}^{-S_\mathrm{i}[\theta_\mathrm{i}]/\hbar - S_U[\theta_\mathrm{i}]/\hbar}. \tag{200}$$

The actions S_i and S_U correspond to the Hamiltonians in eqs. (24) and (27). S_TLL stems from the TLL model and is best written in terms of the inverse Green function as described in appendix A, $S_\mathrm{TLL}[\vartheta(\tau)] = -\frac{\hbar}{2}\iint \mathrm{d}x\, \mathrm{d}\tau\, \vartheta(x,\tau) G^{-1}(x,\tau)\vartheta(x,\tau)$ with the appropriate Green function of the model. First, the integration with respect to ϑ is done by completing the square in the second exponential in line (200) and then performing the Gaussian pathintegral. The result is absorbed into the normalization constant $\mathcal{N}$. What remains is

$$\mathrm{e}^{-S^\mathrm{E}_\mathrm{eff}[\theta_\mathrm{i}]/\hbar} = \mathcal{N} \int \mathcal{D}\lambda\ \mathrm{e}^{\frac{1}{2}\iint \mathrm{d}\tau\, \mathrm{d}\tau'\, \lambda(\tau) G(x_\mathrm{i},x_\mathrm{i};\tau,\tau')\lambda(\tau') + i\int \mathrm{d}\tau\, \lambda(\tau)\theta_\mathrm{i}(\tau)} \times \mathrm{e}^{-S_\mathrm{i}[\theta_\mathrm{i}]/\hbar - S_U[\theta_\mathrm{i}]/\hbar}.$$

Another completion of the square is needed, and it is convenient to express the fields and kernels in their Fourier representations $\theta_i(\tau) = \frac{1}{\hbar\beta}\sum_n \theta_\mathrm{i}(\omega_n)\mathrm{e}^{-i\omega_n\tau}$. Then the final (Euclidean) effective action reads

$$S^\mathrm{E}_\mathrm{eff}[\theta_\mathrm{i}] = \frac{1}{2\beta}\sum_n \frac{\theta_\mathrm{i}(\omega_n)\theta_\mathrm{i}(-\omega_n)}{G_{\omega_n}(x_\mathrm{i},x_\mathrm{i})} + \int_0^{\hbar\beta} \mathrm{d}\tau \left[U_\mathrm{i} \cos[2k_\mathrm{F}x_\mathrm{i} + 2\sqrt{\pi}\theta_\mathrm{i}(\tau)] + \frac{eU}{\sqrt{\pi}}\,\theta_\mathrm{i}(\tau)\right]. \tag{201}$$

C.2 Double barrier effective action

Since the current through a double barrier structure can be described by the evolution of the two phase fields $\vartheta(x_1)$ and $\vartheta(x_2)$ we seek an effective action for these impurity modes. As in the one impurity problem we inhibit the pathintegration at θ_i where $i = 1,2$ by introducing two delta-funcionals. The resulting imaginary-time pathintegrations are (superscript E omitted),

$$\mathrm{e}^{-S_\mathrm{eff}[\theta_1,\theta_2]/\hbar} = \int \mathcal{D}\lambda_1 \mathcal{D}\lambda_2\ \mathrm{e}^{i\int \mathrm{d}\tau\, \theta_1(\tau)\lambda_1(\tau)} \mathrm{e}^{i\int \mathrm{d}\tau\, \theta_2(\tau)\lambda_2(\tau)}$$
$$\times \int \mathcal{D}\vartheta\ \mathrm{e}^{-S_\mathrm{TLL}[\vartheta(\tau)]/\hbar - S_U[\vartheta(\tau)]/\hbar - i\int \mathrm{d}\tau\, \vartheta_1(\tau)\lambda_1(\tau) - i\int \mathrm{d}\tau\, \vartheta_2(\tau)\lambda_2(\tau) - S_\mathrm{dot}[\theta_1,\theta_2]/\hbar}. \tag{202}$$

The actions correspond to the one in the single barrier action except that two impurity potentials are introduced [eq. (41)] and that the electric potential which produces the field $\partial_x U(x) = E(x)$ is not further specified in eq. (42). The integrals are carried out as in the one impurity problem. First the ϑ integrations done by diagonalizing, then the λ_i- integrals are done successively. The resulting Gaussian integrals are cast into the normalization. We find for the effective action

$$\begin{aligned} S_{\text{eff}}[\theta_1,\theta_2] =& \frac{1}{2\beta}\sum_{n,i,k}\theta_i(\omega_n)G^{-1}_{ik}(\omega_n)\theta_k(-\omega_n) \\ &+ \frac{e^2\beta}{2\pi}\sum_n \int\int \mathrm{d}x\mathrm{d}x' E(x,\omega_n)E(x',-\omega_n)\times \\ &\qquad\qquad \times\left[\sum_{i,j} G(x,x_i;\omega_n)G^{-1}_{ik}(\omega_n)G(x',x_k;\omega_n)\right] \\ &+ \frac{e}{2\sqrt{\pi}}\sum_{n,i,k}\int \mathrm{d}x E(x,\omega_n)G(x,x_i;\omega_n)G^{-1}_{ik}(\omega_n)\theta_k(-\omega_n) \\ &+ S^{\text{dot}}[\theta_1,\theta_2]. \end{aligned} \tag{203}$$

We use the notation $G_{ij}(\omega_n) := G_{\omega_n}(x_i,x_j)$, and can write the inverse of the Green function Fourier modes as

$$\mathbf{G}^{-1} = \frac{1}{\det G}\begin{pmatrix} G_{22} & -G_{12} \\ -G_{21} & G_{11}\end{pmatrix}. \tag{204}$$

Using (anti) symmetric combinations of the impurity modes $\theta_\pm = \frac{1}{2}(\theta_1 \pm \theta_2)$ the general form of the effective action for a double barrier in a Tomonaga-Luttinger liquid and an arbitrary driving field $E(x)$ coupled to the charge density reads

$$S_{\text{eff}}[\theta_+,\theta_-] = \sum_{r=\pm}\left(S^r[\theta_r] + S^r_U[\theta_r]\right) + S^{r,-r}[\theta_+,\theta_-] + S^{\text{const}}_U + S_{\text{dot}}[\theta_+,\theta_-], \tag{205}$$

where the quadratic terms in $\theta_\pm$ are

$$S^\pm[\theta_\pm] = \frac{1}{2\beta}\sum_n \theta_\pm(\omega_n)\tilde{K}_\pm(\omega_n)\theta_\pm(\omega_n) \tag{206}$$

$$\tilde{K}_\pm(\omega_n) = \frac{G_{22}(\omega_n) \mp 2G_{12}(\omega_n) + G_{11}(\omega_n)}{G_{11}(\omega_n)G_{22}(\omega_n) - G_{12}(\omega_n)G_{21}(\omega_n)}. \tag{207}$$

The $\pm$ mixed terms

$$S^{r,-r}[\theta_+,\theta_-] = \frac{1}{2\beta}\sum_n \theta_+(\omega_n)\tilde{K}^{r,-r}(\omega_n)\theta_-(\omega_n) \tag{208}$$

$$\tilde{K}^{r,-r}(\omega_n) = \frac{G_{11}(\omega_n) - G_{22}(\omega_n) - r\left[G_{12}(\omega_n) - G_{21}(\omega_n)\right]}{G_{11}(\omega_n)G_{22}(\omega_n) - G_{12}(\omega_n)G_{21}(\omega_n)}, \tag{209}$$

and the linear terms with the electric fields read

$$S_U^{\pm} = \frac{e}{2\sqrt{\pi}} \sum_n \int \mathrm{d}x\, E(x,\omega_n) \tilde{L}^{\pm}(x,\omega_n) \theta_{\pm}(-\omega_n) \tag{210}$$

$$\begin{aligned} \tilde{L}^{\pm}(x,\omega_n) =& \frac{G_{\omega_n}(x,x_2)G_{11}(\omega_n) - G_{\omega_n}(x,x_1)G_{12}(\omega_n)}{G_{11}(\omega_n)G_{22}(\omega_n) - G_{12}(\omega_n)G_{21}(\omega_n)} \\ & \pm \frac{G_{\omega_n}(x,x_1)G_{22}(\omega_n) - G_{\omega_n}(x,x_2)G_{21}(\omega_n)}{G_{11}(\omega_n)G_{22}(\omega_n) - G_{12}(\omega_n)G_{21}(\omega_n)}. \end{aligned} \tag{211}$$

Also constant terms arise

$$S_{\mathrm{U}}^{\mathrm{const}} = \frac{e^2\beta}{2\pi} \sum_n \int\int \mathrm{d}x\, \mathrm{d}x' E(x,\omega_n) E(x',\omega_n) \tilde{M}(x,x',\omega_n) \tag{212}$$

$$\begin{aligned} \tilde{M}(x,x',\omega_n) =& \frac{G_{\omega_n}(x,x_1)G_{22}(\omega_n)G_{\omega_n}(x,x_1)}{G_{11}(\omega_n)G_{22}(\omega_n) - G_{12}(\omega_n)G_{21}(\omega_n)} \\ & + \frac{G_{\omega_n}(x,x_2)G_{11}(\omega_n)G_{\omega_n}(x,x_2)}{G_{11}(\omega_n)G_{22}(\omega_n) - G_{12}(\omega_n)G_{21}(\omega_n)} \\ & - \frac{2G_{\omega_n}(x,x_1)G_{12}(\omega_n)G_{\omega_n}(x',x_2)}{G_{11}(\omega_n)G_{22}(\omega_n) - G_{12}(\omega_n)G_{21}(\omega_n)}. \end{aligned} \tag{213}$$

Eqs. (205) to (213) form the general effective action for a double barrier in a TLL quantum wire. The effects of the interactions in the system are manifest through the Green functions in the kernels. If one makes further assumptions of the microscopic details like the range of the interaction, its strength and/or homogeneity, the Green function can be specified and the effective action may be cast into significantly clearer expressions. Particular cases of the interaction and the electric potential landscape are discussed in the core chapters 5.1-5.4.

D Renormalization group for a single barrier in a TLL

The idea of a renormalization group analysis is that a change in the high-energy cutoff ($\hbar\omega_{\mathrm{c}} \to \hbar\mu$) of a theoretical model should not change the low-energy physics fundamentally but is only accompanied by a modification of the parameters of the theory as to mass, coupling constants etc. Progressively integrating out the high-momentum degrees of freedom one gets an effective action that has same form as the initial one but with renormalized or rescaled parameters of the underlying theory. Repeating this procedure one obtains a scaling flow of the parameters which traces the changing parameters as the cutoff of lowered. The fixed point of a model are the points in parameter space where the parameters remain the same whatever the value of the cutoff is. The parameters fall into three categories: relevant, irrelevant and marginal. Relevant (irrelevant) parameters grow (decrease) under renormalization, and marginal operators undergo logarithmic variations. Hence an irrelevant parameter does not affect the low energy properties of a model.

In our case the parameter space is one-dimensional and has only the impurity strength U_{i} [113, 150]. We start off with the continuous form of the single barrier effective action given in eq. (25) and the corresponding partition function (we choose

$x_\mathrm{i} = 0$, omit the index i at the fields and write the high-energy cutoff ω_c explicitly)

$$S[\theta] = \frac{1}{2}\int\limits_{|\omega|<\omega_\mathrm{c}} \frac{\mathrm{d}\omega}{2\pi}\frac{\theta(\omega)\theta(-\omega)}{G(\omega)} + U_\mathrm{i}\int_0^{\hbar\beta}\mathrm{d}\tau\cos[2\sqrt{\pi}\theta(\tau)] \tag{214}$$

$$Z_0 = \int \mathcal{D}\theta\,\mathrm{e}^{-\int \mathrm{d}\tau\, S[\theta(\tau)]/\hbar}. \tag{215}$$

Here, $G(\omega)$ denotes the one point function $G_\omega(x,x)$. We define "slow" and "fast" modes of the field $\theta(\tau) = \theta_\mathrm{s}(\tau) + \theta_\mathrm{f}(\tau)$ that are separated by μ in ω-space

$$\begin{aligned}\theta(\omega) &\approx \theta_\mathrm{s}(\omega) \quad \text{for} \quad |\omega| \le \mu\\ \theta(\omega) &\approx \theta_\mathrm{f}(\omega) \quad \text{for} \quad \mu < |\omega| \ll \omega_\mathrm{c}.\end{aligned}$$

To eliminate the fast modes we need to define an average $\langle\cdot\rangle_\mathrm{f}$ with respect to the θ_f s. This is done by a smooth function $w(x)$ which goes to unity for $x \gg 1$ and $w(x) \to 0$ for $x \to 0$ in the Fourier transformed Green function,

$$G_\mathrm{f}(\tau) \equiv \langle\theta(\tau)\theta(0)\rangle_\mathrm{f} = \langle\theta_\mathrm{f}(\tau)\theta_\mathrm{f}(0)\rangle = \int\limits_{|\omega|<\omega_\mathrm{c}} \frac{\mathrm{d}\omega}{2\pi} G(\omega)\mathrm{e}^{i\omega\tau}w(\omega/\mu), \tag{216}$$

$$\text{where} \quad w(x) \overset{\text{e.g.}}{=} \frac{x^2}{1+x^2}.$$

To calculate the effective partition function for the slow modes $\tilde{Z} = \int \mathcal{D}\theta_\mathrm{f} Z_0$ we treat the barrier term peturbatively by expanding in powers of $U_\mathrm{i} = U_\mathrm{i}(\omega_\mathrm{c})$ (to first order)

$$Z_0 = \int \mathcal{D}\theta\,\exp\left[-\frac{1}{2}\int\limits_{|\omega|<\omega_\mathrm{c}} \frac{\mathrm{d}\omega}{2\pi}\theta(\omega)G^{-1}(\omega)\theta(-\omega)\right]\times \left(1 - U_\mathrm{i}(\omega_\mathrm{c})\int_0^{\hbar\beta}\mathrm{d}\tau\cos[2\sqrt{\pi}\theta(\tau)]\right) + O[U_\mathrm{i}^2]. \tag{217}$$

The first term is treated by changing the integration limit to $|\omega| < \mu$, but to fast-average out the modes in the cosine we decompose into θ_s and θ_f and separate it into the imaginary and real part. Doing so we get in $\tilde{Z}$ terms

$$\frac{1}{2}\int \mathcal{D}\theta_\mathrm{f}\int_0^{\hbar\beta}\mathrm{d}\tau\,\exp\left[\pm i2\sqrt{\pi}\theta_\mathrm{f}(\tau) - \frac{1}{2}\int\limits_{|\omega|<\omega_\mathrm{c}} \frac{\mathrm{d}\omega}{2\pi}\theta(\omega)G^{-1}(\omega)\theta(-\omega)\right]. \tag{218}$$

We can only integrate over the fast modes by introducing the weight function $w(\omega/\mu)$ in the Fourier transforms

$$\int_0^{\hbar\beta}\mathrm{d}\tau\int\mathcal{D}\theta\,\exp\left\{-\int\limits_{|\omega|<\omega_\mathrm{c}}\frac{\mathrm{d}\omega}{2\pi}\Big[\mp i2\sqrt{\pi}\theta(\omega)w(\omega/\mu)\mathrm{e}^{i\omega\tau} + \frac{1}{2}\theta(\omega)\,w(\omega/\mu)G^{-1}(\omega)\theta(-\omega)\Big]\right\}. \tag{219}$$

The pathintegral is done by diagonalizing the exponent by a change of variables $\theta(\omega) \to \theta^*(\omega) + \Lambda(\omega)$ where $\Lambda = \pm i\sqrt{\pi}\mathrm{e}^{-i\omega\tau}G(\omega)$. This yields for the effective partition sum

$$\tilde{Z} = Z_0^{\mathrm{f}} \int \mathcal{D}\theta_{\mathrm{s}} \, \exp\left[-\frac{1}{2}\int\limits_{|\omega|<\mu} \frac{\mathrm{d}\omega}{2\pi}\theta_{\mathrm{s}}(\omega)G^{-1}(\omega)\theta_{\mathrm{s}}(-\omega)\right] \times$$
$$\left(1 - U_{\mathrm{i}}(\omega_{\mathrm{c}}) \int_0^{\hbar\beta} \mathrm{d}\tau \cos[2\sqrt{\pi}\theta_{\mathrm{s}}(\tau)] \exp\left[-\frac{\pi}{2}\int\limits_{|\omega|<\omega_{\mathrm{c}}} \frac{\mathrm{d}\omega}{2\pi} G(\omega) w(\omega/\mu)\right]\right), \quad (220)$$

where Z_0^{f} is the partition function with respect to the fast modes for the unperturbed action in eq. (214), higher order terms in U_{i} are omitted, and the exponent in the second exponential term is identified with the Green function $G_{\mathrm{f}}(0) = \langle\theta(\tau \to 0)\theta(0)\rangle_{\mathrm{f}}$ as in eq. (216). So the barrier term is renormalized by

$$U_{\mathrm{i}}(\omega_{\mathrm{c}}) \, \mathrm{e}^{-\frac{\pi}{2}G_{\mathrm{f}}(0)} \int_0^{\hbar\beta} \mathrm{d}\tau \cos[2\sqrt{\pi}\theta_{\mathrm{s}}(x)]. \quad (221)$$

Carrying out the integration using $G(\omega) = 2g_0/|\omega|$ we get $G_{\mathrm{f}}(0) = -g_0 \ln(\omega_{\mathrm{c}}/\mu)$. We conclude the renormalization group transformation by rescaling $\tau \to (\omega_{\mathrm{c}}/\mu)\tau$. The effective, renormalized partition function Z_0^{s} for the slow modes then reads

$$Z_0^{\mathrm{s}} = \int \mathcal{D}\theta_s \, \mathrm{e}^{-S^{\mathrm{s}}/\hbar} \quad (222)$$

$$S^{\mathrm{s}}[\theta_{\mathrm{s}}] = \frac{1}{2}\int\limits_{|\omega|<\mu} \frac{\mathrm{d}\omega}{2\pi}\frac{\theta_{\mathrm{s}}(\omega)\theta_{\mathrm{s}}(-\omega)}{G(\omega)} + U_{\mathrm{i}}(\omega_{\mathrm{c}})[\omega_{\mathrm{c}}/\mu]^{1-g_0}\int_0^{\hbar\beta}\mathrm{d}\tau\cos[2\sqrt{\pi}\theta_{\mathrm{s}}(\tau)] \quad (223)$$

By comparing the eqs. (214) with (223) we get the renormalization group equation for the potential $U_{\mathrm{i}}(\mu) = U_{\mathrm{i}}(\omega_{\mathrm{c}})[\omega_{\mathrm{c}}/\mu]^{1-g_0}$. This yields the flow equation with $\mathrm{d}l = \mathrm{d}\mu/\mu$

$$\frac{\mathrm{d}U_{\mathrm{i}}}{\mathrm{d}l} = (1-g_0)U_{\mathrm{i}}(l). \quad (224)$$

E Fourier weights of the dot dissipative kernel $W_\varepsilon(t)$

The Fourier weights for $\exp\{-W_\varepsilon(t)\}$ are calculated as an expansion around the zero temperature expression of $W(t)$ [115, 66],

$$W_\varepsilon(t, T=0) = \frac{1}{g_0}\mathrm{Ln}\left[\frac{1-\mathrm{e}^{-\varepsilon/\omega_{\mathrm{c}}} - i\varepsilon t}{1-\mathrm{e}^{-\varepsilon/\omega_{\mathrm{c}}}}\right]. \quad (225)$$

We plug this into the Fourier transform for the $w_p(\varepsilon)$ and have,

$$\begin{aligned} w_p(\varepsilon) =& \frac{\varepsilon}{2\pi}\int_0^{2\pi/\varepsilon} \mathrm{d}t \frac{\left[1-\mathrm{e}^{-\varepsilon/\omega_c}\right]^{1/g_0}}{\left[1-\mathrm{e}^{-\varepsilon/\omega_c - i\varepsilon t}\right]^{1/g_0}}\, \mathrm{e}^{ip\varepsilon t} \\ =& \left\{ z = \mathrm{e}^{-i\varepsilon t} \right\} \\ =& \frac{-1}{2\pi}\left[1-\mathrm{e}^{-\varepsilon/\omega_c}\right]^{1/g_0} i \int_0^{\mathrm{e}^{-2\pi i}} \frac{\mathrm{d}z}{z^{p+1}\left[1-\mathrm{e}^{-\varepsilon/\omega_c} z\right]^{1/g_0}} \\ =& \left\{ \begin{array}{l} y = \mathrm{e}^{-\varepsilon/\omega_c} \\ 1 \geq g_0 > 0 \end{array} \right\} \\ =& \frac{-1}{2\pi}\left[1-\mathrm{e}^{-\varepsilon/\omega_c}\right]^{1/g_0} i \int_{|z|=1} \frac{y^{1/g_0}\mathrm{d}z}{z^{p+1}(y-z)^{1/g_0}} \end{aligned}$$

The integral is now solved with the residues of $1/z^{p+1}$ since the other singularity is outside the circle $|z| = 1$,

$$\begin{aligned} w_p(\varepsilon) &= \left[1-\mathrm{e}^{-\varepsilon/\omega_c}\right]^{1/g_0} y^{1/g_0}\, \mathrm{Res}\left[\frac{z^{-p-1}}{(y-z)^{1/g_0}}; 0\right] \\ &= \left[1-\mathrm{e}^{-\varepsilon/\omega_c}\right]^{1/g_0} y^{1/g_0}\, \frac{1}{p!}\, \lim_{z\to 0}\frac{\mathrm{d}}{\mathrm{d}z^p}\frac{1}{(y-z)^{1/g_0}} \\ &= \left[1-\mathrm{e}^{-\varepsilon/\omega_c}\right]^{1/g_0} \frac{\Gamma(1/g_0+p)}{p!\Gamma(1/g_0)} \mathrm{e}^{-p\varepsilon/\hbar\omega_c}, \end{aligned}$$

where $p = 0, 1, 2\ldots$ We note that terms other than zeroth order in p are always of higher order than $e^{-\beta\varepsilon}$. Therefore we only keep the term $w_{p=0}(\varepsilon)$ for our analysis of the quantum Coulomb blockade conductance peaks.

F Green function for the box inhomogeneity

The Green function for a piecewise constant interaction strength can be calculated exactly. The wire region is described by the interaction parameter g_1 on the length L while g_0 is attributed to the leads,

$$g(x) = \left\{ \begin{array}{lll} g_0 & \text{for} & |x| > L/2 \\ g_1 & \text{for} & |x| \leq L/2 \end{array} \right. . \tag{226}$$

The differential equation for the Green function is solved separately in the intervals $x < -L/2$, $-L/2 \leq x \leq L/2$ and $x > L/2$ where $g = g_0, g_1$ is constant, and by using that the functions and their derivatives must be continuous at $x = \pm L/2$. The fundamental solutions of the differential equation for the propagator in real time

[eq. (192)] are plain waves,

$$\begin{aligned} x' < x < L/2: \quad & \Phi_+ = \mathrm{e}^{i\omega(x-x')g_1/v_\mathrm{F}} + R_+ \, \mathrm{e}^{-i\omega(x-x')g_1/v_\mathrm{F}} \\ x > L/2: \quad & \Phi_+ = t_+ \, \mathrm{e}^{-i\omega(x)g_0/v_\mathrm{F}} \\ -L/2 < x < x': \quad & \Phi_- = \mathrm{e}^{-i\omega(x-x')g_1/v_\mathrm{F}} + R_- \, \mathrm{e}^{i\omega(x-x')g_1/v_\mathrm{F}} \\ x > L/2: \quad & \Phi_- = t_- \, \mathrm{e}^{i\omega(x)g_0/v_\mathrm{F}} \end{aligned}$$

We can eliminate the $t_\pm$ and $R_\pm$ from the continuity conditions and obtain for the fundamental solutions in the region $|x| \leq L/2$,

$$\begin{aligned} x' < x: \quad & \Phi_+ = \mathrm{e}^{i\omega(x-x')g_1/v_\mathrm{F}} + R_0 \, \mathrm{e}^{-i\omega(x-x')g_1/v_\mathrm{F}} \\ x < x': \quad & \Phi_- = \mathrm{e}^{-i\omega(x-x')g_1/v_\mathrm{F}} + R_0 \, \mathrm{e}^{i\omega(x-x')g_1/v_\mathrm{F}} \end{aligned}$$

where

$$R_0 = \frac{g_0 - g_1}{g_0 + g_1} \, \mathrm{e}^{-\omega_n L/v_\mathrm{F}}$$

The full Green function is then constructed using the Wronski determinant,

$$\begin{aligned} G_{\omega_n}(x,x') &= \frac{\Phi_+(x)\Phi_-(x')}{W[\Phi_+,\Phi_-]} \\ W[\Phi_+(x),\Phi_-(x)] &= \Phi'_+(x)\Phi_-(x) - \Phi'_-(x)\Phi_+(x), \end{aligned}$$

Here, Φ' is the derivative with respect to x. We finally get for the (time ordered) propagator for a TLL with piecewise constant interaction strength,

$$\begin{aligned} G_{\omega_n}(x,x') = \frac{g_1}{2\omega_n} \Big[& \mathrm{e}^{-\omega_n(x-x')g_1/v_\mathrm{F}} + R_0^2 \, \mathrm{e}^{\omega_n(x-x')g_1/v_\mathrm{F}} \\ & + 2R_0 \cosh\left[\omega_n(x+x')g_1/v_\mathrm{F}\right] \Big] \times \left[1 - R_0^2\right]^{-1}. \end{aligned} \tag{227}$$

G Form functions, g-parameter and spectral densities

We list additional form functions $\varphi_i(x)$, their respective interaction parameters and the spectral densities here,

$$\varphi_4(x) = \frac{1}{\sqrt{1 + \frac{x^2}{L^2}}} \qquad \varphi_5(x) = \mathrm{e}^{-2|x|/L}$$

$$\varphi_6(x) = \begin{cases} \frac{1}{2}[1 + \cos(2\pi x/L)] & \text{for} \quad -\frac{L}{2} < x < \frac{L}{2} \\ 0 & \text{else} \end{cases}.$$

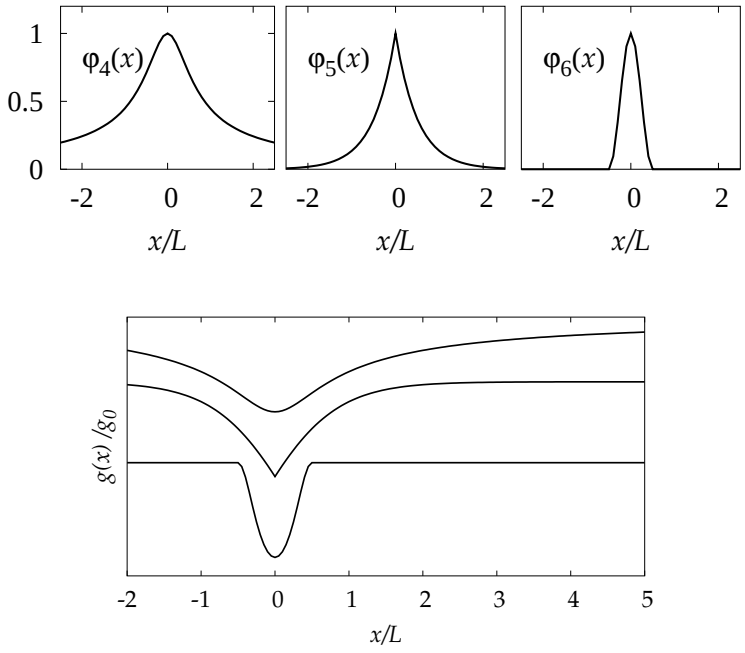

Figure 27: Inhomogeneity potentials $\varphi_i(x)$, $i = 4, 5, 6$ (top) and the respective interaction parameters $g(x)/g_0$ from top to bottom with offset each, (bottom).

The resulting spectral densities are obtained along the eqs. (165,166) and read,

$$J_4^1(\omega) = \frac{\omega}{g_0}\mathrm{Re}\left[1 - \sqrt{\pi}\tilde{V}\frac{\omega}{\omega_*}\Gamma(1/2)\left(\mathbf{H}_0\left[\frac{2\omega}{\omega_*}\right] - \mathbf{N}_0\left[\frac{2\omega}{\omega_*}\right]\right)\Big|_{\omega_n\to -i\omega}\right]^{-1}$$

$$J_5^1(\omega) = \frac{\omega}{g_0}\mathrm{Re}\left[1 - \tilde{V}\frac{\omega_n/\omega_*}{1+(\omega_n/\omega_*)^2}\left(\mathrm{e}^{-\omega_n/\omega_*} + \frac{\omega_n}{\omega_*}\right)\Big|_{\omega_n\to -i\omega}\right]^{-1}$$

$$J_6^1(\omega) = \frac{\omega}{g_0}\mathrm{Re}\left[1 - \frac{\tilde{V}}{2}\left(1 - \mathrm{e}^{-\frac{\omega_n}{\omega_*}} + \frac{(\omega_n/\pi\omega_*)^2}{1+(\omega_n/\pi\omega_*)^2}\left[1 + \mathrm{e}^{-\frac{\omega_n}{\omega_*}}\right]\right)\Big|_{\omega_n\to -i\omega}\right]^{-1}$$

The functions $\mathbf{H}_0$ and $\mathbf{N}_0$ for φ_4 denote the Struve and Neumann functions [134]. The actual shapes are plotted in fig. 28.

H Propagator for small distances

For the kernel in the double barrier effective action we need the one and two point function. The latter only for small distances with respect to the extension L of the potential because we assume that the inhomogeneity changes on a scale much larger than the distance between the two impurities (the length of the quantum dot a). Hence we expand the two point function for the kernel $K(\omega_n)$. The eventually

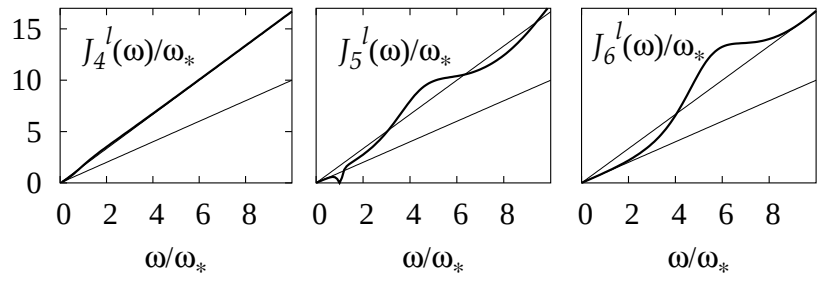

Figure 28: $J_i^1(\omega)$, $i = 4, 5, 6$.

obtained result holds in first order in the inhomogeneity V_1 and first order in a/L. We start from the general form of the Green function (156) from chapter 5.3 and rearrange the terms to obtain ($x_\mathrm{d} = 0$, here),

$$G_{\omega_n}\left(-\frac{a}{2};\frac{a}{2}\right) = \mathrm{e}^{\eta_\mathrm{b} a} G_{\omega_n}(0,0) + \Lambda \tag{228}$$

$$\Lambda = -\frac{g_0}{2\omega_n}\mathrm{e}^{-\eta_\mathrm{b} a} ca \int_0^\infty \mathrm{d}y\, \varphi'(y)\mathrm{e}^{-2\eta y}, \tag{229}$$

where $\eta_\mathrm{d} = g(x_\mathrm{b})\omega/2\pi v_\mathrm{F}$. The kernel $K_\pm(\omega_n)$ then reads

$$K_\pm^{-1} = G_{\omega_n}(0,0)\left[1 \pm \mathrm{e}^{-\eta_\mathrm{d} a}\right] \pm \Lambda. \tag{230}$$

Let us further examine the different energy regimes. The energy scale is divided by (i) the crossover energy $\hbar\omega_* = \hbar v_\mathrm{F}/g_0 L$ and (ii) the level spacing $\varepsilon = \hbar\pi v_\mathrm{F}/ag(x_\mathrm{d})^2$. It is to be noted that the level spacing ε is always larger than the crossover energy. For $\eta_d a \gg 1$ the second term becomes negligible and (228)–(230) yield the usual Ohmic ($\propto \omega/g(x_\mathrm{d})$) and discrete parts ($\propto \sum \delta(\hbar\omega - n\varepsilon)$) of the spectral density. However, in the regime $\eta_\mathrm{d} a \ll 1$ one has to treat the contributions $(\eta_\mathrm{d} a)^n$ with care to recover charging energy and the correct scaling of $J(\omega)$. $\eta_\mathrm{d} a$ must be kept up to second order in the expressions for $K_-(\omega)$ while K_+ and J_+ respectively immediately yield

$$J_+(\omega \ll \omega_*) = \frac{1}{2}\mathrm{Im}\frac{1}{G_{i\omega}(0,0)}. \tag{231}$$

Collecting terms up to $(\eta_\mathrm{d} a)^2$ we get

$$K_-^{-1}(\omega_n) \approx G_{\omega_n}(0,0)\left[\eta_\mathrm{d} a - \frac{1}{2}(\eta_\mathrm{d} a)^2\right] + \eta_\mathrm{d} a(1-\eta_\mathrm{d} a)\mathcal{L} \tag{232}$$

$$\mathcal{L} = \frac{g_0}{2\omega_n}\left[-\frac{c}{\eta}\varphi(0) + 2c\int_0^\infty \mathrm{d}y\, \varphi(y)\mathrm{e}^{-2\eta y}\right] \tag{233}$$

Noting that $G_{\omega_n}(0,0) + 2\mathcal{L} = g(x_\mathrm{d})/g_0$ we have

$$K_-(\omega_n) = \left[\frac{g(x_\mathrm{d})^2 a}{2v_\mathrm{F}}\left(1 - \frac{1}{2}(\eta_\mathrm{d} a)\frac{2\omega_n}{g(x_\mathrm{d})}\left[G_{\omega_n}(0,0) + 2\mathcal{L}\right]\right)\right]^{-1} \tag{234}$$

$$\approx \frac{2v_\mathrm{F}}{g(x_\mathrm{d})^2 a}\left[1 + \frac{1}{2}\eta_\mathrm{d} a \frac{g_0}{g(x_\mathrm{d})}\left\{\frac{2\omega_n}{g_0}\left[G_{\omega_n}(0,0) + 2\mathcal{L}\right]\right\}\right], \tag{235}$$

and

$$J_-(\omega) \approx \frac{1}{2}\mathrm{Im}\left.\frac{2\omega_n}{g_0\left[1 - 2c\int_0^\infty \mathrm{d}y\, \varphi(y)\mathrm{e}^{-2\eta y}\right]}\right|_{\omega_n \to i\omega} \tag{236}$$

$$= \frac{1}{2}\mathrm{Im}\frac{1}{G_{i\omega}(0,0)}. \tag{237}$$

Altogether, the spectral density for the two impurity system is written as

$$J(\omega) = \frac{1}{2}\left[\mathrm{Im}\frac{1}{G_{i\omega}(x_\mathrm{d}, x_\mathrm{d})}\right]\left[1 + \varepsilon\sum_n \delta(\hbar\omega - n\varepsilon)\right]. \tag{238}$$

I Phenomenological $J_\mathrm{b}(\omega)$ with crossover

In the homogeneous case $g(x) = g_0$ where the interaction does not change along the wire the Green function has a simple form which allows to evaluate the dissipative kernel analytically. $\beta = 1/k_\mathrm{B}T$ being the inverse temperature we get

$$W_0(t) = \frac{2}{g_0}\ln\left[\frac{\sqrt{1+\omega_\mathrm{c}^2 t^2}\,\Gamma^2(1 + \frac{1}{\omega_\mathrm{c}\hbar\beta})}{\left|\Gamma(1 + \frac{1}{\omega_\mathrm{c}\beta\hbar}(1 + i\omega_\mathrm{c}t))\right|^2}\right] + i\frac{2}{g_0}\arctan\omega_\mathrm{c}t, \tag{239}$$

and

$$W_0(T \to 0, t) = \frac{2}{g_0}\mathrm{Ln}\left[1 + i\omega_\mathrm{c}t\right]. \tag{240}$$

Also the tunneling rates can be calculated exactly in this case [116, 151],

$$\Gamma_0(E,\beta) = \frac{\Delta^2}{4}\frac{1}{\omega_\mathrm{c}}\left(\frac{\hbar\beta\omega_\mathrm{c}}{2\pi}\right)^{1-\frac{2}{g}}\frac{\left|\Gamma(\frac{1}{g_0} + i\frac{\beta E}{2\pi})\right|^2}{\Gamma(2/g_0)}\mathrm{e}^{\frac{\beta E}{2} - \frac{|E|}{\omega_\mathrm{c}}} \tag{241}$$

$$\xrightarrow{T\to 0} \frac{\Delta^2}{4}\frac{2\pi}{\omega_\mathrm{c}\Gamma(2/g_0)}\left(\frac{E}{\hbar\omega_\mathrm{c}}\right)^{\frac{2}{g_0}-1}\mathrm{e}^{-\frac{E}{\hbar\omega_\mathrm{c}}}. \tag{242}$$

The $\Gamma(x)$ on the right hands side denotes the gamma function. In the zero temperature limit the typical Luttinger liquid power law behavior in E is visible. Using the detailed balance relation for the rate $\Gamma(-E) = \exp(-\beta E)\Gamma(E)$ one can pass to the non-linear conductance and gets

$$\mathcal{G}_0(U, T = 0) = \frac{1}{R_T}\frac{1}{\Gamma(2/g_0)}\left(\frac{eU}{\hbar\omega_\mathrm{c}}\right)^{2/g_0 - 2}. \tag{243}$$

Here, $R_T = 2\hbar\omega_c^2/\pi e^2\Delta^2$. The conductance scales to zero in U in a power law fashion. When we examine the linear conductance at finite temperature a similar power law occurs in T

$$\mathcal{G}_0(U=0,T) = \frac{1}{R_T}\frac{\Gamma^2(1/g_0)}{\Gamma(2/g_0)}\left(\frac{2\pi k_B T}{\hbar\omega_c}\right)^{2/g_0-2}. \tag{244}$$

For our nonhomogeneous interaction we do not expect such a simple power law exponent but, depending on the energy (either thermal or voltage), driven by ω_* a crossover from $g_0 \to g(x_b)$.

Since we know that the spectral density has the above mentioned structure we can try a phenomenological approach in order to examine the crossover from energy regimes governed by g_0 and g_b respectively. We assume the following model spectral density

$$J_{ph}(\omega) = \frac{2\omega}{g_0}e^{-\omega/\omega_*} + \frac{2\omega}{g(x_b)}(1-e^{-\omega/\omega_*}). \tag{245}$$

Doing so we can calculate the rate at zero temperature exactly. Plugging (245) into (63) we get

$$W_{ph}(t) = \int_0^\infty \frac{d\omega}{\omega}\left[\frac{1-\cos\omega t}{\tanh\hbar\omega\beta/2} + i\sin\omega t\right]\left(\frac{2}{g_{eff}}e^{-\omega/\omega_{eff}} + \frac{2}{g(x_b)}e^{-\omega/\omega_c}\right). \tag{246}$$

The two summands have the same form as two homogeneous spectral densities but effective g-parameters and cutoff frequencies

$$\omega_{eff} = \frac{\omega_c\omega_*}{\omega_c+\omega_*} \text{ and: } g_{eff} = \frac{g(x_b)g_0}{g(x_b)-g_0} < 0.$$

Hence we can use the equation (240) and write the forward rate as

$$\Gamma_{ph}(E) = \left(\frac{\Delta}{2}\right)^2 \int_{-\infty}^{\infty} \frac{e^{iEt/\hbar}dt}{[1+i\omega_{eff}t]^{\frac{2}{g_{eff}}}[1+i\omega_c t]^{\frac{2}{g(x_b)}}}. \tag{247}$$

Eq. (247) is analytically feasible and yields

$$\Gamma_{ph}(E) = \left(\frac{\Delta}{2\omega_c}\right)^2 \frac{2\pi\omega_c}{\Gamma(2/g_0)}\left(\frac{E}{\hbar\omega_c}\right)^{2/g_0-1}\left(\frac{\omega_c}{\omega_{eff}}\right)^{2/g_{eff}} M\left[\frac{2}{g_{eff}},\frac{2}{g_0},-\frac{E}{\hbar\omega_*}\right]e^{-E/\hbar\omega_c} \tag{248}$$

The function $M(a,b,z)$ is the confluent hyper geometric function (see below). For high and low energies E we obtain the following asymptotic rates

$$\Gamma_{ph}(E) \xrightarrow{E/\hbar\omega_* \gg 1} \left(\frac{\Delta}{2}\right)^2 \frac{2\pi}{\Gamma(2/g(x_b))}\left(\frac{E}{\hbar\omega_c}\right)^{2/g(x_b)-1}\frac{1}{\omega_c}, \tag{249}$$

which resembles the rate for a homogeneous interaction strength characterized by $g(x_b)$. Instead for low energies a power law corresponding to g_0 is obtained.

$$\Gamma(E) \xrightarrow{E/\hbar\omega_* \ll 1} \left(\frac{\Delta}{2}\right)^2 \frac{2\pi}{\Gamma(2/g_0)} \left(\frac{E}{\hbar\omega_c}\right)^{2/g_0-1} \frac{1}{\omega_c} \left(\frac{\omega_c}{\omega_*}\right)^{2/g_{\rm eff}}. \tag{250}$$

The actual rate has an offset with respect to a rate for homogeneous interaction which is given by the term $(\omega_c/\omega_{\rm eff})^{2/g_{\rm eff}} \ll 1$. Let us examine the rate at zero temperature (Fig. 29). Now we observe the new feature due to the inhomogeneity in $g(x)$; viz. a crossover from a g_0–driven power-law at lower energies E/ω_* to a power law exponent $g(x_b)$ at high E. This means that depending on the A refined

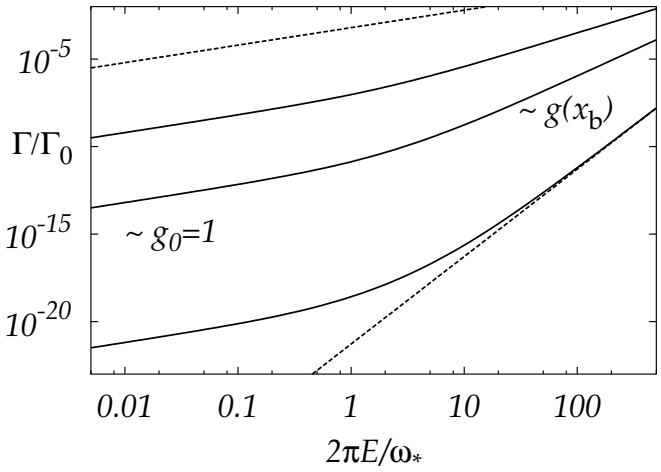

Figure 29: Double logarithmic plot of the rate Γ in units $\Gamma_0 = \Delta^2\omega_c/4$ versus $E/\hbar\omega_*$ at $T = 0$. $g_0 = 1$ and $g(x_b) = 2/3$, 0.5 and $1/3$. The dashed lines are the rates for homogeneous interaction with g_0=1 (top curve) and $g_0 = 1/3$ (bottom curve).

treatment for the rates includes a fit of spectral density in terms of exponential functions. This allows us to calculate the dissipative kernels analytically an reduced the numerical effort to the computation of the tunneling rate, which itself is a slowly converging, massively oscillating integral. Doing so we reduce the computational workload and time considerably.

Integral

We find in [135]

$$\begin{aligned}\int_{-\infty}^{\infty} {\rm d}x\,(\beta+ix)^{-\mu}\,(\gamma+ix)^{-\nu}\,{\rm e}^{-ipx} &= 0 \text{ if } p>0\\ &= \frac{2\pi {\rm e}^{\gamma p}(-p)^{\mu+\nu-1}}{\Gamma(\mu+\nu)}\,{}_1F_1(\mu;\nu;(\beta-\gamma)p) \text{ if } p<0\\ &\qquad \text{where } {\rm Re}\beta>0,\ {\rm Re}\gamma>0,\ \text{and } {\rm Re}(\mu+\nu)>1\end{aligned} \tag{251}$$

${}_1F_1(a,b,z)$ is the confluent hypergeometric function, also known as the *Kummer function* $M(a,b,z)$ [134]. It has the following properties

$$M(a,b,z) = 1 + \frac{a}{b}z + \frac{(a)_2 x^2}{(b)_2 2!} + \cdots + \frac{(a)_n x^n}{(b)_n n!} \ldots$$
$$(a)_0 = 1,\ (a)_n = a(a+1)(a+2)\ldots(a+n-1)$$
$$M(a,b,z) = \frac{\Gamma(b)}{\Gamma(b-a)}(-z)^{-a}\left[1 + \mathrm{O}(|z|^{-1})\right],$$

which we used to obtain eqs. (249) and (250).

References

[1] R. Feynman, Engineering & Science **23**, 22 (1960).

[2] G. Binnig and H. Rohrer, Scientific American **253**, 40 (1985).

[3] G. Binnig, C. Quate, and C. Gerber, Phys. Rev. Lett. **56**, 930 (1986).

[4] J. Bardeen and W. Brattain, Phys. Rep. **74**, 230 (1948).

[5] *UltraSPARC III Cu Processor - Technical Information*, Sun microsystems.

[6] G. Moore, Electronics **38**, 114 (1965).

[7] Y. Imry, *Introduction to mesoscopic physics* (Oxford University Press, Oxford, 1997).

[8] S. Washburn, in *"Mesoscopic phenomena in solids"*, edited by B. Altshuler (Elsevier Science Publishers, New York, 1991).

[9] N. Byers and C. Yang, Phys. Rev. Lett. **7**, 46 (1961).

[10] M. Büttiker, Y. Imry, and R. Landauer, Phys. Rev. A **96**, 365 (1983).

[11] L. Levy, G. Dolan, J. Dunsmuir, and H. Bouchiat, Phys. Rev. Lett. **64**, 2074 (1990).

[12] K. von Klitzing, G. Dorda, and M. Pepper, Phys. Rev. Lett. **45**, 494 (1980).

[13] D. Wharam *et al.*, J. Phys. C **21**, L209 (1988).

[14] B. van Wees *et al.*, Phys. Rev. Lett. **60**, 848 (1988).

[15] J. Voit, Rep. Prog. Phys **57**, 977 (1994), cond-mat/9510014 (update).

[16] C. Kane and M. P. Fisher, Phys. Rev. Lett. **68**, 1220 (1992).

[17] D. Maslov, Phys. Rev. B **52**, R14368 (1995).

[18] V. Ponomarenko, Phys. Rev. B **52**, R8666 (1995).

[19] I. Safi and H. Schulz, Phys. Rev. B **52**, R17040 (1995).

[20] Y. Oreg and A. M. Finkelstein, Phys. Rev. B **54**, R14265 (1996).

[21] A. Kawabata, J. Phys. Soc. Jap. **65**, 30 (1996).

[22] A. Furusaki and N. Nagosa, Phys. Rev. B **47**, 4631 (1993).

[23] S. M. Sze, *Semiconductor devices*, 2nd ed. (Wiley & Sons, New York, 1985).

[24] J. Weiner *et al.*, Phys. Rev. Lett. **63**, 1641 (1989).

[25] K. Ismail, S. Washburn, and K. Lee, Appl. Phys. Lett. **59**, 1998 (1991).

[26] A. Goñi *et al.*, Phys. Rev. Lett. **67**, 3298 (1991).

[27] A. Schmeller *et al.*, Phys. Rev. B **49**, 14778 (1994).

[28] C. Schüller *et al.*, Phys. Rev. B **54**, R17304 (1996).

[29] M. Sassetti and B. Kramer, Phys. Rev. Lett. **80**, 1485 (1998).

[30] S. Tarucha, T. Honda, and T. Saku, Solid State Comm. **94**, 413 (1995).

[31] B. Kane *et al.*, Appl. Phys. Lett. **72**, 306 (1998).

[32] K. Thomas *et al.*, Phys. Rev. Lett. **77**, 135 (1996).

[33] C. Liang *et al.*, Phys. Rev. B **61**, 9952 (2000).

[34] D. Kaufman *et al.*, Phys. Rev. B **59**, R10433 (1999).

[35] B. Dwir *et al.*, Physica B **259-261**, 1025 (1999).

[36] L. N. Pfeiffer *et al.*, J. Crystal Growth **849**, 127 (1993).

[37] A. Yacoby *et al.*, Phys. Rev. Lett. **77**, 4612 (1996).

[38] A. Yacoby *et al.*, Solid State Comm. **101**, 77 (1997).

[39] M. Rother *et al.*, Physica E **6**, 551 (2000).

[40] D. Maslov and M. Stone, Phys. Rev. B **52**, R5539 (1995).

[41] R. de Picciotto *et al.*, Phys. Rev. Lett. **85**, 1730 (2000).

[42] R. de Picciotto, H. L. Stormer, K. W. Baldwin, and K. W. West, Nature **411**, 51 (2001).

[43] O. M. Auslaender *et al.*, Science **295**, 825 (2002).

[44] R. Saito, G. Dresselhaus, and M. Dresselhaus, *Physical Properties of Carbon Nanotubes* (Imperial College Press, London, 1998).

[45] in *Proceeedings of the School and Workshop on Nanotubes & Nanostructures 2000*, Vol. 74 of *Atti di Conferenze – Conference Proceedings*, Società di Fisica, edited by S. Bellucci (Compositori, Bologna, Italy, YEAR).

[46] C. Kane and E. Mele, Phys. Rev. Lett. **78**, 5986 (1997).

[47] P. Wallace, Phys. Rep. **71**, 622 (1947).

[48] R. Saito, M. Fujita, G. Dresselhaus, and M. Dresselhaus, Appl. Phys. Lett. **60**, 2204 (1992).

[49] M. Ouyang, J.-L. Huang, and C. Lieber, Phys. Rev. Lett. **88**, 66804 (2002).

[50] A. Thess *et al.*, Science **273**, 483 (1996).

[51] T. W. Ebbesen *et al.*, Chem. Phys. Lett. **209**, 83 (1993).

[52] J. Wildröer *et al.*, Nature **391**, 59 (1998).

[53] T. W. Odom, J.-L. Huang, P. Kim, and C. M. Lieber, Nature **391**, 62 (1998).

[54] J. Nygård *et al.*, Appl. Phys. A **69**, 297 (1999).

[55] W. Liang *et al.*, Nature **411**, 665 (2001).

[56] M. Bockrath *et al.*, Nature **387**, 598 (1999).

[57] *Single charge tunneling*, Vol. B294 of *NATO ASI Series*, edited by H. Grabert and M. Devoret (Plenum Press, New York, 1992).

[58] M. Bockrath *et al.*, Science **275**, 1922 (1997).

[59] S. J. Tans *et al.*, Nature **386**, 474 (1997).

[60] M. Buitelaar, A. Bachthold, T. Nussbaumer, and C. Schönenberger, Phys. Rev. Lett. **88**, 156801 (1998).

[61] D. Bozovic *et al.*, Appl. Phys. Lett. **78**, 3696 (2001).

[62] H. Postma, M. de Jonge, Z. Yao, and C. Dekker, Phys. Rev. B **62**, R10653 (2000).

[63] A. Kumar, S. E. Laux, and F. Stern, Phys. Rev. B **42**, 5166 (1990).

[64] L. P. Kouwenhoven *et al.*, in *Mesoscopic Electron Transport*, edited by L. Sohn, L. Kouwenhoven, and G. Schön (Kluwer, Dordrecht, 1997), Chap. Electron Transport in Quantum Dots.

[65] G. Ingold and Y. Nazarov, in *Single charge tunneling*, Vol. B294 of *NATO ASI series*, edited by H. Grabert and M. Devoret (Plenum Press, New York, 1992).

[66] A. Braggio, M. Grifoni, M. Sassetti, and F. Napoli, Europhys. Lett. **50**, 236 (2000).

[67] I. Kulik and R. Shekhter, Zh. Eksp. Teor. Fiz. **68**, 623 (1975).

[68] D. Averin and K. Likharev, Journal of Low Temperature Physics **62**, 345 (1986).

[69] C. Bennakker, Phys. Rev. B **44**, 1646 (1991).

[70] H. Schöller and G. Schön, Phys. Rev. B **50**, 18436 (1994).

[71] D. Goldhaber-Gordon *et al.*, Nature **391**, 156 (1998).

[72] S. M. Cronenwett, T. H. Osterkamp, and L. P. Kouwenhoven, Science **281**, 540 (1998).

[73] L. Kouwenhoven and L. Glazman, Physics World **14**, 33 (2001).

[74] O. Auslaender *et al.*, Phys. Rev. Lett. **84**, 1764 (2000).

[75] M. Bockrath *et al.*, Nature **291**, 283 (2001).

[76] H. Postma *et al.*, Science **293**, 76 (2001).

[77] M. Thorwart *et al.*, Phys. Rev. Lett. **111**, 111 (2002).

[78] M. Thorwart and M. Grifoni, Chem. Phys. **281**, 477 (2002).

[79] Y. Nazarov and L. Glazman, cond-mat/0209090 (unpublished).

[80] S. Tomonaga, Prog. Theor. Phys. **5**, 544 (1950).

[81] J. Luttinger, J. Math. Phys. **4**, 1154 (1963).

[82] M. Sassetti, in *Quantum Transport in Semiconductor Submicron Structures*, Vol. 326 of *E*, NATO ASI Series, edited by B. Kramer (Kluwer Academic Publisher, Dordrecht, 1996), pp. 95 – 131.

[83] H. Schulz, *Les Houche Ecole d'Ete de Physique Theorique* (Elsevier Science Publishers B.V., Amsterdam, 1995), Vol. LXI, p. pp 533, cond-mat/9503150.

[84] M. Stone, in *Bosonization*, edited by M. Stone (World Scientific, Singapore, 1994).

[85] J. von Delft and H. Schoeller, Ann. Phys. **4**, 225 (1998).

[86] K. Schönhammer, cond-mat/9710330 (unpublished).

[87] P. Nozieres, *Theory of Interacting Fermi Systems* (W.A. Benjamin, New York, Amsterdam, 1964).

[88] H.J. Schulz and G. Cuniberti and P. Pieri, in *Field Theories for Low Dimensional Condensed Matter Systems*, *Springer Lecture Notes in Physics*, edited by G. Morandi and A. Tagliacozzo and P. Sodano (Springer, Heidelberg, 2000).

[89] J. M. Luttinger, Phys. Rev. **119**, 1153 (1960).

[90] F. Haldane, J. Phys. C **14**, 2585 (1981).

[91] D. C. Mattis and E. H. Lieb, J. Math. Phys. **4**, 304 (1965).

[92] R. Heidenreich, R. Seiler, and D. Uhlenbrock, J. Stat. Phys. **22**, 27 (1980).

[93] P. Kopietz, *Bosonization of interacting fermions in arbitrary dimensions*, *Lecture notes in physics* (Springer–Verlag, Berlin, Heidelberg, 1997).

[94] A. E. Mattson, S. Eggert, and H. Johannesson, Phys. Rev. B **56**, 15615 (1997).

[95] S. Eggert, A. E. Mattssson, and J. Kinaret, Phys. Rev. B **56**, R15537 (1997).

[96] K. Schönhammer *et al.*, Phys. Rev. B **61**, 4393 (2000).

[97] M. Fabrizio and A. Gogolin, Phys. Rev. B **51**, 17827 (1995).

[98] S. Shankar, Rev. Mod. Phys. **66**, 129 (1994).

[99] I. Affleck, in *Fields, Strings and Critical Phenomena*, edited by E. Brèzin and J. Zinn-Justin (Elsevier, Amsterdam, 1989), p. 564.

[100] R. Kubo, M. Toda, and N. Hashimitsume, *Statistical Physics II*, Vol. 31 of *Springer Series in Solid-State Sciences* (Springer-Verlag, Berlin, 1985).

[101] G. Mahan, *Many-Particle Physics*, 2nd ed. (Plenum Press, New York, 1990).

[102] G. Cuniberti, M. Sassetti, and B. Kramer, Physica B **227**, 256 (1996).

[103] G. Cuniberti, M. Sassetti, and B. Kramer, Phys. Rev. B **57**, 1515 (1998).

[104] I. Safi, Phys. Rev. B **55**, R7331 (1997).

[105] S. Lal, S. Rao, and D. Sen, Phys. Rev. Lett. **87**, 26801 (2001).

[106] R. Landauer, Phil. Mag. **21**, 863 (1970).

[107] R. Landauer, Z. Phys. **68**, 217 (1987).

[108] M. Büttiker, Phys. Rev. Lett. **57**, 1761 (1986).

[109] C. Kane and M. P. Fisher, Phys. Rev. B **46**, 15233 (1992).

[110] T. Giamarchi and H. Schulz, Phys. Rev. B **37**, 325 (1988).

[111] I. Safi and H. Schulz, Phys. Rev. B **59**, 3040 (1999).

[112] L. Glazman, I. Ruzin, and B. Shklovskii, Phys. Rev. B **45**, 8454 (1992).

[113] M. Fisher and W. Zwerger, Phys. Rev. B **32**, 6190 (1985).

[114] U. Weiss, M. Sassetti, T. Negele, and M. Wollensak, Z. Phys. B **84**, 471 (1991).

[115] U. Weiss, *Quantum Dissipative Systems (2nd edition)*, Vol. 10 of *Series in Modern Condensed Matter Physics* (World Scientific Publishing, Singapore, 1999).

[116] R. Egger, C. Mak, and U. Weiss, J. Chem. Phys. **100**, 2651 (1994).

[117] M. Sassetti and U. Weiss, Europhys. Lett. **27**, 311 (1994).

[118] A. Caldeira and A. Leggett, Ann. Phys. **149**, 374 (1983).

[119] P. Fendley, A. Ludwig, and H. Saleur, Phys. Rev. B **52**, 8934 (1995).

[120] M. Sassetti, G. Cuniberti, and B. Kramer, Solid State Comm. **101**, 915 (1997).

[121] A. Furusaki and N. Nagaosa, Phys. Rev. B **54**, R5239 (1996).

[122] A. Fechner, M. Sassetti, and B. Kramer, Europhys. Lett. **45**, 693 (1999).

[123] R. Feynman and F. Vernon, Ann. Phys. **24**, 118 (1963).

[124] M. Sassetti, F. Napoli, and U. Weiss, Phys. Rev. B **52**, 11213 (1995).

[125] A. Furusaki and N. Nagosa, Phys. Rev. B **47**, 3827 (1993).

[126] A. Furusaki, Phys. Rev. B **57**, 7141 (1998).

[127] Y. Yang and T. Lin, Phys. Rev. B **64**, 233314 (2001).

[128] A. Braggio, M. Sassetti, and B. Kramer, Phys. Rev. Lett. **87**, 146802 (2001).

[129] T. Kleimann, G. Cuniberti, M. Sassetti, and B. Kramer, in *Proceedings of the School and Workshop on Nanotubes & Nanostructures 2000*, edited by S. Bellucci (Compositori, Bologna, 2001), Vol. 74, pp. 257–263.

[130] G. Cuniberti, Ph.D. thesis, Università degli Studi di Genova, 1998.

[131] T. Kleimann, Master's thesis, Universität Hamburg, 1999.

[132] M. Sassetti and B. Kramer, Eur. Phys. J. B **4**, 357 (1998).

[133] H. Schulz, Phys. Rev. Lett. **71**, 1864 (1993).

[134] M. Abramowitz and I. A. Stegun, *Handbook of Mathematical Functions* (Dover Publications, Inc., New York, 1965).

[135] I. Gradshteyn and I. Ryzhik, *Table of Integrals, Series, and Products*, fourth ed. (Academic Press Inc., New York and London, 1965).

[136] A. Prudnikov, Y. A. Brychkov, and O. Marichev, *Integrals and Series* (Gordon and Breach Science Publishers, New York, 1986).

[137] M. Sassetti and B. Kramer, Phys. Rev. B **54**, R5203 (1996).

[138] C. Kane and M. P. Fisher, Phys. Rev. B **46**, 7268 (1992).

[139] E. Lieb and D. Mattis, Phys. Rev. **125**, 164 (1962).

[140] D. Weinmann, W. Häusler, and B. Kramer, Phys. Rev. Lett. **74**, 984 (1995).

[141] R. Egger and A. Gogolin, Eur. Phys. J. B **3**, 281 (1998).

[142] H. Yoshioka and A. Odintsov, Phys. Rev. Lett. **82**, 374 (1999).

[143] R. Egger and A. Gogolin, Phys. Rev. Lett. **79**, 5082 (1997).

[144] C. Kane, L. Balents, and M. Fisher, Phys. Rev. Lett. **79**, 5086 (1997).

[145] E. Taft and H. Philipp, Phys. Rev. B **138**, A 197 (1965).

[146] K. Matveev and L. Glazman, Phys. Rev. Lett. **70**, 990 (1993).

[147] T. Kleimann, M. Sassetti, B. Kramer, and A. Yacoby, Phys. Rev. B **62**, 8144 (2000).

[148] L. Schulman, *Techniques and Applications of Path Integration* (Wiley, New York, 1981).

[149] J. Zinn-Justin, *Quantum field theory and critical phenomena* (Oxford University Press, New York, 1989).

[150] T. Ohta and D. Jasnow, Phys. Rev. B **20**, 139 (1979).

[151] M. P. A. Fisher and A. T. Dorsey, Phys. Rev. Lett. **54**, 1609 (1985).

Acknowledgements

I would like to thank all the persons who supported me during the years of my PhD studies, and made the stay in Genoa pleasant – scientifically as well as socially.